APPU Aircraft Empennage Design

Multidisciplinary Design Optimization of a Cruciform or T-tail Empennage

Master Thesis Aerospace Engineering

Jan Heiremans

Delft University of Technology

TU Delft

APPU Aircraft Empennage Design

Multidisciplinary Design Optimization of a Cruciform or T-tail Empennage

by

Jan Heiremans

in partial fulfillment of the requirements for the degree of

Master of Science
in Aerospace Engineering

at the Delft University of Technology,
to be defended publicly on Monday June 30, 2025 at 1:00 PM.

Supervisor:	Dr.-Ing. A. Heidebrecht	
Thesis committee:	Dr. ir. R. Vos,	TU Delft
	Dr.-Ing. A. Heidebrecht,	TU Delft
	Dr. M. D. Pavel,	TU Delft

An electronic version of this thesis is available at `http://repository.tudelft.nl/`.

TU Delft Delft University of Technology

Preface

This thesis is the culmination of my academic journey in the field of aerospace engineering. It marks the conclusion of several years of study, during which I encountered both progress and setbacks. Despite the challenges along the way, this period has been deeply formative and rewarding. As I now prepare to take the next step, I look forward to applying the knowledge and skills I have gained to address complex and meaningful problems.

I am particularly grateful to Alexander Heidebrecht for his invaluable guidance, insightful feedback, and consistent support throughout this process. I would like to show my appreciation to ParaPy and FlightStream for providing the software licenses that made this work possible. I am especially thankful to Colin Heimans of ParaPy for his active support and technical guidance, which greatly facilitated the integration of FlightStream with ParaPy.

Special thanks to my parents for their support throughout this project and, by extension, throughout my entire studies. They provided me with opportunities that I will forever be grateful for. I would like to thank my girlfriend, friends, and family for offering the much needed moments of relaxation and encouragement that helped me maintain my motivation throughout this journey.

Jan Heiremans
Denderleeuw, June 2025

Abstract

The APPU project aims to lower the threshold of installing hydrogen-driven and boundary-layer-ingesting propulsion systems in the short term. This is done by replacing the Auxiliary Power Unit with an Auxiliary Power & Propulsion Unit (APPU). To study these concepts, the Airbus A321neo is taken as a reference baseline. The implementation of the APPU system on the A321neo aircraft necessitates a redesign of the existing empennage. The research objective of this thesis project is to investigate how an optimal empennage design for an aircraft equipped with an APPU system differs from an optimal empennage design for an aircraft without such a system. Multidisciplinary design optimization is used to minimize fuel weight for different aircraft configurations by optimizing the empennage geometry. Four different disciplines are identified. A weight discipline estimates the empennage weight based on the empirical Raymer equations. Two separate aerodynamic disciplines are implemented with different fidelity levels. The low-fidelity version is based on AVL's vortex lattice method, expanded with a constant friction coefficient drag model to account for viscous effects. The high-fidelity version is based on FlightStream's panel method. FlightStream proved to be infeasible for use in this study due to long run times and limited mesh robustness. Therefore, only the low-fidelity version is used to generate the final results. The static stability and control of the aircraft are ensured through a set of constraints that require specific stability and control derivatives to remain within defined limits. These derivatives are provided by the stability and control discipline that is based on AVL as well. The performance discipline applies the Breguet equation to convert the aircraft weight and aerodynamic performance into an estimate of the fuel load required to complete the design range. ParaPy is used as a multi-model-generator to provide the required input geometries for the disciplines. The study reveals that optimal empennage designs for aircraft equipped with an APPU system differ notably from optimal empennage designs for conventional aircraft. Both configurations benefit from high aspect ratios and reduced tailplane areas. However, APPU-equipped aircraft require a low cruciform tail to accommodate the hydrogen tank and reduced sweep angles to position the aerodynamic center aft without intersecting the propulsor plane. The low-fidelity aerodynamics discipline is unable to optimize the airfoils. AVL's modeling of only the camber line makes it unsuitable for optimizing symmetric profiles, such as those on vertical tailplanes. Furthermore, the horizontal tailplane airfoils showed limited variation from the initial design. This is likely due to the dual-parameter definition of the camber line, as the class-shape transformation parameterization method is applied independently to both the upper and lower surfaces of the airfoils.

Contents

Nomenclature

Abbreviations

Abbreviation	Definition
APPU	Auxiliary Power & Propulsion Unit
APU	Auxiliary Power Unit
AR	Aspect Ratio
AVL	Athena Vortex Lattice
BL	Boundary Layer
BLI	Boundary Layer Ingestion
CAD	Computer-Aided Design
CFD	Computational Fluid Dynamics
CST	Class-Shape Transformation
DLM	Doublet Lattice Method
DSM	Design Structure Matrix
EASA	European Union Aviation Safety Agency
HTP	Horizontal TailPlane
IDF	Individual Discipline Feasible
LE	Leading Edge
MAC	Mean Aerodynamic Chord
MDA	MultiDisciplinary Analysis
MDF	MultiDisciplinary Feasible
MDO	Multidisciplinary Design Optimization
MMG	Multi-Model Generator
OEW	Operating Empty Weight
QP	Quadratic Programming
SFC	Specific Fuel Consumption
SLSQP	Sequential Least Squares Quadratic Programming
STEP	STandard for the Exchange of Product data
TLNS	Thin-Layer Navier-Stokes
VCFQ	Variance Constrained Flying Qualities
VTK	Visualization ToolKit format
VTP	Vertical TailPlane

Symbols

Symbol	Definition	Unit
a	Speed of sound	[m/s]
a_{cruise}	Speed of sound at cruise altitude	[m/s]
A_{engine}	Engine frontal area	[m^2]
A_i	CST coefficient	[-]
$\mathbf{A_l}$	Lower surface CST coefficients vector	[-]
$\mathbf{A_u}$	Upper surface CST coefficients vector	[-]
AR	Aspect ratio	[-]
AR_{HTP}	Horizontal tailplane aspect ratio	[-]
AR_{VTP}	Vertical tailplane aspect ratio	[-]
b	Span	[m]
b_e	Elevator span	[m]
b_{HTP}	Horizontal tailplane span	[m]
b_{semi}	Semi span	[m]
b_{VTP}	Vertical tailplane span	[m]
b_{wing}	Wing span	[m]
B_i^n	Bernstein polynomial	[-]
$c_{D_{des}}$	Drag coefficient at the design point	[-]
$c_{D_{engine}}$	Engine drag coefficient	[-]
c_{D_f}	Friction drag coefficient	[-]
$c_{D_{i,des}}$	Induced drag coefficient at the design point	[-]
$c_{D_{0,des}}$	Zero-lift drag coefficient at the design point	[-]
c_{elev}	Elevator chord fraction	[-]
c_f	Friction coefficient	[-]
c_{hinge}	Hinge line chordwise fraction	[-]
c_{HTP}	Horizontal tail volume coefficient	[-]
$c_{HTP,root}$	Horizontal tailplane root chord	[m]
$c_{HTP,tip}$	Horizontal tailplane tip chord	[m]
c_{local}	Local chord	[m]
$c_{L_{app}}$	Lift coefficient at approach	[-]
$c_{L_{cruise}}$	Lift coefficient at cruise	[-]
$c_{L_{des}}$	Lift coefficient at the design point	[-]
c_{L_p}	Rate of change of the roll moment coefficient as a function of the roll rate	[-]
$c_{L_{VTP}}$	Lift coefficient of the vertical tailplane	[-]
$c_{L_{VTP,max}}$	Maximum lift coefficient of the vertical tailplane	[-]
$c_{L_{\alpha_h}}$	Horizontal tail lift curve slope	[-]
c_{L_β}	Rolling moment curve slope	[-]
c_M	Pitching moment coefficient	[-]
$c_{M_{des}}$	Pitching moment coefficient at the design point	[-]
c_{M_q}	Rate of change of the pitching moment coefficient as a function of the pitch rate	[-]
c_{M_α}	Pitching moment curve slope	[-]
$c_{M_{\delta e}}$	Elevator effectiveness	[1/°]
$c_{N_{max}}$	Maximum yawing moment coefficient	[-]
c_{N_r}	Rate of change of the yawing moment coefficient as a function of the yaw rate	[-]
c_{N_β}	Yawing moment curve slope	[-]
$c_{N_{\delta r}}$	Rudder effectiveness	[1/°]
c_{rud}	Rudder chord fraction	[-]
c_{root}	Root chord	[m]
c_{tip}	Tip chord	[m]
c_{VTP}	Vertical tail volume coefficient	[-]

Symbol	Definition	Unit
$c_{VTP_{HTP}}$	Local chord of the VTP at the HTP	[m]
$c_{VTP,root}$	Vertical tailplane root chord	[m]
$c_{VTP,tip}$	Vertical tailplane tip chord	[m]
c_{wing}	Wing chord	[m]
c_{Y_β}	Side force curve slope	[-]
cap_{hyd}	Maximum hydrogen capacity	[kg]
cap_{ker}	Maximum kerosene capacity	[kg]
d_{hinge}	Normalized distance to the hinge	[-]
D	Drag	[N]
D_{des}	Drag at the design point	[N]
$D_{f_{a/c}}$	Aircraft friction drag	[N]
$D_{f_{emp}}$	Empennage friction drag	[N]
$D_{f_{TP}}$	Tailplane friction drag	[N]
$D_{i,des}$	Induced drag at the design point	[N]
F_w	Fuselage width at horizontal tail intersection	[m]
g	Gravitational constant	[N/kg]
g_j	Inequality constraints	[-]
h	Altitude	[m]
H_{HTP}	Relative height of the HTP w.r.t. the VTP	[-]
h_i	Equality constraints	[-]
H_k	Hessian matrix of the objective function	[-]
I_{xx}	Moment of inertia around the x-axis	[kgm^2]
I_{yy}	Moment of inertia around the y-axis	[kgm^2]
I_{zz}	Moment of inertia around the z-axis	[kgm^2]
k_{max}	Maximum number of iterations	[-]
K_{uht}	Constant equal to 1.143 for an all-moving tail, equal to 1.0 otherwise	[-]
K_y	Aircraft pitching radius of gyration	[m]
K_z	Aircraft yawing radius of gyration	[m]
$l_{hyd,TO}$	Hydrogen level at take-off	[-]
$l_{ker,TO}$	Kerosene level at take-off	[-]
L	Lift	[N]
L_{des}	Lift at the design point	[N]
L_{HTP}	Distance between wing quarter-MAC and tail quarter-MAC	[m]
L_{VTP}	Distance from the center of gravity to the aerodynamic center of the vertical tailplane	[m]
M	Mach number	[-]
M_{cruise}	Mach number at cruise	[-]
M_{perp}	Perpendicular Mach number	[-]
M_q	Rate of change of the pitching moment as a function of the pitch rate	[-]
MAC	Mean aerodynamic chord	[m]
n_{ult}	Ultimate load factor	[-]
N_{engine}	Yawing moment by engine thrust	[Nm]
N_{lo}	Number of coordinates on the lower surface	[-]
N_{max}	Maximum yawing moment	[Nm]
N_{up}	Number of coordinates on the upper surface	[-]
N_{VTP}	Yawing moment by vertical tailplane	[Nm]
OEW	Operative empty weight	[kg]
$OEW_{fuselage}$	Fuselage operative empty weight	[kg]
$OEW_{tailless}$	Tailless operative empty weight	[kg]
p_{cruise}	Pressure at cruise altitude	[Pa]
p_k	Direction vector	[-]

Symbol	Definition	Unit
q	Dynamic pressure	[Pa]
q_h	Dynamic pressure at horizontal tail plane	[Pa]
q_{min}	Minimum dynamic pressure	[Pa]
q_∞	Freestream dynamic pressure	[Pa]
R	Range	[m]
Re_{TP}	Reynolds number at the tailplane	[m]
S	Surface area	[m^2]
S_e	Elevator surface area	[m^2]
s_{HTP}	Relative set-back of the HTP root leading edge	[-]
S_{HTP}	Horizontal tailplane surface area	[m^2]
$S_{TP,wet}$	Tailplane wetted area	[m^2]
S_{VTP}	Vertical tailplane surface area	[m^2]
$S_{VTP_{min}}$	Minimum required vertical tailplane surface area	[m^2]
S_{wet}	Wetted area	[m^2]
S_{wing}	Wing surface area	[m^2]
sfc	Specific fuel consumption	[kg/(Ns)]
sfc_{APPU}	Specific fuel consumption of the APPU system	[kg/(Ns)]
$sfc_{APPU,main}$	Specific fuel consumption of the APPU main engines	[kg/(Ns)]
$sfc_{APPU,prop}$	Specific fuel consumption of the APPU propulsor	[kg/(Ns)]
sfc_{neo}	Specific fuel consumption of the A321neo	[kg/(Ns)]
sfc_{v3}	Specific fuel consumption of the A321v3	[kg/(Ns)]
S.M.	Static margin	[-]
T	Thrust	[N]
T_{cruise}	Temperature at cruise altitude	[K]
T_{engine}	Engine thrust	[N]
$(t/c)_{root}$	Thickness to chord ratio at the root	[-]
U_0	Freestream velocity component in longitudinal direction	[m/s]
V	Velocity	[m/s]
V_{app}	Approach velocity	[m/s]
V_{cruise}	Cruise velocity	[m/s]
V_∞	Freestream velocity	[m/s]
W	Weight	[kg]
W_{app}	Weight at approach	[kg]
W_{des}	Weight at the design point	[N]
W_{dg}	Flight design gross weight	[kg]
W_{emp}	Empennage weight	[kg]
W_f	Final weight	[kg]
W_{fuel}	Fuel weight	[kg]
W^0_{fuel}	Initial fuel weight	[kg]
$\widehat{W_{fuel}}$	Normalized fuel weight	[kg]
W_{HTP}	Horizontal tailplane weight	[kg]
W_i	Initial weight	[kg]
$W_{payload}$	Payload weight	[N]
W_{VTP}	Vertical tailplane weight	[kg]
W_{wing}	Main wing weight	[kg]
x	Design vector	[-]
$x_{CG,aft}$	Most aft center of gravity	[-]
$x_{CG,app}$	Center of gravity at approach	[m]
$x_{CG,des}$	Center of gravity at the design point	[m]
$x_{CG,fuel}$	Fuel center of gravity	[m]
$x_{CG,HTP}$	Horizontal tailplane center of gravity	[m]
$x_{CG,hyd}$	Hydrogen center of gravity	[m]
$x_{CG,ker}$	Kerosene center of gravity	[m]

Symbol	Definition	Unit
$x_{CG,OE}$	Operative empty center of gravity	[m]
$x_{CG,OE_{fuselage}}$	Fuselage operative empty center of gravity	[m]
$x_{CG,OE_{tailless}}$	Tailless operative empty center of gravity	[m]
$x_{CG,payload}$	Payload center of gravity	[m]
$x_{CG,VTP}$	Vertical tailplane center of gravity	[m]
$x_{CG,wing}$	Main wing center of gravity	[m]
x_{HTP}	x-coordinate of the HTP leading edge root point	[m]
x_i	Design variables	[-]
x_k	Current solution	[-]
x_l	Lower bound vector	[-]
x_{NP}	Neutral point x-coordinate	[m]
x_u	Upper bound vector	[-]
x_0	Initial solution	[-]
y_{engine}	Distance from the center of gravity to the engine centerline	[m]
y_i	Discipline output value	[-]
y_{MAC}	y-coordinate of the mean aerodynamic chord	[m]
z_{HTP}	z-coordinate of the HTP leading edge root point	[m]
α	Angle of attack	[°]
α_k	Step length	[-]
$\dot{\alpha}$	Angle of attack rate of change	[°/s]
γ	Flight path angle	[°]
Γ	Circulation	[-]
δ	Deflection angle	[°]
δ_e	Elevator deflection	[°]
δ_r	Rudder deflection	[°]
$\Delta c_{L_{flaps}}$	Difference in lift coefficient due to flap deployment	[-]
ϵ	Tolerance threshold	[-]
ϵ/c	Airfoil fit error	[-]
ζ	Normalized z-coordinate	[-]
ζ_{dr}	Dutch roll damping ratio	[-]
ζ_p	Phugoid damping ratio	[-]
ζ_{sp}	Short period damping ratio	[-]
η_h	Horizontal tail dynamic pressure ratio	[-]
θ	Pitch angle	[°]
λ	Taper ratio	[-]
$\Lambda_{c/4}$	Quarter chord sweep angle	[°]
Λ_{HTP}	Horizontal tailplane leading edge sweep angle	[°]
Λ_{VTP}	Vertical tailplane leading edge sweep angle	[°]
μ	Viscosity	[Ns/m^2]
μ_{cruise}	Viscosity at cruise altitude	[Ns/m^2]
ρ	Density	[kg/m^3]
ρ_{cruise}	Pressure at cruise altitude	[kg/m^3]
ρ_{gr}	Pressure at ground level	[kg/m^3]
ρ_∞	Freestream density	[kg/m^3]
τ	Minimum gradient norm	[-]
τ_e	Elevator angle of attack effectiveness	[-]
τ_{roll}	Roll mode time constant	[-]
$\phi_{APPU,prop}$	APPU propulsor thrust fraction	[-]
ψ	Normalized x-coordinate	[-]
ψ_{eq}	Equispaced normalized x-coordinate	[-]
ψ_{hinge}	Normalized x-coordinate of the hinge	[-]
$\omega_{n,sp}$	Short period natural frequency	[Hz]

1

Introduction

The APPU project aims to lower the threshold of installing Boundary-Layer-Ingesting (BLI) and hydrogen-driven propulsion systems in the short term. This is done by replacing the Auxiliary Power Unit (APU) with an Auxiliary Power & Propulsion Unit (APPU). This means that the APU in the tail cone of a passenger aircraft is replaced by a BLI propulsor with an engine. This engine delivers around 10% of the thrust during cruise as well as the auxiliary power that was previously provided by the APU. In addition, the APPU uses hydrogen to power the engine, which is stored in a tank in the tail cone of the aircraft. The reduction in CO_2 emissions is estimated to be approximately proportional to the APPU thrust share (10% during cruise). In addition, overall efficiency would improve, resulting in additional savings [1].

In order to study these concepts, the Airbus A321neo is taken as a reference baseline. The implementation of the hydrogen engine and the BLI propulsor results in some changes that need to be made to the baseline reference aircraft. One of these changes is driven by the fact that no elements of the horizontal tail plane (HTP) can cross the fuselage. As a result, the HTP must move onto the vertical tail plane (VTP) to form either a cruciform tail or a T-tail [1]. An additional constraint due to the implementation of the BLI propulsor is that no part of the empennage can be aft of the propeller. This is to avoid the loss of control and stability in case the propeller fails and strikes the empennage. Redesigning the empennage to meet these requirements is the subject of this thesis project.

The research objective of this study is to investigate how an optimal empennage design for an aircraft with an APPU system differs from an optimal design for an aircraft that does not have an APPU system. Furthermore, this study aims to find what implications the location of the tank and propulsor have on the empennage design compared to the empennage of a conventional passenger aircraft.

chapter 2 introduces the background and outlines related research on empennage optimization, along with the research questions guiding this study. The theoretical foundation and overall methodology are presented in chapter 3, followed by the practical implementation of the individual components in chapter 4. chapter 5 discusses the outcomes of the optimization, including two validation studies comparing selected results with higher-fidelity methods. Finally, the study is concluded in chapter 6.

2

Research Objectives

The design of an aircraft empennage is a critical aspect of overall aerodynamic performance, stability, and control. As aviation technology advances and sustainability concerns drive innovation, new methodologies are required to optimize empennage configurations beyond traditional design approaches. This chapter outlines the research objectives that guide this study, focusing on the application of Multidisciplinary Design Optimization (MDO) to the development of a cruciform or T-tail empennage for the APPU aircraft.

This chapter begins with a review of the state-of-the-art methods in empennage design in section 2.1, highlighting the limitations of conventional techniques such as the tail volume coefficient method. The discussion then shifts to the identified research gaps, particularly in optimizing empennage configurations with constraints related to novel propulsion systems and hydrogen storage integration. Based on these gaps, the problem statement and research questions are formulated to address how an optimal empennage design for the APPU aircraft differs from conventional designs in section 2.2.

2.1. State-of-the-art

A common method to size the empennage during conceptual design is to use tail volume coefficients. Raymer [2] describes the method of tail volume coefficients in his work. It enables the designer to compare the design to historical data. He states that the primary purpose of the tail is to counteract the moments produced by the wing. In that way, it would be logical if the tail size is somehow related to the wing size. The magnitude of the force generated by the tail increases proportionally to the area of the tail. Consequently, the effectiveness of the tail is determined by multiplying the tail area by the tail moment arm. This product has units of volume, hence the name 'tail volume coefficients'. In order to obtain a non-dimensional coefficient, it needs to be divided by something else with the units of volume. Since the tail size is related to the wing size in some way, it makes sense to divide it by the wing size multiplied by something with units of length. For the horizontal tail, this is the mean chord length of the wings because the pitching moment that must be countered by the horizontal tail is most directly proportional to the wing chord. On the other hand, the yawing moments that must be countered by the vertical tail are most directly related to the wing span. This results in equations Equation 2.1 and Equation 2.2 for the horizontal and vertical tail volume coefficients, respectively.

$$c_{HTP} = \frac{L_{HTP} S_{HTP}}{b_w ing S_w ing} \tag{2.1}$$

$$c_{VTP} = \frac{L_{VTP} S_{VTP}}{c_w ing S_w ing} \tag{2.2}$$

Typical values for transport aircraft are 1.00 for the horizontal tail volume coefficient and 0.09 for the vertical tail volume coefficient. In the case of a T-tail, the vertical tail volume coefficient can be reduced by approximately 5% as a result of the end-plate effect, while the horizontal tail volume coefficient can be decreased by approximately 5% due to the undisturbed airflow experienced by the horizontal surface.

The method of tail volume coefficients is valuable when one needs to know quickly how big the horizontal and vertical tailplane approximately should be. However, the method still has some shortcomings. First of all, the method of tail volume coefficients is an empirical method that is based on historical data and thus has limited meaning from a physics point of view. Additionally, the method is limited to calculating surface areas, but does not provide other variables such as aspect ratios, taper ratios, sweep angles, and airfoil shapes. Finally, the size and shape of the elevator and rudder are not provided by the tail volume method. Simplified tail sizing processes, such as the tail volume coefficient method, are often applied in aircraft initial design tools to avoid the complex and iterative process [3, 2].

There exist many more methods for the conceptual design of an empennage. One option to achieve an improved conceptual design for an empennage is to apply multidisciplinary design optimization. MDO is not a new concept to the aerospace industry. However, when it comes to initial aerodynamic design, it is applied more often to the main wing than to the empennage. Detailed design of the tail with stability and control constraints is just more complex than the detailed design of the main wing [4]. MDO can help to solve the shortcomings of the tail volume method to a certain degree by combining some disciplines that are relevant for empennage design. All the variables that the tail volume method does not provide can be found when applying MDO depending on the parameterization that is applied to the problem. MDO can be applied to a great variety of fidelity levels for the different disciplines. Computationally cheap empirical methods can be used to speed up the process, or more computationally expensive physics-based methods can be used for increased precision and physical meaning. In addition, the design of the elevator and rudder can be easily included by expanding the design space to include some additional variables. Finally, whereas the tail volume method only provides a plausible design, MDO provides a design that is optimized to a (local) optimum.

Galloway [5] applied optimization to control, stability, and performance of conceptual aircraft design. Rather than focusing on the optimization of the empennage alone, Galloway [5] developed a design optimization capability that optimized the whole aircraft initial design. The tool is able to size the aircraft, and control the location and dimensions of the empennage, control surfaces, and landing gear. In addition, the tool has the ability to distribute systems and components. The analysis of different disciplines is carried out on the designs generated by the tool. These disciplines include: applied aerodynamics, weight and balance, mission analysis, performance, and static and dynamic stability and control [5]. To obtain low computational cost, Galloway used simple equations to evaluate these disciplines. For example, the weight and balance are based on empirical relations. The applied aerodynamics, mission performance, and stability and control are based on simple physics-based relations or semi-empirical methods. An example of a simple physics-based relation that is applied is the standard method for drag polar calculation to find the drag coefficient. There are still some limitations to Galloway's [5] tool. First, the tool is limited to general aviation aircraft, and thrust effects are not considered in stability and control analyses. In addition, it is not able to design active control systems.

Morris [6] developed a control & stability module at Virginia Tech that could be implemented in an MDO tool for advanced aircraft conceptual design. The module treats both static and dynamic stability & control. An innovative method, Variance Constrained Flying Qualities (VCFQ), was developed to include closed-loop dynamic performance metrics. A limitation in the work of Morris [6] is that the horizontal and vertical tailplane areas are sized for the initial configuration and are kept constant throughout the optimization. Morris [6] performed an example design study on a Boeing 737-800 to test the new stability & control module. The objective of the study is to redesign the horizontal and vertical tailplane to minimize the aircraft gross weight and trimmed drag coefficient. In this study, the static stability requirements on the static margin imposed by federal regulations are assumed to be relaxed. Morris [6] allows the aircraft to be neutrally stable or slightly unstable, assuming that a well-designed control system can overcome these instabilities.

Morris [6] mainly used the NASTRAN aeroelastic solver to retrieve the required data. NASTRAN is a finite element analysis structural solver that is coupled with some aerodynamic solvers. For subsonic flows, NASTRAN applies a Doublet Lattice Method (DLM). Modifications are made to the standard DLM in order to take wing-body interference effects into account. In addition to NASTRAN, Digital DATCOM

is used to calculate the drag coefficient and certain stability derivatives, which NASTRAN cannot produce. Digital DATCOM is a program that computes stability & control related parameters based on a semi-empirical method. It uses results from existing aircraft and physics-based relationships with empirical corrections to accomplish this.

The 737-800 is the second-longest aircraft within the 737 family [7]. The empennage for an aircraft family is often designed for the shorter aircraft within the family since they have a shorter tail length. If the empennage is big enough to counter the moments on the short aircraft with the short moment arm, it should be big enough to counter the moments on the longer versions with longer tail lengths as well. Consequently, the empennage is over-designed for the longer versions within the family. The results of the example study were promising. The horizontal tailplane area was reduced by 36% and the vertical tailplane area by 32%. The gross aircraft weight was reduced by $2392kg$. A total drag reduction of approximately 12% was obtained compared to the baseline configuration. Throughout the entire flight envelope, the static margin was marginally stable or unstable. This indicates that the empennage is indeed larger than necessary for the long Boeing 737-800. However, it is important to remember that relaxed static stability requirements were considered for this study. It is unclear how much of the drag and weight reduction is a result of the relaxed static stability requirements and how much is a result of the over-designed original empennage.

Cosenza [8] created a tool for handling qualities optimization based on a modification of the Routh-Hurwitz criterion. The algebraic relations that proceed from the modified Routh-Hurwitz criterion are set as constraints during the optimization process. The module focuses on designs with excellent control anticipation parameters and short period damping ratio. The objective of the optimization process is to minimize the horizontal tailplane zero-lift drag, induced drag, and weight. Cosenza [8] showed that it is possible to consider the handling qualities of the aircraft during conceptual design and still gain on performance. It should be noted that one of the limitations of Cosenza's [8] work is that it focuses solely on longitudinal stability and control.

Denieul [9] and Garmendia [10] also worked on multidisciplinary design optimization including stability & control constraints. However, their work focuses on the optimization of control surfaces of a blended wing body configuration. This is of less interest for this thesis project since the aircraft configuration is already determined by the APPU project.

Liu and Jiang [4] stated that an aircraft's empennage is often sized using volume coefficient methods in conventional aircraft design processes. They proposed an improved method for the conceptual design of an empennage by applying multidisciplinary design optimization. Stability and control requirements were taken into account in the form of constraints. The constraints are based on regulations and the fundamental functionalities of the empennage. The aerodynamic drag polar is estimated using component-based building methods. The wing and empennage's induced drag is calculated with a potential flow solver including fuselage and nacelles corrections. Semi-empirical methods with high-fidelity corrections are used for the viscous drag and wave drag. The primary wing and fuselage structure is analyzed using analytical methods, whereas the secondary structural weight is analyzed using semi-empirical methods. The optimization of the empennage was combined with the optimization of the main wing as well. An example study was performed where the initial design was based on reference data of a medium-range transport aircraft [11]. This resulted in a saving of 9% in block fuel weight and a reduction of 3% in the maximum take-off weight compared to the initial design. This shows the gains that can still be made in carbon reduction by optimizing the empennage in the conceptual design phase.

There still exists a literature gap that is discussed in this section that is relevant to the empennage design for the APPU project. Firstly, all of the literature mentioned above focuses either on the optimization including stability & control constraints of an aircraft with a conventional tail or a blended wing body configuration. None of the literature treats a cruciform or T-tail configuration which is forced due to the location of the hydrogen tank in the APPU project. In addition, none of the work discussed has limitations on the location of the empennage due to the presence of a propulsor at the rear of the fuselage. Second, during the optimization processes discussed in the literature, the focus is mainly on the optimization of the empennage planform, control surfaces, or both. If the airfoil is optimized, it is no

more than the thickness-to-chord ratio that is varied. This thesis project will aim to offer more freedom to the airfoil to further optimize its shape. Finally, increasing the fidelity of the analysis tools used during the optimization process is often one of the recommendations for future work in the discussed literature. This thesis project aims to increase the fidelity of the aerodynamic solver.

2.2. Problem Statement & Research Goals

The research objective of this thesis project is to investigate how an optimal empennage design for an aircraft equipped with an APPU system differs from an optimal empennage design for an aircraft without such a system. Combined with the literature gaps that are found in section 2.1, this leads to the formulation of some research questions that this thesis project will aim to answer. The main research question is stated below:

Which implications does the inclusion of an APPU system have on the optimal empennage design for a commercial aircraft?

Some sub-questions have been formulated to help answer the main research question. Morris [6] redesigned the empennage of a Boeing 737-800 to test his new stability and control module. As stated in section 2.1, the empennage for larger members of aircraft families is often over-designed. As a result, Morris [6] was able to significantly reduce the size and drag of the empennage. This study uses the Airbus A321neo as a baseline. Similar to the Boeing 737-800, the A321neo is the longest aircraft within the A320 family [12]. This leads to the first two research questions.

What is an optimal conventional, T-tail, or cruciform empennage design for the A321neo when optimized to reduce the fuel required to cover the design range?

How much can the surface area of the A321neo empennage be reduced and what is the effect on the total drag?

The addition of the hydrogen tank and the propulsor for the APPU aircraft will add weight to the rear of the fuselage of the A321neo baseline. As a result, the center of gravity will move aft and the main wing needs to be shifted back. This shortens the tail length and thus the moment arm of the empennage, leading to the next research question:

How does the additional weight due to the hydrogen tank and propulsor, and the repositioning of the main wing influence the optimal empennage design?

The design of the empennage for the APPU project is constrained by the location of the propulsor and the hydrogen tank. In case the propulsor fails, the blades should not be able to strike the empennage. This means that the empennage should be entirely in front of the propulsor. In addition, the hydrogen tank will be located in the tail cone of the aircraft, taking up the space where the wingbox of the horizontal tail is usually located. This means that the empennage design for the APPU aircraft is limited to a T-tail or cruciform configuration. These requirements form the basis of the following research question:

How does the location of the hydrogen tank and the propulsor influence the optimal empennage design of APPU-equipped aircraft?

In the existing literature discussed in section 2.1, the influence of the optimizer on the airfoil geometries was limited to the thickness to chord ratio at most. This offers limited freedom to the optimizer to adjust the airfoils of the vertical and horizontal tailplane. The following sub-question aims to explore this design space in more detail:

Which airfoils for the horizontal and vertical tailplane offer the best performance for the aircraft when optimized to reduce the fuel required to cover a certain design range?

Finally, an often recurring recommendation for future work is to increase the fidelity level of the aerodynamic analysis tool that is used in the optimization study. The following sub-question helps to explore these options:

Which level of fidelity for the aerodynamic analysis tool is obtainable within an optimization tool?

3

Methodology

Multidisciplinary design optimization is used to find optimal empennage designs for different aircraft configurations to answer the research questions posed in section 2.2. MDO applies optimization algorithms to solve design problems that involve multiple disciplines simultaneously. By optimizing all disciplines simultaneously rather than sequentially, trade-offs can be made between different disciplines, often resulting in superior design. This chapter aims to provide a deeper insight into the theory behind some building blocks that together form a method to solve the research questions through MDO. First, the objective of the optimization algorithm is discussed in section 3.1. Next, the different disciplines that are considered in this study are presented in section 3.2. MDO requires some kind of architecture to let all disciplines communicate with each other. The MDO architecture for this study is set forth in section 3.3. Finally, the optimization algorithm that navigates through this architecture is described in section 3.4.

3.1. Objective

For the optimization algorithm to find an optimum, an objective function must be given that it can minimize. The results of the optimization process can differ greatly depending on the selection of the objective function. Two of the most frequently applied objectives when it comes to aerodynamic shape optimization are the maximum takeoff weight and the fuel mass. For this study, it has been decided to use a normalized version of the fuel mass. The reason for choosing the fuel mass as the objective is twofold. First, it is important to keep in mind the goal of the APPU project. This is to reduce the emissions of an aircraft that is equipped with the APPU system compared to the baseline aircraft. One of the most effective ways to reduce emissions is by reducing the amount of fuel that is being burned. Secondly, the fuel mass can be estimated from some basic variables that can be obtained from a relatively low number of different disciplines, keeping the complexity of the MDO problem to a minimum.

The fuel mass required for an aircraft is dependent on the aircraft's mass and aerodynamic efficiency. If an aircraft has high aerodynamic efficiency, there is less drag that needs to be overcome by the engines, and thus less fuel needs to be burned. Similarly, if an aircraft weighs less, less lift needs to be generated by the wing, and thus less drag is generated as well. This leads to a total of three disciplines to be able to evaluate the objective function: weight to calculate the empennage structural weight, aerodynamics to obtain the aerodynamic efficiency, and performance to calculate the fuel weight based on the aerodynamic efficiency and the aircraft's weight. More details on these disciplines are provided in section 3.2.

The fuel mass is normalized by dividing it by the fuel mass required for the initial configuration at the beginning of the optimization process. This can be seen in Equation 3.1. Here, $\widehat{W}_{fuel}$ is the normalized fuel weight, W_{fuel} is the fuel weight for the current design at the objective evaluation, and W^0_{fuel} is the initial fuel weight. The reason for this is that the optimization convergence criterion can be applied more easily to relative values rather than absolute values.

$$\widehat{W}_{fuel} = \frac{W_{fuel}}{W^0_{fuel}} \tag{3.1}$$

3.2. Disciplines

Multiple disciplines can be identified that play a role during the optimization of an empennage. Four different disciplines are identified for this study: weight, aerodynamics, stability and control, and performance. The weight discipline estimates the structural weight of the empennage. The aerodynamic discipline returns the aerodynamic performance indicators of the aircraft configuration. The stability and control discipline is tasked with calculating stability and control derivatives required for the constraints such that the empennage meets its purpose. Finally, the performance discipline converts the structural weight estimate together with the aerodynamic performance indicators into the fuel load required to cover the design range. This section aims to provide a deeper insight into the methods that are selected for each of these disciplines.

3.2.1. Weight

A reliable method to estimate the weight of the empennage is of great importance for the optimization of the empennage. Without it, the optimizer tends to move to very slender and thin lifting surfaces. These have great aerodynamic properties but would end up being too heavy in reality. The weight of the aircraft's empennage is estimated by an empirical method described by Raymer [2].

Raymer [2] separates the empennage weight into a weight estimate for the horizontal tail and a weight estimate for the vertical tail. The estimates for the horizontal and vertical tails can be seen in Equation 3.2 and 3.3 respectively. Note that these equations use British units and that the results are in pounds. The Raymer method is dependent on a relatively large number of variables that are controlled by the optimizer, making it sensitive to changes in the design vector. In addition, it is able to deal with the HTP at any height, ranging from conventional tails to T-tails.

$$\begin{aligned} W_{HTP} = {} & 0.0379 K_{uht} \left(1 + F_w / b_{HTP}\right)^{-0.25} W_{dg}^{0.639} n_{ult}^{0.10} \\ & \times S_{HTP}^{0.75} L_{HTP}^{-1.0} K_y^{0.704} \left(\cos \Lambda_{c/4,HTP}\right)^{-1.0} \\ & \times AR_{HTP}^{0.166} \left(1 + S_e / S_{HTP}\right)^{0.1} \end{aligned} \tag{3.2}$$

$$\begin{aligned} W_{VTP} = {} & 0.0026 \left(1 + H_{HTP}\right)^{0.225} W_{dg}^{0.556} n_{ult}^{0.536} L_{HTP}^{-0.5} \\ & \times S_{VTP}^{0.5} K_z^{0.875} \left(\cos \Lambda_{c/4,VTP}\right)^{-1.0} AR_{VTP}^{0.35} \left(t/c\right)_{root}^{-0.5} \end{aligned} \tag{3.3}$$

The meaning of every symbol used in Equation 3.2 and 3.3 is listed below:

- AR_{HTP}: Horizontal tail aspect ratio
- AR_{VTP}: Vertical tail aspect ratio
- b_{HTP}: Horizontal tail span
- F_w: Fuselage width at horizontal tail intersection
- H_{HTP}: Relative height of the HTP w.r.t. the VTP: 0.0 for a conventional tail, 1.0 for a T-tail
- K_{uht}: Constant equal to 1.143 for an all-moving tail, equal to 1.0 otherwise
- K_y: Aircraft pitching radius of gyration
- K_z: Aircraft yawing radius of gyration
- L_{HTP}: Distance between wing quarter-MAC and tail quarter-MAC
- n_{ult}: Ultimate load factor, or 1.5 times the limit load factor
- S_e: Elevator surface area
- S_{HTP}: Horizontal tail surface area
- S_{VTP}: Vertical tail surface area
- $(t/c)_{root}$: Thickness to chord ratio at the root

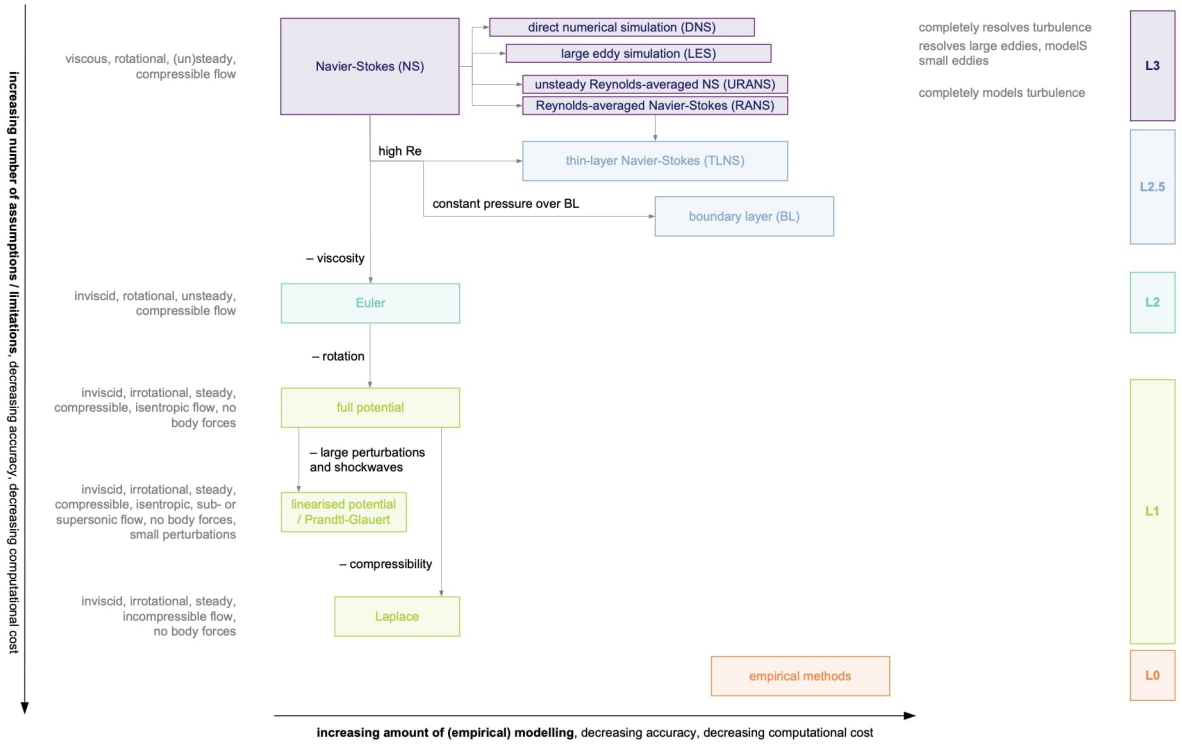

Figure 3.1: Overview of different aerodynamic models [13].

- W_{dg}: Flight design gross weight
- W_{HTP}: Horizontal tail weight
- W_{VTP}: Vertical tail weight
- $\Lambda_{c/4,HTP}$: Horizontal tail sweep at quarter-MAC
- $\Lambda_{c/4,VTP}$: vertical tail sweep at quarter-MAC

3.2.2. Aerodynamics

It is the aerodynamics discipline's task to analyze the aerodynamic performance of the aircraft. An aerodynamic solver is selected to calculate the aerodynamic performance indicators throughout the optimization process, i.e., lift, drag, and moment coefficients. There exists a wide variety of aerodynamic models and solution methods. However, there are differences in complexity and fidelity levels between them. Understanding the inner workings, underlying presumptions, and techniques of models and solution methods is crucial, particularly when using them to inform decisions, since this will make it possible to evaluate the output at the appropriate value. One of the goals of this study is to investigate which fidelity level for the aerodynamic solver can be attained for optimization studies such as this. Therefore, multiple solvers need to be tested at different fidelity levels.

Flow Models

Three fundamental principles generally determine flows: conservation of mass, momentum, and energy. However, there are differences in how these conservation principles are converted into three different equations: an energy equation, a momentum equation, and a continuity equation [13]. Figure 3.1 gives a hierarchical overview of different aerodynamic models. Descending along the vertical axis, there are more assumptions in the flow models. This results in lower computational costs and simplifies the flow model. Along the horizontal axis, the degree to which the model is determined by empirical models increases, resulting in a reduced computational cost as well.

The Navier-Stokes equations are classified as level L3 and are considered the highest fidelity flow models available. One step below the Navier-Stokes equations are the viscous thin-layer Navier-Stokes (TLNS) and boundary layer (BL) equations. Here some additional assumptions are made in order to

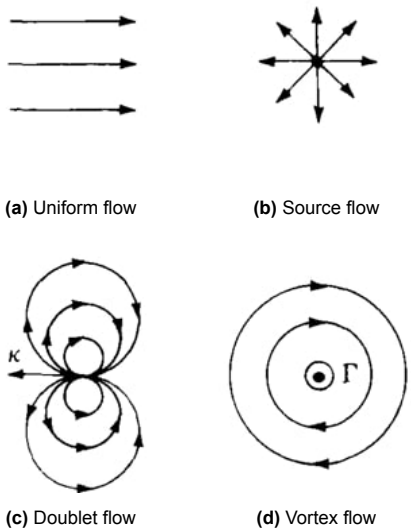

(a) Uniform flow **(b)** Source flow

(c) Doublet flow **(d)** Vortex flow

Figure 3.2: Elementary solutions [17]

be able to perform viscous simulations at a relatively low cost. Peerlings [13] positioned these models between L2 and L3 since they are of a higher fidelity level than other L2 models, but not as detailed as the Navier-Stokes equations. L2 comprises the Euler equations which ignore viscous effects. One more level down in L1, one finds the full potential flow equations first, which assume irrotational flow. There are two additional models in L1. The linearized potential, or the Prandtl-Glauert equation, is a simplification of the full potential equations. The Laplace equations assume incompressible flow. Finally, empirical methods are gathered at the L0 level.

Solution Methods

Different solution methods can be used to solve the flow models presented in Figure 3.1. These solution methods can be divided into two main categories: linear and non-linear methods. Both categories are presented in this section.

Non-linear solution methods are used to solve the non-linear flow models in the diagram in Figure 3.1. Non-linear models are the models with high fidelity levels. This includes everything from the direct numerical simulation of the Navier-Stokes equations to the full potential equations. In general, they all work similarly. The flow domain is split up into a finite number of elements. The conservation of momentum, mass, and energy is then applied to all elements [14]. The most popular non-linear solution methods include finite difference methods [15], finite element methods, and finite volume methods [16]. The disadvantage of non-linear solution methods is that they are used to solve non-linear flow models, which are computationally relatively expensive. For this reason, non-linear methods are ruled out for this optimization study, where many simulations need to be run.

When using linear flow models, complex flows can be solved by superimposing multiple known standard solutions to simple flows. Anderson [17] describes a couple of these elementary solutions. They can be seen in Figure 3.2. Uniform flow is a flow that is coming from one direction and travels at the freestream velocity. A source flow is flow coming out of a point that travels outward radially. A doublet is two sources at the same point of equal, but opposite strength. Finally, a vortex flow is a flow with concentric streamlines [17].

Out of these elementary flow solutions, only vortex flow is capable of generating lift. This is due to the fact that circulation around a vortex flow's streamline is finite and by the Kutta-Joukowski theorem's relationship between circulation and lift, which is given in Equation 3.4.

$$L = \rho_\infty V_\infty \Gamma \tag{3.4}$$

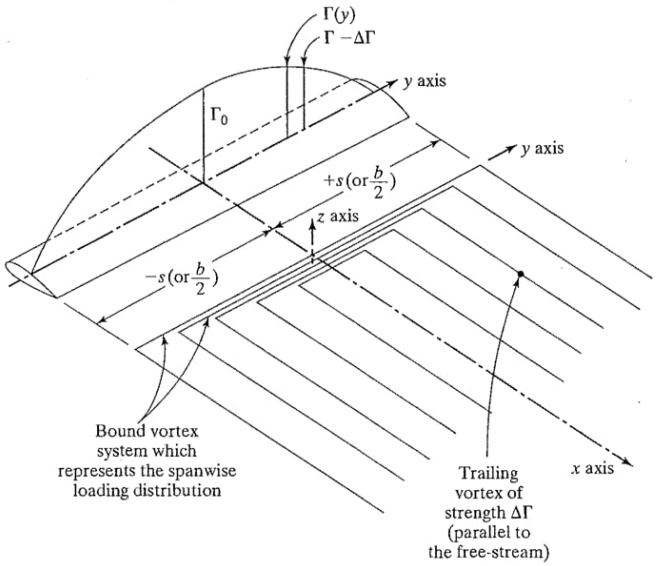

Figure 3.3: Super positioning of multiple horseshoe vortices [18].

Lifting line theory replaces lifting surfaces with a vortex filament that runs through the aerodynamic center of the wing sections. As mentioned before, vortex filaments have to continue to infinity. To match this requirement, two vortices are located at the wing tips that continue for infinity downstream. This way, the vortex filament can be bound between the span of the lifting surface and still be infinite. This is called a horseshoe vortex [13].

However, one horseshoe vortex is not able to accurately model the lift distribution of a lifting surface. To describe the lift distribution more accurately, multiple horseshoe vortices are superimposed. This is visualized in Figure 3.3. The vortex strength distribution can be made continuous by superimposing an infinite number of horseshoe vortices. The vortices that are shed downstream create a vortex sheet that can be used to calculate the lift and induced drag [17].

The lifting line theory is capable of providing acceptable results for straight wings with an aspect ratio greater than 4 [17]. Unfortunately, its predictions are less accurate for other wing geometries, which significantly limits its applicability. These limitations can be omitted by positioning multiple lifting lines next to each other in chordwise direction. All these lifting lines combined form a lifting surface where its strength is dependent on both the spanwise and chordwise location. It is also known as the lifting surface theory [13].

At every point on the wing, normal velocity is induced by all the horseshoe vortices that form the lifting surface and wake vortex sheet. The resultant velocity field should be tangent to the wing. There are two main disadvantages to the lifting line and the lifting surface theory. First of all, they assume thin airfoils. Secondly, they assume linear lift slopes. The last assumption only holds for small angles of attack. These limitations limit their applicability for an empennage optimization study where high angles of attack can occur and ideally the thickness of the wing elements and fuselage is also considered when analyzing the aerodynamic performance.

The vortex lattice method works in a similar way as the lifting line theory. The difference, however, is that VLM divides the lifting surface into quadrilateral panels. A horseshoe vortex is placed on the quarter chord line of every panel. This can be seen in Figure 3.4. The strength of every horseshoe vortex is calculated based on the boundary condition that the flow should be tangent at 3/4 chord. The lift and induced drag can be determined from the strength of these vortices. VLM is a simpler method than LST due to the lack of overlapping horseshoe vortices. Again, the disadvantage is still that it assumes thin airfoils since it still relies on the same principles [15]. As a result, its applicability for this

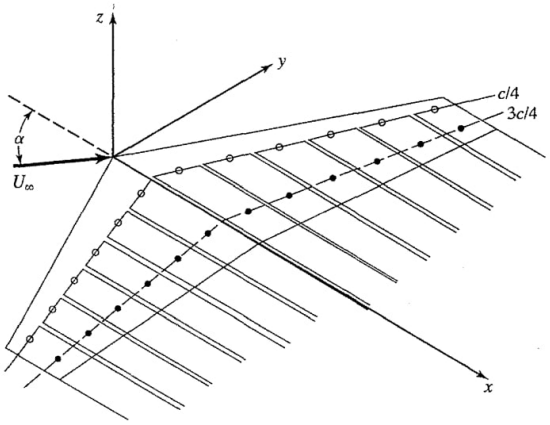

Figure 3.4: Vortex Lattice method applied to a swept wing [18].

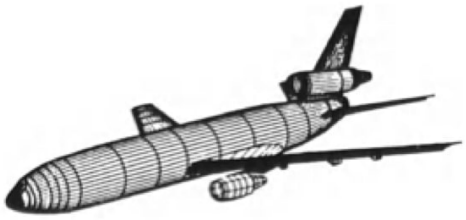

Figure 3.5: Panel method applied to a McDonnell Douglas DC-10 [20].

study is limited due to the same reasons as for lifting line and surface theory.

Similar to VLM, the panel method divides the geometry into panels and a singularity is added at each panel. The type of singularity depends, for instance, on whether it is a lifting or non-lifting surface. The strength of every singularity is again solved with a set of equations based on boundary conditions [19]. The panel method is visualized in Figure 3.5 where it is applied to a McDonnell Douglas DC-10. The main advantage that the panel method has over the other linear methods that have been discussed here is that it is able to handle three-dimensional geometries [20]. This makes it capable of dealing with thicker airfoils, fuselages, and nacelles. The panel method is selected as the aerodynamic solution method for this study due to its quickness advantage over non-linear solution methods and its ability to deal with three-dimensional geometries.

FlightStream

Flightstream is an enhanced panel method solver developed by Research in Flight. It is able to capture boundary layer aerodynamics, flow separation, and post-stall aerodynamics. It does this by applying a physics-based fully viscous-coupled non-linear flow model. Capturing non-linear aerodynamics, onset of stall, prediction of $C_{L_{max}}$ and post-stall loads are all included in the viscous coupled capabilities [21].

In addition to having a faster calculation time than more complex computational fluid dynamics (CFD) solvers, FlightStream has the advantage of being able to model with greater fidelity than conventional vortex lattice tools for conceptual design. FlightStream can support both detailed models, such as PTC Creo computer-aided design (CAD) models, and simplified models, such as Open VSP models [22]. FlightStream is also compatible with ParaPy, which is used to generate the geometries throughout the optimization process. More information on FlightStream and its implementation in this study is provided in subsection 4.4.1.

AVL

Athena Vortex Lattice, or AVL in short, is a flow solver whose main applications are quick aerodynamic analysis and aircraft configuration evaluation, developed by Harold Youngren and Mark Drella. As the name suggests, AVL applies a vortex lattice method. This makes it mainly applicable to thin lifting

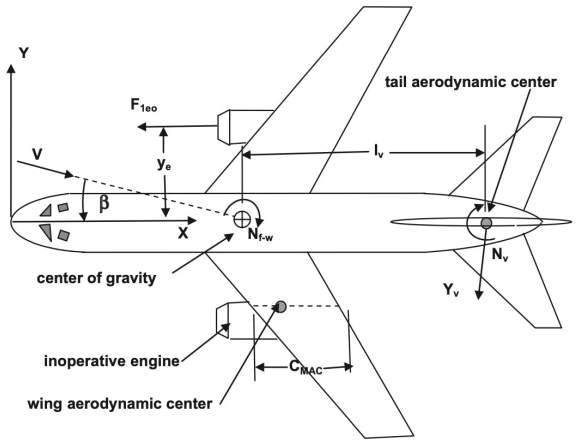

Figure 3.6: Forces acting on an aircraft with one engine inoperative [26]

surfaces at modest angles of attack and sideslip. In addition to thin lifting surfaces, AVL has the ability to analyze slender bodies such as fuselages. It is standard practice, however, to neglect the fuselage and connect the two sides of the wing when a fuselage is expected to have little influence on the aerodynamic loads. AVL applies Trefftz-plane analysis for drag and efficiency calculations [23]. Just like FlightStream, AVL is integrated with ParaPy. The main limitation of AVL for this study is its Prandtl-Glauert compressibility model, suitable for the subsonic domain. Transonic conditions are possibly occurring at the design Mach number of 0.78. More information on AVL and its implementation in this study is provided in subsection 4.4.2.

3.2.3. Stability & Control

An aircraft's empennage has three main functions that it needs to fulfill. It needs to provide longitudinal and directional trim, stability, and control. This subsection will discuss which requirements need to be fulfilled for each of the functions of the empennage. First, the requirements for ensuring that the aircraft can be trimmed are presented. Next, the stability requirements are discussed. Then, the requirements for the controllability of the aircraft are shown. The subsection is concluded with the selection of a solver to calculate the required stability and control derivatives.

Trim

One of the necessities for a safe flight is trim. When an aircraft is in trim, it either continues to go in the intended direction or follows a desired trajectory. In simpler terms, the airplane is considered to be in trim when the sums of all forces and moments are equal to zero [24]. To obtain longitudinal trim, there is one requirement. The pitching moment coefficient should be zero at the angle of attack where the lift equals the weight of the aircraft, or $c_M = 0$ at $c_{L_{cruise}}$ [25]. $c_{L_{cruise}}$ must be such that the lift at the design point is equal to the design weight. Equation 3.5 and 3.6 should be valid at the design point for longitudinal stability.

$$L_{des} = W_{des} \tag{3.5}$$

$$c_{M_{des}} = 0 \tag{3.6}$$

An aircraft is considered to be in directional trim when the net yawing moment around the vertical axis is zero. The design point for directional trim is the one engine inoperative situation. The forces acting on the aircraft in this situation are shown in Figure 3.6. In order to obtain directional trim, the moments around the center of gravity created by these forces need to add up to zero. There are two forces that create a moment around the center of gravity visible in Figure 3.6. First, there is the thrust force from one engine, T_{engine}. The moment it creates around the aircraft's center of gravity is shown in Equation 3.7 where y_{engine} is the distance from the center of gravity to the engine centerline.

$$N_{engine} = T_{engine} y_{engine} \tag{3.7}$$

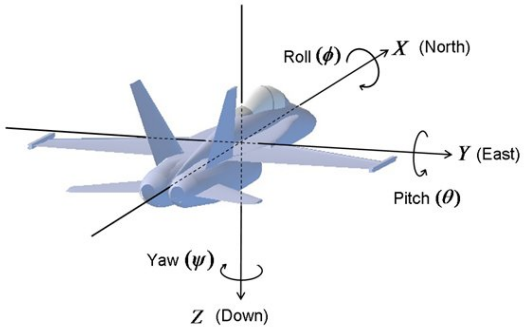

Figure 3.7: Coordinate system of an aircraft with rotational motions [27].

The second force visible in Figure 3.6 is the lift force generated by the vertical tailplane. It also creates a moment around the aircraft's center of gravity shown in Equation 3.8 where L_{VTP} is the distance from the center of gravity to the aerodynamic center of the vertical tailplane.

$$N_{VTP} = -qc_{L_{VTP}} S_{VTP} L_{VTP} \tag{3.8}$$

These two moments need to add up to zero in order to obtain directional trim with one engine inoperative. In order to find the minimum surface area for the vertical tailplane, the maximum lift coefficient of the VTP and the minimum dynamic pressure should be considered. This can be solved for the VTP surface area resulting in Equation 3.9.

$$S_{VTP_{min}} = \frac{T_{engine} y_{engine}}{q_{min} c_{L_{VTP,max}} L_{VTP}} \tag{3.9}$$

Equation 3.9 can be extended in order to take into account the drag created by the inoperative engine. This results in Equation 3.10 [4].

$$S_{VTP_{min}} = \frac{T_{engine} y_{engine} + q_{min} c_{D_{engine}} A_{engine} y_{engine}}{q_{min} c_{L_{VTP,max}} L_{VTP}} \tag{3.10}$$

Stability

Stability can be divided into three categories: longitudinal, lateral, and directional stability. Each of these poses its own requirements on the empennage. A coordinate system of an aircraft as well as its rotational motions is shown in Figure 3.7. Longitudinal stability refers to the stability of rotational motion around the y-axis and linear motions in the xz-plane. Lateral stability refers to the stability of rotational motion around the x-axis and linear motion in the yz-plane. Finally, directional stability refers to the stability of rotational motion around the z-axis and linear motion in the xy-plane [24]. In contrast to the trim requirements before, stability bounds are non-zero inequality bounds. The stability parameters should be within a certain stability margin. When a stability parameter is zero, the aircraft is considered neutrally stable for that parameter.

Static stability concerns the initial reaction to an instantaneous perturbation of a motion variable when flying in a steady flight condition. The aircraft should develop forces and moments that counteract the perturbation without pilot assistance in order to be considered statically stable [24].

In order for an aircraft to be considered longitudinally statically stable, it needs to meet two conditions. First of all, the pitching moment needs to decrease with an increase in angle of attack. This guarantees that when there is a sudden increase in angle of attack, the aircraft will pitch nose down, decreasing the angle of attack again. This translates to the requirement for the pitching moment curve to have a negative slope, or $c_{M_\alpha} < 0$ [24].

According to Torenbeek [28], there is an additional requirement to obtain longitudinal static stability.

The static margin should be within a specific range: $0.05 < \text{S.M.} < 0.1$. Lower values for the static margin could result in an aircraft that is unstable, while higher values correspond to aircraft that might be too stable. When an aircraft is too stable, it is at risk of not being maneuverable enough. The static margin can be calculated from Equation 3.11. Here, x_{NP} is the x-coordinate of the neutral point, $x_{CG,aft}$ the x-coordinate of the center of gravity most aft, and MAC the mean aerodynamic chord.

$$\text{S.M.} = \frac{x_{NP} - x_{CG,aft}}{\text{MAC}} \tag{3.11}$$

When it comes to lateral static stability, there is only one condition. When the aircraft is in a freestream flow where the sideslip angle is nonzero, the aircraft should roll into the freestream direction. In other words, when there is a sudden increase in sideslip angle, the roll angle should decrease. This can be translated into a requirement on the rolling moment curve as a function of the sideslip angle: $c_{L_\beta} < 0$. There is a similar requirement for directional stability. When the aircraft flies at a non-zero sideslip angle, the aircraft should yaw into the direction of the sideslip. This means that the slope of the yawing moment curve as a function of the sideslip angle should be positive, or $c_{N_\beta} > 0$ [24].

Dynamic stability concerns the reaction of an aircraft after a disturbance in the trim conditions to go back to the steady trim conditions without any inputs from the pilot. Dynamic stability does take the history of the motion into account and focuses more on the rate at which the motion dampens out. Aircraft generally need to have dynamic stability, although some minor deficiencies can be allowed under certain circumstances [24].

Longitudinal dynamic stability requires certain values for c_{M_q} as well as sufficient damping for both the short-period and phugoid modes. The most important requirement for longitudinal dynamic stability is based on the value for c_{M_q}. c_{M_q} is the rate of change of the pitching moment coefficient as a function of the pitch rate. Note that q is not the same as $\dot{\alpha}$. The pitch angle θ is the sum of the flight path angle γ and the angle of attack α. As a result, the pitch angle can vary at different rates as the angle of attack. To obtain longitudinal dynamic stability, its value should typically be between -30 and -5: $-30 < c_{M_q} < -5$ [24].

The remaining requirements for longitudinal dynamic stability are with respect to the short period natural frequency and damping ratio, and the phugoid damping ratio [4]. The natural frequency of the short period should be between 0.28 and 3.6: $0.28 < \omega_{n,sp} < 3.6$. The damping ratio of the short period should also be within a certain range: $0.3 < \zeta_{sp} < 2$. The natural frequency and damping ratio can be estimated with Equation 3.12 and Equation 3.13 respectively. M_q indicates the rate of change of the dimensional pitching moment as a function of the pitch rate. M_q is the rate of change of the dimensional pitching moment derivative with respect to the vertical velocity component . U_0 is the freestream velocity component in longitudinal direction and I_{yy} is the moment of inertia along the y-axis of the aircraft [29].

$$\omega_{n,sp} = \sqrt{\frac{-U_0 M_w}{I_{yy}}} \tag{3.12}$$

$$\zeta_{sp} = -\frac{M_q}{2}\sqrt{\frac{-1}{U_0 M_w I_{yy}}} \tag{3.13}$$

For the phugoid, there are two different levels that can be applied. Complying with level 1 is satisfactory, but level 2 is also acceptable. To comply with level 1, the damping ratio of the phugoid should be at least 0.04, or $\zeta_p > 0.04$. To reach level 2, the damping ratio should be positive, or $\zeta_p > 0$. The damping ratio of the phugoid can be estimated by Equation 3.14 [30]. The phugoid damping ratio cannot be negative according to Equation 3.14 since L/D is positive by definition. However, it is important to remember that Equation 3.14 is just an approximation and that the phugoid can be unstable in reality. Furthermore, it may seem as if the empennage has no influence on the phugoid damping ratio. However, it is important to note that the empennage efficiency has an influence on the overall lift-to-drag ratio.

$$\zeta_p = \frac{1}{\sqrt{2}L/D} \tag{3.14}$$

There exist three more requirements to achieve lateral-directional stability [4]. First, the rate of change of the yawing moment coefficient as a function of the yaw rate should be negative: $c_{N_r} < 0$. This is similar to the first requirement for longitudinal dynamic stability [31]. Next, the Dutch roll damping ratio needs to be at least 0.08, or $\zeta_{dr} > 0.08$. The Dutch roll damping ratio can be calculated using Equation 3.15 [30].

$$\zeta_{dr} = -\frac{c_{N_r}}{8}\sqrt{2S\rho V b^3 / I_{zz} c_{N_\beta}} \tag{3.15}$$

The final requirement for lateral-directional dynamic stability is the roll mode time constant, which should be less than 1.4: $\tau_{roll} < 1.4$. The roll mode time constant can be found from Equation 3.16 [30]. Note that here, L in c_{L_p} does not denote the lift force, but the rolling moment.

$$\tau_{roll} = \frac{-4I_{xx}}{S\rho V b^2 c_{L_p}} \tag{3.16}$$

Galloway [5] applied optimization for control, stability, and performance on conceptual aircraft design. Galloway developed a design optimization capability that optimized the entire aircraft initial design instead of focusing solely on the empennage. The module was developed in such a way that it is possible to easily change the selection of design variables, constraints, and objective function. Galloway performed test case studies with different objective functions. However, not all the tests are free to explore the full design space. As a result, there is no optimization of the empennage in some tests.

In his second test case, a general aviation aircraft is sized for mission and performance. Constraints are imposed on the static stability and controllability of the aircraft. The objective of the test is to minimize the gross take-off weight, as well as the surface area of the elevator, rudder, and aileron. The design space of the empennage includes the span of both the horizontal and vertical tails and the hinge line location of the elevator and the rudder. Considering only static stability and control constraints, the optimum gross take-off weight is found to be $2715lb$. All the requirements are met. In addition, it is found that increasing the control surface deflection limits reduces the required control surface area. The same test is repeated, but with the addition of dynamic stability and control constraints. Behavior constraints are implemented on the short period, phugoid, Dutch roll, and roll modes of motion to be exact. The design variables and objectives remain the same. However, the additional constraints did not influence the gross take-off weight, since the same value of $2715lb$ is found [5]. These findings indicate that it can be assumed that dynamic stability constraints do not influence the empennage design a lot. Therefore, it has been decided to take only static stability requirements into account.

Control

The third function of the empennage is to offer longitudinal and directional control to the aircraft. One way to measure longitudinal control is the elevator effectiveness. The elevator effectiveness measures the rate of change in the pitching moment as a function of the elevator deflection angle ($c_{M_{\delta_e}}$). Typical values for the elevator effectiveness range between -0.2 and $-4/rad$. The elevator effectiveness can either be measured directly or calculated with Equation 3.17. Here, $c_{L_{\alpha_h}}$ is the horizontal tail lift curve slope, η_h denotes the horizontal tail dynamic pressure ratio (q_h/q_∞), c_{HTP} is the horizontal tail volume coefficient, and b_e and b_{HTP} are the span of the elevator and horizontal tail respectively. τ_e is the angle of attack effectiveness of the elevator; it is mainly a function of the elevator-to-tail chord ratio [24].

$$c_{M_{\delta e}} = \frac{\partial c_M}{\partial \delta_e} = -c_{L_{\alpha_h}} \eta_h \cdot c_{HTP} \cdot \frac{b_e}{b_{HTP}} \tau_e \tag{3.17}$$

Nicolosi et al. [32] researched the directional control effectiveness of aircraft. They found that most aircraft have a rudder effectiveness of approximately 0.004 per degree or 0.23 per radian, or $c_{N_{\delta r}} \approx 0.23/rad$. The rudder effectiveness can be measured directly in a similar way to the elevator effectiveness: $c_{N_{\delta r}} = \frac{\partial c_N}{\partial \delta_r}$

Solver

It is the job of the stability and control discipline to return the stability and control derivatives required for the constraints. The computation of these derivatives requires an aerodynamic solver because empirical methods are deemed not accurate enough for this study. The aerodynamic solver does not need to

be the same as the solver for the aerodynamics discipline. However, using the same solver can have advantages when implementing the disciplines. The stability and control discipline uses the AVL solver just like the low-fidelity version of the aerodynamics discipline.

In addition to the AVL capabilities mentioned in subsection 3.2.2, AVL has some additional capabilities that make it suitable for stability and control analysis. The stability derivatives are direct outputs of AVL, making simulations at different angles of attack and sideslip obsolete. In addition, AVL can simulate control surfaces such as an elevator and rudder, including partial-span and multiple control configurations, while accounting for deflection gains. When such control surfaces are added, the control derivatives are a direct output of the AVL simulations as well. Finally, AVL possesses the ability to analyze dynamic stability when mass properties are provided, making it possible to extend the model in the future. The implementation of the stability and control discipline is presented in section 4.5.

3.2.4. Performance

The goal of the performance discipline is to estimate the fuel load required to cover the mission design range. However, in the case of the APPU propulsion configuration, the aircraft has two separate propulsion systems. Two conventional main engines and a hydrogen-powered propulsor at the back. Traditional methods require adaptations to take into account the thrust delivered by the APPU system.

The Breguet range equation is a simple method to quickly calculate the range of an aircraft based on some basic parameters and fuel load. However, it can also be used to calculate the fuel load required for an aircraft to cover a certain range. The derivation, as given by Kundu [33], is stated below.

The derivation of the Breguet range equation starts from Equation 3.18. It states that the weight of the fuel burned ($\mathrm{d}W$) in an infinitesimal time ($\mathrm{d}t$) is equal to the specific fuel consumption (sfc) times the thrust (T).

$$\frac{\mathrm{d}W}{\mathrm{d}t} = sfc \times T \tag{3.18}$$

Or:

$$\mathrm{d}t = \frac{\mathrm{d}W}{sfc \times T} \tag{3.19}$$

Both the numerator and the denominator can be multiplied by the weight in Equation 3.19. If the aircraft is in equilibrium, as is the case during cruise, $W = L_{des}$ and $T = D_{des}$. This results in Equation 3.20.

$$\mathrm{d}t = \frac{1}{sfc}\left(\frac{W}{T}\right)\left(\frac{\mathrm{d}W}{W}\right) = \frac{1}{sfc}\left(\frac{L_{des}}{D_{des}}\right)\left(\frac{\mathrm{d}W}{W}\right) \tag{3.20}$$

The elemental range can be found from Equation 3.21.

$$\mathrm{d}s = V \times \mathrm{d}t = \frac{V}{sfc}\left(\frac{L_{des}}{D_{des}}\right)\left(\frac{\mathrm{d}W}{W}\right) \tag{3.21}$$

The total range covered during cruise can be found by integrating Equation 3.21 between the final weight after cruise (W_f) and the initial weight before cruise (W_i). In other words, W_i is the weight of the aircraft with fuel on board and W_f without. Changes in L/D and sfc during the cruise phase are often minor. Typically, mid-cruise conditions can be taken such that they can be treated as constants. This results in Equation 3.22.

$$R = \int \mathrm{d}s = \int_{W_f}^{W_i} \frac{V}{sfc}\left(\frac{L_{des}}{D_{des}}\right)\left(\frac{\mathrm{d}W}{W}\right) = \frac{V}{sfc}\left(\frac{L_{des}}{D_{des}}\right)\ln\left(\frac{W_i}{W_f}\right) \tag{3.22}$$

The definition of the lift coefficient can be rewritten so that the velocity V can be expressed as a function of other parameters:

$$V = \sqrt{\frac{2W}{\rho S_{wing} c_{L_{des}}}} \tag{3.23}$$

This can be substituted into Equation 3.22:

$$R = \int_{W_f}^{W_i} \frac{1}{sfc}\sqrt{\frac{2W}{\rho S_{wing} c_{L_{des}}}}\left(\frac{L_{des}}{D_{des}}\right)\left(\frac{\mathrm{d}W}{W}\right) = \sqrt{\frac{2}{\rho S_{wing}}}\int_{W_f}^{W_i}\frac{1}{sfc}\left(\frac{\sqrt{c_{L_{des}}}}{c_{D_{des}}}\right)\left(\frac{\mathrm{d}W}{\sqrt{W}}\right) \tag{3.24}$$

Solving Equation 3.24 results in the final form of the Breguet range equation. It can be seen in Equation 3.25. Note that once again, L/D and sfc can be assumed to be constant during the cruise phase if midcruise values are taken.

$$R = \sqrt{\frac{2c_{L_{des}}}{\rho S_{wing}}}\frac{1}{sfc \times c_{D_{des}}}\int_{W_f}^{W_i}\frac{\mathrm{d}W}{\sqrt{W}} = 2\sqrt{\frac{2c_{L_{des}}}{\rho S_{wing}}}\frac{\sqrt{W_i}-\sqrt{W_f}}{sfc \times c_{D_{des}}} \tag{3.25}$$

3.3. MDO Architecture

One of the most widely applied architectures to MDO problems is the multidisciplinary feasible architecture. The architecture that has been created for this study is an example of it. Before presenting the actual architecture of this study, some theoretical background on multidisciplinary feasible architectures is provided. subsection 3.3.1 is based on the work of Lambe and Martins [34] unless stated otherwise.

3.3.1. Multidisciplinary Feasible

The MultiDisciplinary Feasible (MDF) architecture [35] performs a Gauss-Seidel MultiDisciplinary Analysis (MDA) to guarantee consistency between coupled disciplines. An example Design Structure Matrix (DSM) of the MDF architecture is given in Figure 3.8. Here, x is the design vector consisting of design variables x_i, and y_i is the outcome of analysis i. The numbers in the nodes indicate the order in which the different operations in the boxes are performed.

MDA is a method for solving multiple disciplines in an iterative way in which the most up-to-date coupling variable information is used as an input for the different disciplines. The MDA loop is visualized in Figure 3.8 where it iterates between Steps 2 and 5. When a required input for a discipline has not yet been calculated within the MDA loop, a target value for that input is used (y_i^t). The MDA loop continues to iterate until the target values are equal to the output values, or $y_i^t = y_i$. The outcome of the discipline can be used as the target value for the next iteration of the MDA loop. Once the MDA loop has converged, the objective and constraints are evaluated. The optimizer will then determine the next values for the design variables, and the whole process will be repeated. It is also possible to apply other MDA strategies, such as the Newton MDA strategy, instead of using the Gauss-Seidel MDA strategy.

MDF is essentially the same as single-discipline optimization, where the MDA loop replaces the single discipline. The advantage of MDF is that there is no need for consistency constraints, which reduces the size of the problem. Consistency constraints are used by other architectures that do not make use of an MDA loop, such as Individual Discipline Feasible (IDF), to guarantee consistency between different disciplines. In essence, this means that target values are added to the design vector and used as input to the disciplines. This in turn increases the design space and thus the problem size. Equality constraints are added to the problem that state that the target values should be equal to the output of the discipline they are supposed to originate from. These constraints are known as consistency constraints. The trade-off that is made when applying an MDF architecture is a smaller problem size at the cost of having to set up and run an MDA loop. Additionally, MDF tends to be more robust since there are fewer constraints that need to converge.

3.3.2. Project Architecture

An MDF architecture is designed for this study. An MDF architecture has been selected over an IDF architecture or hybrid between the two primarily for its robustness. Two separate, but similar, architectures have been made. This is because there is an aerodynamic discipline that uses FlightStream and another one that uses AVL, which combines the stability & control discipline. The architecture with the FlightStream-based aerodynamic discipline is visible in Figure 3.9, while the architecture with the

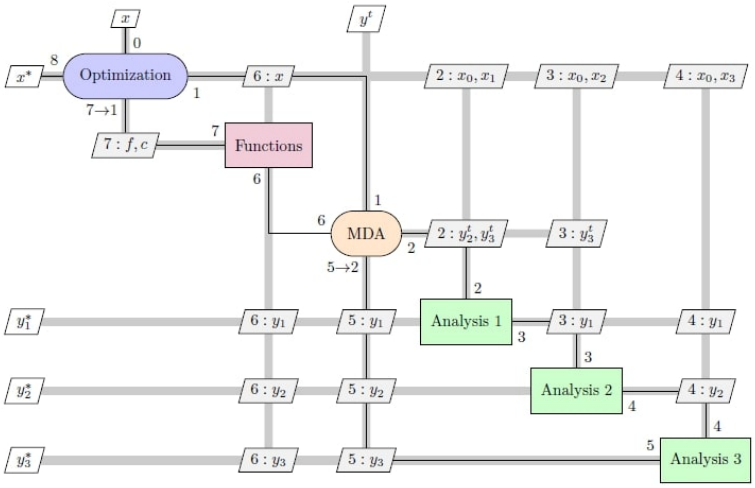

Figure 3.8: Multidisciplinary feasible architecture [34].

AVL-based aerodynamic discipline is portrayed in Figure 3.10. An MDA loop is set up in both architectures where, initially, a target value for the fuel weight is provided to the weight and stability & control disciplines in the FlightStream architecture. For the AVL architecture, the target value is provided to the weight and aerodynamics disciplines. After completing an iteration of the MDA loop, the target value for the fuel weight is replaced with the latest output of the performance discipline.

Five main elements of the architecture are visible on the diagonal from top left to bottom right in the DSM: the optimizer in yellow, the MDA loop in dark gray, the disciplines in blue, the objective in purple, and the constraints in red. The light gray blocks contain the design variables passed on to different elements of the architecture, and the green blocks represent the output of the different disciplines, the objective, and the constraints.

The inputs required for all the different main elements of the architecture can be found on the same vertical line as the main element itself. The outputs of each of the main elements, on the other hand, are located on the same horizontal line as the main elements' blocks. The gray lines between all the blocks represent how all the variables and outputs are communicated between all the elements on the main diagonal. The lack of inputs under the elements on the main diagonal in Figure 3.9 and 3.10 indicates that there are no feedback interactions present in the architecture. This means that there are no fully coupled disciplines present in the architecture. However, there is still directional coupling present in the form of feedforward indicated by the disciplinary outputs that serve as inputs for other disciplines. These outputs are all located above the diagonal, indicating that the coupling is feedforward.

The black arrows indicate the flow of the process. It starts at the initial values of the design variables. These are indicated by 0 in superscript. They are the inputs of the optimizer. From the optimizer, the arrows head to the MDA loop. Within the MDA, all the disciplines are analyzed sequentially. This is repeated until convergence of the fuel weight has been reached. Next in line are the objective and constraint evaluations. They provide their outcomes to the optimizer, which uses them to decide which step to take next or whether the optimization has converged. Once the optimization has converged, the optimizer returns the final value for the design variables, which are left from the optimizer block in the DSM. The final values of the disciplines are also visible on the left-hand side of the DSM. All final values are denoted by an * in superscript. The order of the process is also denoted by the numbers in the blocks on the main diagonal. Processes with the same number can be performed in parallel in theory because they are uncoupled. Note that for the architecture with the FlightStream aerodynamic discipline, two sets of two disciplines can be performed in parallel since they are fully uncoupled. However, this is not done in practice for this study.

Note that the architecture with the FlightStream aerodynamic discipline has an additional design vari-

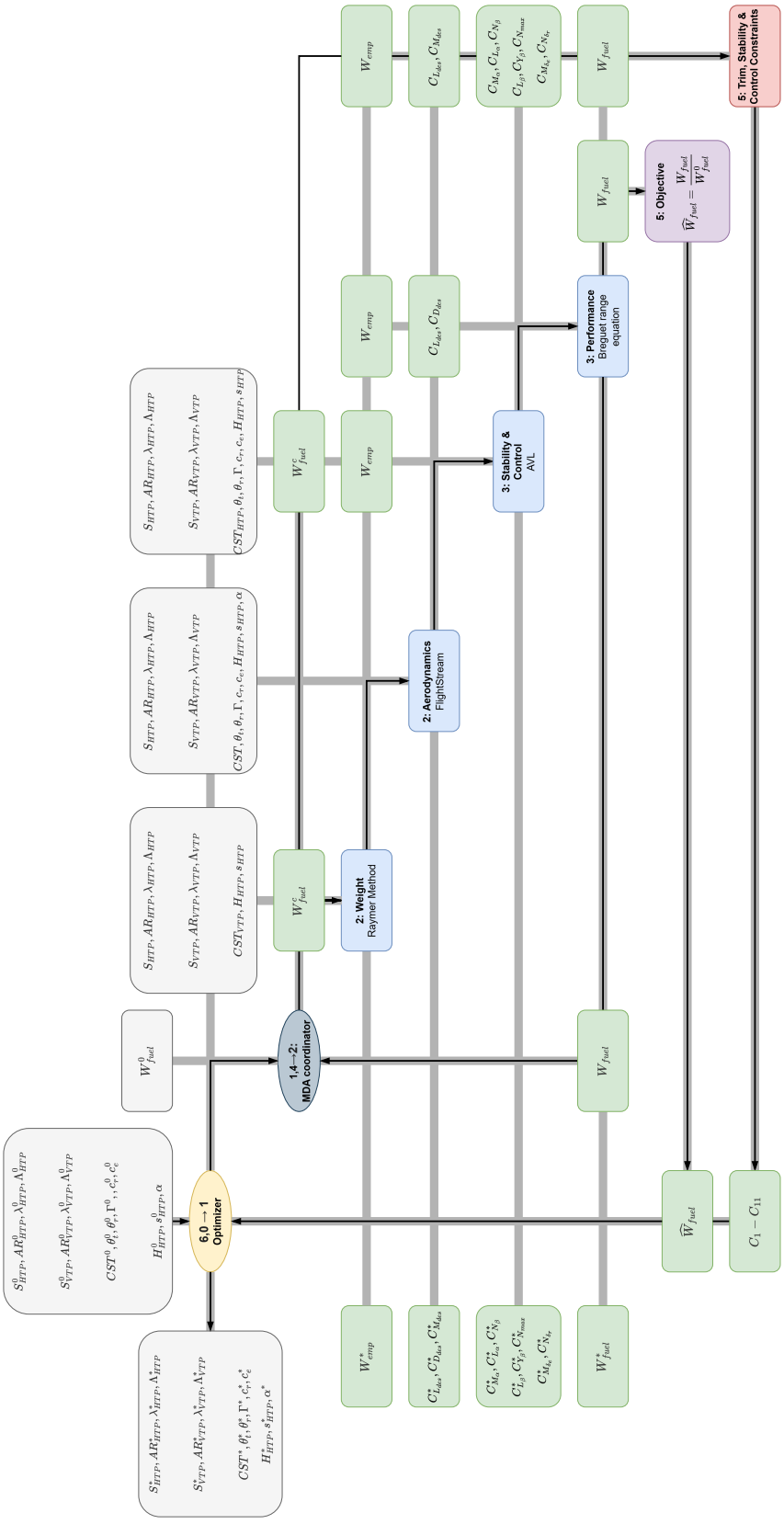

Figure 3.9: Design structure matrix of the MDO architecture for this study with the FlightStream aerodynamics discipline.

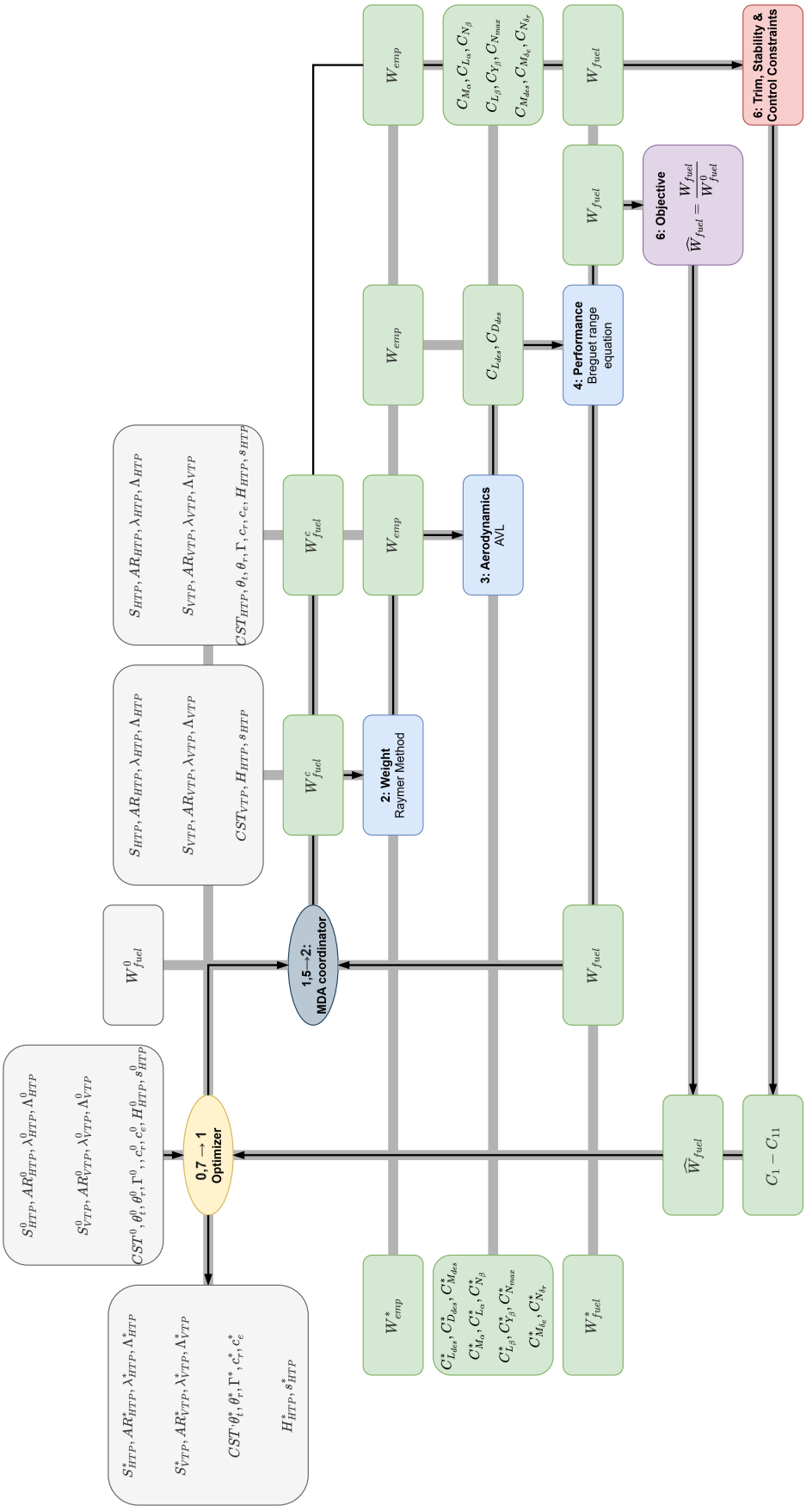

Figure 3.10: Design structure matrix of the MDO architecture for this study with the AVL aerodynamics discipline.

able compared to the architecture with the AVL aerodynamic discipline: α, which is the angle of attack. The aerodynamic discipline uses FlightStream to calculate the lift, drag, and moment coefficients at the design point. However, FlightStream does not have the option to calculate the required angle of attack based on a target lift coefficient. FlightStream instead calculates the lift, drag, and moment coefficient based on the angle of attack it receives from the optimizer. Constraint C_7 guarantees that the lift produced is equal to the aircraft weight at the design point. Note that it is absent in the other architecture since AVL allows users to set a target lift coefficient. More information on the design variables and constraints is provided in section 4.1 and 4.8, respectively.

3.4. Optimization Algorithm

The optimization algorithm chosen for this study is the Sequential Least Square Quadratic Programming (SLSQP) algorithm. The SLSQP algorithm has been described by Kraft [36]. It is one of the most popular algorithms to solve non-linear constrained optimization problems. SLSQP is a gradient-based algorithm that gradually searches for an optimal solution by decomposing the non-linear optimization problem into multiple Quadratic Programming (QP) subproblems. The problems to which SLSQP can be applied can be formulated as follows [36]:

$$\begin{aligned} \min_{x \in \mathbb{R}^n} \quad & f(x) \\ \\ \text{subject to:} \quad & h_i(x) = 0 \quad \text{for} \quad i = 1, \ldots, m, \\ & g_j(x) \geq 0 \quad \text{for} \quad j = 1, \ldots, q, \\ & x_l \leq x \leq x_u \end{aligned} \tag{3.26}$$

The SLSQP algorithm can be broken down into seven steps. Each of these steps is explained below. These steps are also visualized in a flowchart in Figure 3.11.

Step 1: An initial solution x_0 needs to be provided to the algorithm from where it starts looking for an optimum. In addition to this starting point, a set of termination criteria needs to be given. These termination criteria include the maximum number of iterations k_{max}, the tolerance threshold for the change in the objective value ϵ, and a minimum gradient norm τ [37].

Step 2: The value of the objective function $f(x_k)$ and its gradient with respect to the design variables $\nabla f(x_k)$ are calculated at each iteration throughout the optimization process for the current solution denoted by x_k. At the same time, the equality constraint functions $h_i(x_k)$ and inequality constraint functions $g_j(x_k)$ are evaluated at each iteration, as well as their gradients $\nabla h_i(x_k)$ and $\nabla g_j(x_k)$, respectively [37].

Step 3: A quadratic programming subproblem is set up in order to find the search direction of the next step towards the optimal solution. The objective and constraints for this QP subproblem can be seen in Equation 3.27, where p_k is the direction vector, and H_k is the Hessian matrix of the objective function. A quadratic approximation of the problem's Lagrange function is used to compose the subproblem [36]. This method for the search direction was first proposed by Wilson in 1963 [38]. Kraft [36] describes three methods to solve these QP subproblems: a primal method, a primal/dual method, and a dual quadratic programming method.

$$\begin{aligned} \min_{p_k \in \mathbb{R}^n} \quad & \nabla f(x_k)^\intercal p_k + \frac{1}{2} p_k^\intercal H_k p_k \\ \\ \text{subject to:} \quad & \nabla h_i(x_k)^\intercal p_k + h_i(x_k) = 0 \quad \text{for} \quad i = 1, \ldots, m, \\ & \nabla g_j(x_k)^\intercal p_k + g_j(x_k) \geq 0 \quad \text{for} \quad j = 1, \ldots, q, \end{aligned} \tag{3.27}$$

Step 4: Now that the direction of the next step has been determined, the distance that the optimizer moves in this direction must be determined. The step length α_k is found by performing a line search [36]. A trade-off is made in the selection of α_k between a significant reduction in the objective function f and the computational cost of the step length. Ideally, a global minimum is found for the univariate function

shown in Equation 3.28. However, searching for the global minimum or even a local minimum might be too expensive, as it typically requires too many objective function and gradient evaluations. Inexact line searches are more common. Conventional line search algorithms explore a series of potential values for α_k until certain conditions are met. Two popular sets of conditions include the Wolfe conditions and the Goldstein conditions. The line search is carried out in two steps. First, a bracketing phase identifies an interval with suitable step lengths. Then, a good step length within this interval is found by interpolation [39].

$$\min_{\alpha_k \in \mathbb{R}^+} \quad \phi(\alpha_k) = f\left(x_k + \alpha_k p_k\right) \tag{3.28}$$

Step 5: The current solution is updated to find the solution for the next iteration x_{k+1}. To find the next solution, the step size is multiplied by the search direction vector and added to the current solution, as shown in Equation 3.29 [37].

$$x_{k+1} = x_k + \alpha_k p_k \tag{3.29}$$

Step 6: The new solution is checked for convergence. Typically, two convergence criteria are evaluated: the change in objective function value and the gradient norm. The change in objective function value and gradient norm are found from Equation 3.30 and 3.31, respectively. In addition, it is checked whether the maximum number of iterations has been reached [37].

$$|f(x_{k+1}) - f(x_k)| < \epsilon \tag{3.30}$$

$$\|\nabla f(k_{k+1})\| < \tau \tag{3.31}$$

Step 7: If either the change in objective function value or the gradient norm drops below their respective tolerances set in step one, the iterative process is finalized and the latest solution x_{k+1} is returned as the optimal solution for the optimization problem [37]. The latest solution is also returned in case the maximum number of iterations k_{max} has been reached. However, the solution cannot be considered to be the optimal solution since neither the change in objective function value nor the gradient norm is less than the tolerance.

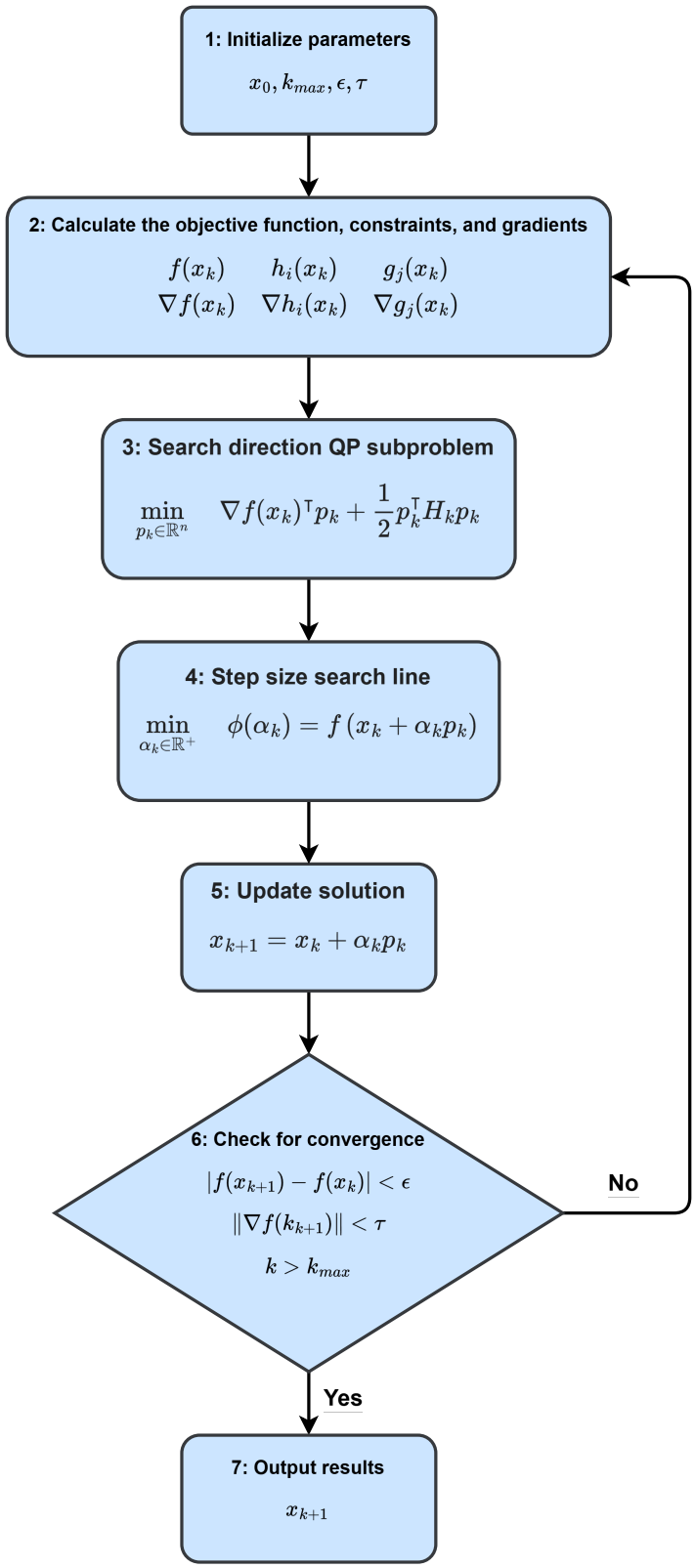

Figure 3.11: SLSQP optimization algorithm flowchart

4

Method Implementation

The methodology in general is explained in chapter 3. This chapter aims to provide a deeper insight into the implementations of some parts of the method described in chapter 3. First, a parameterization is introduced that fully constrains the empennage design based on a set of design variables in section 4.1. The geometry generation based on these design variables is explained in section 4.2. The implementation of the weight, aerodynamics, stability and control, and performance disciplines is presented in section 4.3 to 4.7. Next, the set of constraints that guarantees that the empennage performs its three functions is given in section 4.8. Finally, the initial design of the optimization study can have a large influence on the final design. The way in which the initial design for this study is obtained is explained in section 4.9 together with the lower and upper bounds for the design vector. Some parameters are used throughout the implementation and remain constant during the optimization process. This study was initiated using preliminary project estimates for these parameters, which were kept fixed throughout for consistency. Their values can be found in Appendix A.

4.1. Parameterization

A good parameterization method has four characteristics: it should be consistent, efficient, flexible, and robust. Consistency means that all the disciplinary models are coherent representations of the same model. Efficiency is about reducing the number of design variables as much as possible while still offering freedom over the whole design space. Flexibility is the capacity to produce a wide variety of models from the set of design parameters. The final characteristic is robustness. In order for a parameterization method to be robust, its design variables must produce only physically feasible and usable system variants. This section presents how the empennage for the APPU aircraft is parameterized.

4.1.1. Planform

The HTP and VTP planforms must be parameterized for the optimizer to be able to vary the span, chord lengths, sweep angles, and some other parameters. The parameterization of the planform is based on Liu and Jiang [4], which used a set of design variables that satisfy these requirements. Their set of design variables relating to the planform of the HTP and VTP is listed below:

- Surface area of HTP
- Aspect ratio of HTP
- Taper ratio of HTP
- Leading edge sweep of HTP
- Surface area of VTP
- Aspect ratio of VTP
- Taper ratio of VTP
- Leading edge sweep of VTP

This method is efficient because there are at least four variables required to fully constrain a trapezoid. Both the HTP and VTP are constrained by four variables. By setting the right bounds, this method can

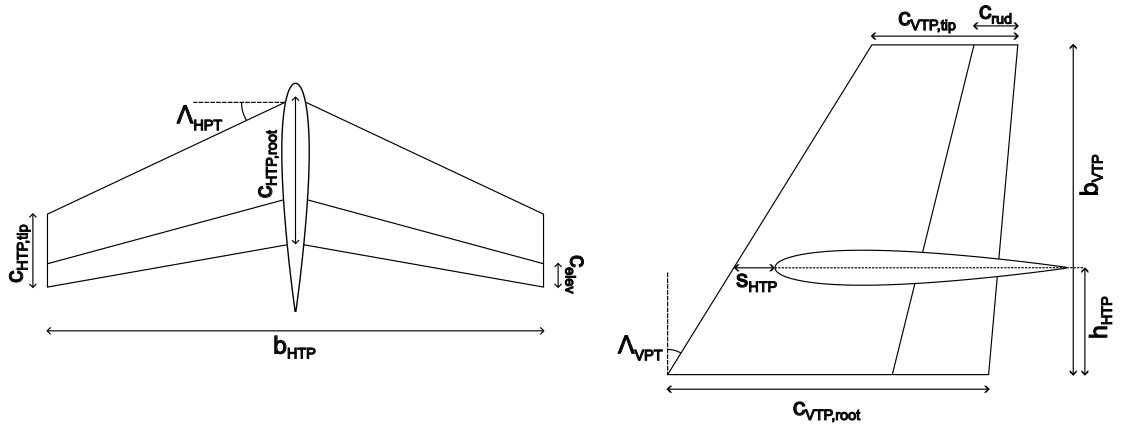

(a) Parameters of the horizontal tailplane.

(b) Parameters of the vertical tailplane.

Figure 4.1: Planform parameters.

be very flexible since a wide range of trapezoid shapes can be generated. Finally, this method is robust when realistic bounds are set. For example, wings with a longer chord at the tip than at the root can be avoided by keeping the aspect ratio below 1. Extremely slender wings can be avoided by putting a realistic upper bound on the aspect ratio.

Figure 4.1 shows some chord lengths, spans, and angles that typically define the planform of a cruciform empennage. Λ_{HTP} and Λ_{VTP} are the leading edge sweep angles of the horizontal and vertical tailplane, respectively. These variables are directly controlled by the parameterization technique of Liu and Jiang [4]. b_{HTP} and b_{VTP} are the spans of the horizontal and vertical tailplane, respectively. The spans of the tailplanes are calculated from the planform parameterization with Equation 4.1. Here AR and S are the aspect ratio and surface area of the relevant tailplane, respectively.

$$b = \sqrt{AR \cdot S} \tag{4.1}$$

$c_{HTP,root}$, $c_{HTP,tip}$, $c_{VTP,root}$, and $c_{VTP,tip}$ are the chord lengths at the root and the tip of the horizontal and vertical tailplane. These chord lengths are calculated based on the aforementioned design variables and spans with Equation 4.2 and Equation 4.3 for the root chords and tip chords, respectively. λ is the taper ratio of the relevant tailplane.

$$c_{root} = \frac{2S}{(1+\lambda)\, b} \tag{4.2}$$

$$c_{tip} = \lambda c_{root} \tag{4.3}$$

Two additional design variables are selected to determine the size of the control surfaces. These are c_{elev} and c_{rud} in Figure 4.1a and Figure 4.1b, respectively. c_{elev} determines the fraction of the local chord of the HTP that is included in the elevator. Similarly, c_{rud} is the fraction of the local chord of the VTP that is included in the rudder. Note that c_{elev} and c_{rud} are fractions of the local chord and not absolute distances. In other words, a value of 0 means there is no control surface, while a value of 1 corresponds with an all-moving tailplane. The location of the hinge line can be found by subtracting c_{elev} or c_{rud} from 1. For instance, when c_{elev} is 0.3, the hinge line is at 70% of the HTP chord.

For a cruciform tail, two more variables are required to determine the location of the horizontal tailplane with respect to the vertical tailplane. This is done with the HTP set-back, s_{HTP}, and HTP height, H_{HTP} as is illustrated in Figure 4.1. H_{HTP} is the relative height of the HTP root leading edge. It is relative to the span of the VTP, meaning that 0 corresponds to a conventional tail and 1 to a T-tail. s_{HTP} is the relative set-back of the HTP root leading edge from the VTP leading edge at the height of the HTP. It is relative to the local chord of the VTP at the height of the HTP. When it is zero, the HTP root leading

edge coincides with the VTP leading edge. A value of one would correspond to the HTP root leading edge being mounted at the VTP trailing edge, which of course is unrealistic.

There are three more variables required to fully determine the shape of the empennage (except for the airfoils). The twist distribution of the HTP is controlled by the root twist angle and the tip twist angle. Between the HTP root and tip, there is a linear twist distribution. The third variable is the HTP dihedral angle, which is set to be constant along the entire span of the HTP. In total, 15 design variables are used to fully constrain the planform of the empennage.

4.1.2. Airfoils

There exist many techniques that can be used to parameterize airfoils. This subsection aims to discuss some of the most popular techniques. It appears that some techniques are superior to others when it comes to convergence rate, complexity of the airfoils that can be represented, etc. Parameterization techniques must fulfill three objectives [40]:

- The number of degrees of freedom should be kept to a minimum.
- A wide range of airfoil shapes should be able to be represented.
- The parameters need to be easy to define and impose.

The efficiency and flexibility that were previously covered can be linked to the first two objectives, respectively. The third requirement has not been discussed before. It is specifically applicable for airfoil parameterization since it can easily get rather complex.

Class-Shape Transformation

The Class-Shape Transformation (CST) is used to parameterize the airfoils of the empennage. Kulfan [41] describes a practical approach to geometry parameterization with CST. Its key benefit is the ability to describe a wide range of geometric shapes using only a few variables. This makes it very suitable for optimization. The two-dimensional form is the one that is applicable for airfoil parameterization. It is given by Equation 4.4. Here ζ and ψ are the normalized coordinates: $\zeta = \frac{z}{c}$ and $\psi = \frac{x}{c}$. $C_{N_2}^{N_1}(\psi)$ is the class function and is determined by two variables: N_1 and N_2. It can be calculated from Equation 4.5. $S(\psi)$ is the shape function and Z_{TE} is the trailing edge thickness. It can be set equal to zero in order to obtain a sharp trailing edge.

$$\zeta(\psi) = C_{N_2}^{N_1}(\psi) \cdot S(\psi) + \psi \cdot Z_{TE} \tag{4.4}$$

$$C_{N_2}^{N_1}(\psi) = \psi^{N_1} (1-\psi)^{N_2} \tag{4.5}$$

Transport aircraft have airfoils with a rounded leading edge and a sharp trailing edge. This general shape can be obtained from the class function by setting $N_1 = 0.5$ and $N_2 = 1$. Bernstein basis polynomials are used for the shape function. The shape function is determined by Equation 4.6.

$$S(\psi) = \sum_{i=0}^{n} B_i^n(\psi) A_i \tag{4.6}$$

Here, B_i^n is the Bernstein basis polynomial. They are multiplied by a weight A_i that is known as the CST coefficient. The values of A_i are gathered in two vectors of length $n+1$. One for the upper surface and one for the lower surface of the airfoil, $\mathbf{A_u}$ and $\mathbf{A_l}$ respectively. It is these weights that determine the shape of the airfoil. The function for the Bernstein basis polynomials can be seen in Equation 4.7. Here, $\binom{n}{i}$ is the binomial coefficient. It can be calculated from Equation 4.8.

$$B_i^n = \binom{n}{i} \psi^i (1-\psi)^{n-i} \tag{4.7}$$

$$\binom{n}{i} = \frac{n!}{i!\,(n-i)!} \tag{4.8}$$

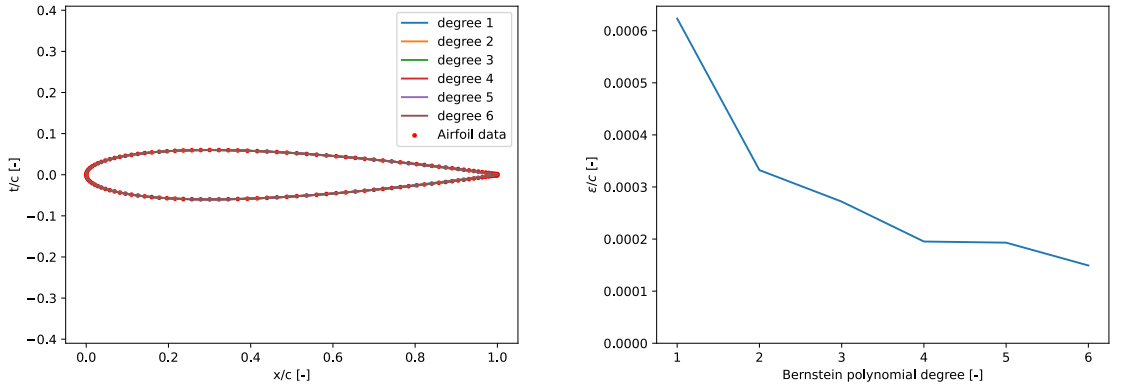

(a) Fit of the CST-generated airfoil.

(b) Error convergence with increasing shape function order.

Figure 4.2: Convergence study on the NACA0012 symmetric airfoil.

Shape Function Order

The number of design variables per airfoil depends on the order of the shape function. A shape function of the n^{th} degree requires $n+1$ design variables for symmetric airfoils and $2n+2$ for asymmetric airfoils. The goal is to keep the number of design variables to a minimum by keeping the order low while offering enough flexibility for the airfoil shape. In pursuit of investigating the optimum order of the shape function, a convergence study has been performed.

The optimum order of the shape function is found by using an optimization algorithm to minimize the error between the generated airfoil and the coordinates of a known airfoil that is modeled by the generated airfoil. The error is measured as the average vertical distance between the generated airfoil and the modeled airfoil at every x-coordinate of the modeled airfoil for both the upper and the lower surface. The objective function for the convergence study is shown in Equation 4.9. Here ϵ/c is the error that is minimized. N_{up} and N_{lo} are the number of coordinates of the modeled airfoil's upper and lower surface respectively. $\zeta_{i,up}$ and $\zeta_{i,lo}$ are the normalized z-coordinate at the i^{th} normalized x-coordinate of the modeled airfoil's upper and lower surface, respectively. $\zeta_{i,up_{CST}}$ and $\zeta_{i,lo_{CST}}$ are the normalized z-coordinate value at the i^{th} normalized x-coordinate of the generated airfoil's upper and lower surface respectively.

$$\epsilon/c = \frac{\sum_{i=1}^{N_{up}} |\zeta_{i,up} - \zeta_{i,up_{CST}}| + \sum_{i=1}^{N_{lo}} |\zeta_{i,lo} - \zeta_{i,lo_{CST}}|}{N_{up} + N_{lo}} \tag{4.9}$$

The convergence study has been performed for shape functions of the 1st order to the 6th order for three different types of airfoils. The first airfoil is a symmetric airfoil, the second is an airfoil with some camber, and the final airfoil is a transonic airfoil. The results for the symmetric NACA0012 airfoil are visible in Figure 4.2. The fit of the CST-generated airfoils with the data points for the NACA0012 can be seen in Figure 4.2a. The red dots represent the coordinates of the actual NACA0012 airfoil. The solid lines are the CST-generated airfoils. It is clear that, visually, even the 1st order shape function is able to get a good fit for a standard symmetric airfoil since they all nicely overlap with the data points. Figure 4.2b shows the convergence of the error with increasing order of the shape function. The error increases significantly with increasing order up to the 4th order shape function. For even higher order shape functions, the marginal decrease in the error is limited. However, later in this section, it will become clear that the error for the first order shape function is already relatively small compared to the error for the transonic airfoil.

The results of the convergence study on the cambered NACA2412 airfoil can be seen in Figure 4.3. In general, the same trends can be seen as with the symmetric NACA0012 airfoil. The fit of the CST-generated airfoils with the data points for the NACA2412 is visible in Figure 4.3a. Again, the red dots represent the coordinates of the actual NACA2412 airfoil and the solid lines are the CST-generated airfoils. Visually, all the CST-generated airfoils seem to nicely fit the data points. Just like it was the

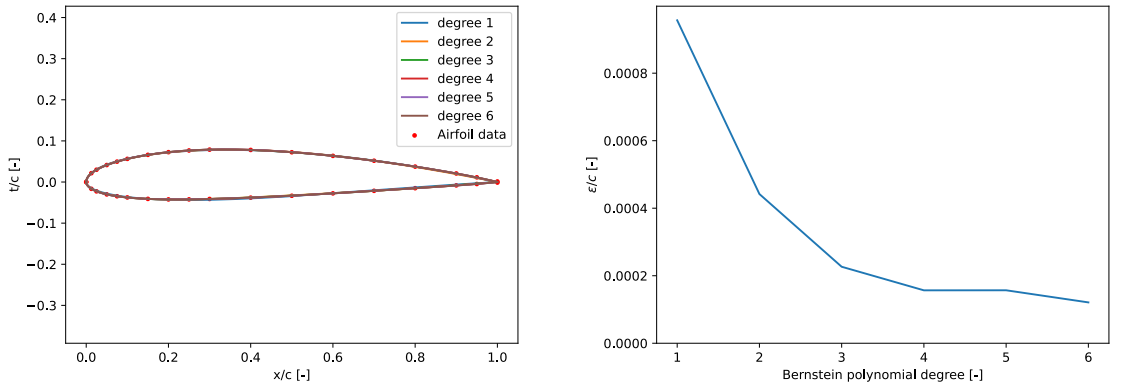

(a) Fit of the CST generated airfoil.

(b) Error convergence with increasing shape function order.

Figure 4.3: Convergence study on the NACA2412 cambered airfoil.

case for the symmetric airfoil. The error convergence with increasing shape function order is given in Figure 4.3b. The same general profile is visible as for the NACA0012 airfoil, where the error is already relatively small to begin with for the first-order shape function. The decrease in the error with increasing shape function order is significant up to the 4th order. For higher orders, the marginal benefit is limited. Just like the symmetric airfoil.

The final convergence study is performed on the Withcomb135 transonic airfoil. The results are given in Figure 4.4. The fit of the CST-generated airfoils with the Withcomb135 data points is shown in Figure 4.4a. Again, the red dots represent the coordinates of the actual Withcomb135 airfoil, and the solid lines are the CST-generated airfoils. This time, there are some clear visual differences between the lower-order generated airfoils and the data points.

The first order shape function seems to have some trouble fitting the upper surface. The first order upper surface approximation creates an airfoil that is too narrow at the leading and trailing edge, while being too thick near the middle. Higher order approximations fit the upper surface much better.

The fit of Bernstein polynomials is worse on the lower surface compared to the upper surface. The first order polynomial fits the lower surface relatively well near the leading edge, but thins out the airfoil near the middle. The fit is the worst near the trailing edge, where the airfoil becomes so thick that the cavity near the trailing edge disappears. The second order provides a better fit compared to the first order approximation on the lower surface. However, the fit near the leading edge is worse for the second order polynomial compared to the first order polynomial. In the middle of the lower surface, the second order approximation creates an airfoil that is too thick in front of approximately 45% chord and too thin beyond. The cavity near the trailing edge is also reduced in size, but not as drastically as for the first order approximation.

This also becomes evident when looking at the convergence with increasing shape function order in Figure 4.4b. For a first order shape function, the error is a full order of magnitude higher than the error for the first order shape function in the previous two convergence studies on the NACA0012 and NACA2412 airfoils. The error reduces for higher order shape functions. However, the error for the 6th order shape function for the Withcomb135 airfoil is in the same order of magnitude as the 1st order shape function for the NACA0012 and NACA2412 airfoils, which confirms that the error for the 1st order shape function in those cases is indeed already relatively low. For the Withcomb 135 transonic airfoil, the error drastically reduces with increasing shape function order up to the 3rd degree. For higher orders, the error stagnates, and the marginal benefit of the higher order is no longer worth the additional variables.

The Airbus A321neo has been chosen as the baseline for the APPU project. Transonic flow can occur

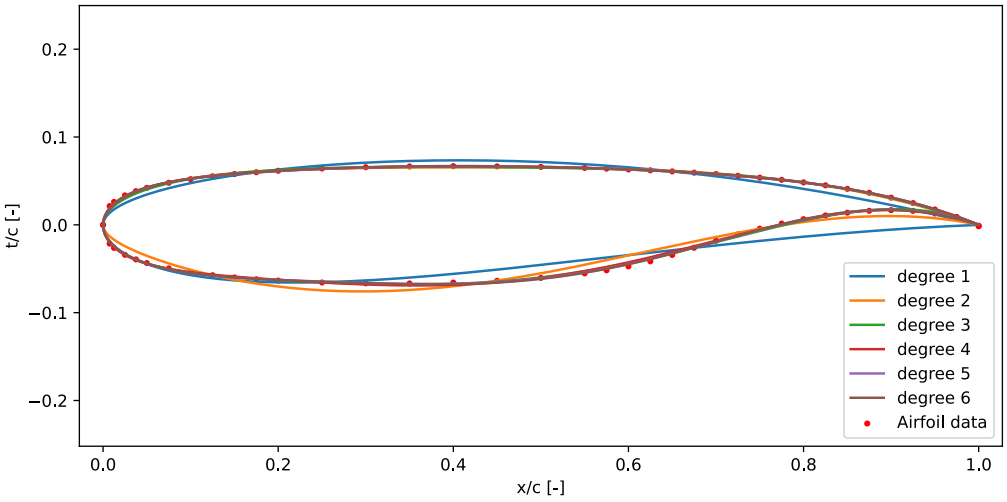

(a) Fit of the CST-generated airfoil.

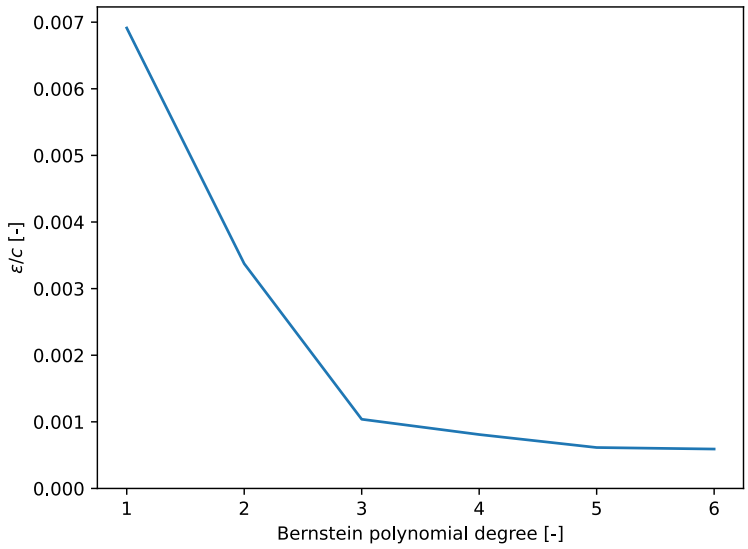

(b) Error convergence with increasing shape function order.

Figure 4.4: Convergence study on the Withcomb135 transonic airfoil.

at the cruise velocity of the A321neo. Therefore, it is of great importance that the parameterization technique is able to properly model transonic airfoils. Based on the final convergence study with the Withcomb135 airfoil, this means that at least a 3rd order shape function is required to model such airfoils. As a result, four design variables are required for the symmetric airfoils of the vertical tailplane and eight design variables for the horizontal tailplane airfoils. With each tailplane consisting of a root and a tip airfoil, a total of 24 design variables for the airfoil optimization is obtained.

4.2. Geometry Generation

In order to be able to use a panel method, many 3D models of the aircraft will need to be generated. The empennage design in these models needs to be based on the parameters given by the optimizer. This cannot be done manually in every iteration of the optimization process. As a result, traditional Computer Aided Design (CAD) tools are ruled out. The optimization algorithm requires a Multi-Model-Generator (MMG) which is a tool that can generate 3D models based on a certain set of parameters. ParaPy is a Python library that is mainly focused on knowledge based engineering. However, it can also be used as an MMG [42].

Figure 4.5 shows a class diagram of all the different classes that make up the geometry of the aircraft. The aircraft is made up of the fuselage, main wing, and empennage. Subclasses are used to generate airfoils and wing segments for the empennage and main wing. This chapter discusses how the geometry of the aircraft is created based on the design variables presented in section 4.1 starting at the airfoil level and building up all the way to the aircraft level.

4.2.1. Airfoil

First, a set of coordinates is generated based on the CST coefficients. In order to achieve this, 50 equispaced points between 0 and 1 are generated. A cosine spreading is used for the normalized x-coordinates to capture as much detail as possible of the airfoil where the curvature is typically the highest for transonic airfoils, i.e. near the leading and trailing edge. This is achieved with Equation 4.10. Here, ψ_{eq} are the equispaced normalized x-coordinates and ψ are the resulting normalized x-coordinates with cosine spreading. The normalized z-coordinate (ζ) of the upper and lower surface at each ψ is calculated based on the CST coefficients with the method explained in subsection 4.1.2. An example of these normalized coordinates for a NACA0012 airfoil can be seen in Figure 4.6. It is clearly visible that there is an increased concentration of points near the leading and trailing edges of the airfoil.

$$\psi = 0.5 \cos(\pi \psi_{eq}) + 1 \tag{4.10}$$

When the control surface is deflected, the coordinates of each point behind the hinge line are adjusted such that they meet the required deflection angle. For each point behind the hinge line, the distance to the hinge line is calculated as $d_{hinge} = \psi - \psi_{hinge}$, where ψ_{hinge} can be easily calculated from the parameterization technique explained in subsection 4.1.1 as $\psi_{hinge} = 1 - c_{hinge}$. Here c_{hinge} is the hinge line fraction. It is the general term for c_{elev} and c_{rud} from section 4.1. The difference in the normalized x-coordinate ($\Delta\psi$) and the difference in the normalized z-coordinate ($\Delta\zeta$) are calculated from Equation 4.11 and 4.12, respectively. Here, δ is the deflection angle. $\Delta\psi$ and $\Delta\zeta$ are added to the applicable original coordinates to find the deflected coordinates. This is visualized in Figure 4.6 where c_{hinge} is set at 0.3 and the deflection angle is set at $\delta = 20°$.

$$\Delta\psi = d_{hinge}(\cos\delta - 1) \tag{4.11}$$

$$\Delta\zeta = -d_{hinge} \sin\delta \tag{4.12}$$

Now that the final coordinates of the points are known, a separate fitted curve is applied to the points for both the upper and lower surface of the airfoil. These fitted curves are then scaled and repositioned such that the chord length can be set and that the origin lines up with the leading edge of the airfoil. The result is an airfoil that consists of an upper and lower surface curve that is entirely determined by the CST coefficients, chord length, hinge line location, and deflection angle.

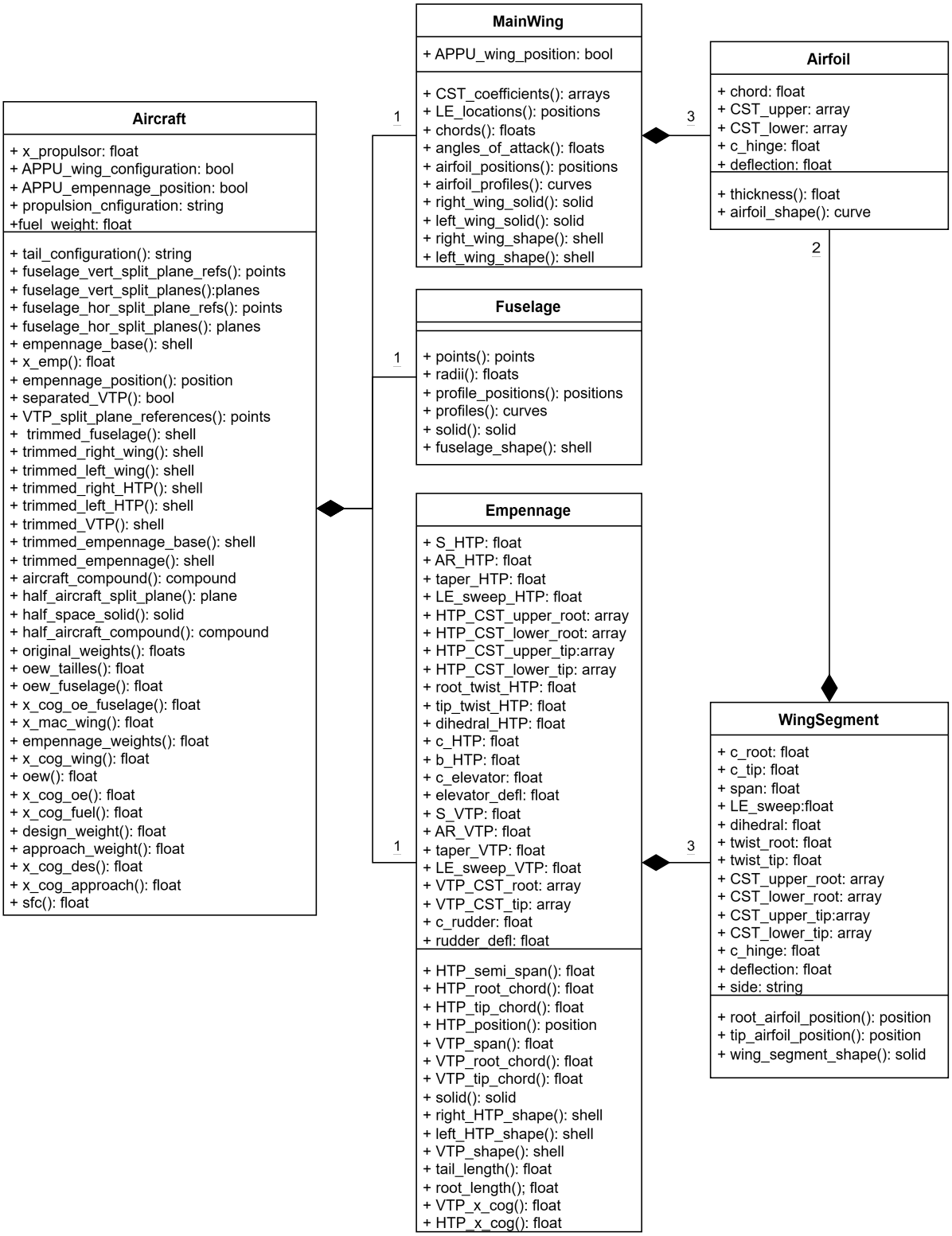

Figure 4.5: Class diagram of the aircraft geometry.

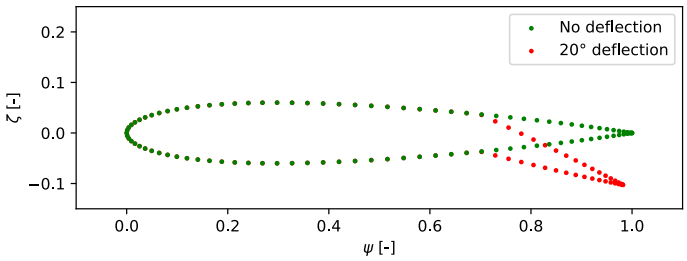

Figure 4.6: Cosine spaced points for fitted upper and lower surface curves of a NACA0012 airfoil with 0° and 20° control surface deflection.

An attribute is added to the airfoil class that returns the airfoil thickness. The airfoil thickness of the VTP root is one of the variables in the Raymer method to estimate the empennage weight described in subsection 3.2.1. Since the maximum thickness of an airfoil is typically closer to the middle of the airfoil, 100 equispaced points are generated between 0 and 1. The z-coordinate of both the upper and lower surface is calculated at each point. The local thickness is the difference between the upper and lower surface z-coordinate at that point. The attribute returns the maximum value of all local thicknesses.

4.2.2. Wing Segment

The airfoils generated in subsection 4.2.1 are used to create wing segments, which, in turn, are used to create an empennage. A wing segment takes a total of 14 inputs to fully constrain the wing segment geometry. These inputs include:

- Root chord length
- Tip chord length
- Span
- Leading edge sweep angle
- dihedral angle
- Root twist angle
- Tip twist angle
- CST coefficients for the root upper surface
- CST coefficients for the root lower surface
- CST coefficients for the tip upper surface
- CST coefficients for the tip lower surface
- Hinge line fraction
- Control surface deflection angle
- Side

These inputs are also visible in Figure 4.5. Two airfoil instances are created: a root airfoil and a tip airfoil. The chord lengths and CST coefficients are passed on to the relevant airfoils. The hinge line fraction and deflection angle are also passed on to both airfoils such that a wing segment is created where the hinge line is at a constant fraction of the chord and the deflection angle is uniform along the span. The root airfoil is rotated such that the incidence angle matches the root twist angle. As a result, the wing segment is positioned such that the origin is at the leading edge of the root airfoil. The tip airfoil is then positioned such that the required span, leading edge sweep angle, dihedral angle, and tip twist angle are obtained. The side input simply determines whether it is a left-sided or right-sided wing by positioning the tip airfoil either to the left or to the right of the root airfoil. A lofted solid is generated between the root and tip airfoil to obtain the wing segment. An example of such a wing segment can be seen in Figure 4.7.

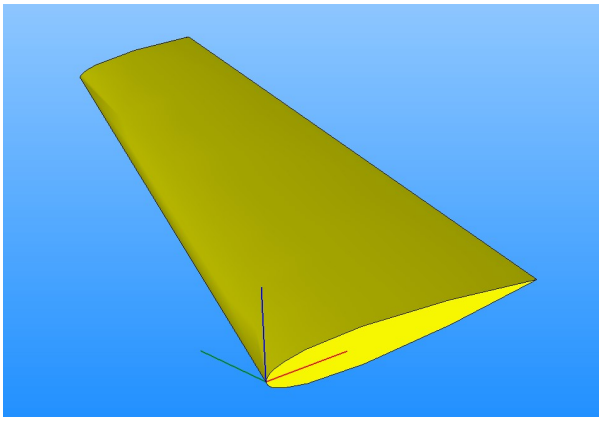

Figure 4.7: Right-sided wing segment.

4.2.3. Empennage

The empennage is made up of three wing segment instances: one for the vertical tailplane and two for the horizontal tailplane (one for each side). The empennage class has 23 inputs that match the design variables presented in section 4.1 with the addition of the deflection angle of the elevator and rudder:

- HTP surface area
- HTP aspect ratio
- HTP taper ratio
- HTP leading edge sweep angle
- HTP CST coefficients for the root upper surface
- HTP CST coefficients for the root lower surface
- HTP CST coefficients for the tip upper surface
- HTP CST coefficients for the tip lower surface
- HTP root twist angle
- HTP tip twist angle
- HTP dihedral angle
- HTP set-back
- HTP height
- Elevator chord fraction
- Elevator deflection
- VTP surface area
- VTP aspect ratio
- VTP taper ratio
- VTP leading edge sweep angle
- VTP CST coefficients for the root
- VTP CST coefficients for the tip
- rudder chord fraction
- rudder deflection

Again, these inputs can also be seen in Figure 4.5. The required spans and chord lengths for the inputs of the wing segments are calculated with Equation 4.1 to 4.3. The empennage is positioned such that the origin is at the leading edge of the root of the VTP. In order to position the HTP, the local chord of the VTP at the height of the HTP is calculated as a linear interpolation between the VTP root and tip chord with Equation 4.13. The local chord length is then used to find the x-coordinate of the HTP root leading edge from Equation 4.14. The z-coordinate of the HTP root leading edge is found from Equation 4.15. An example of such an empennage is visible in Figure 4.8.

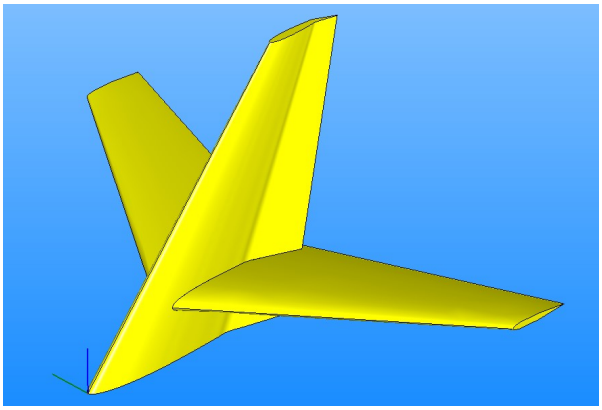

Figure 4.8: Example of an empennage where H_{HTP} and s_{HTP} are both set at 0.2, the rudder is deflected 20°.

$$c_{local} = H_{HTP} c_{VTP,tip} + (1 - H_{HTP})\, c_{VTP,root} \tag{4.13}$$

$$x_{HTP} = H_{HTP} b_{VTP} \tan \Lambda_{VTP} + s_{HTP} c_{local} \tag{4.14}$$

$$z_{HTP} = H_{HTP} b_{VTP} \tag{4.15}$$

Depending on whether an APPU propulsor is present, the position of the empennage is determined by the VTP trailing edge root point, or by the aft-most point of the whole empennage. An attribute, tail length, returns the overall length. This is the distance between the VTP root leading edge x-coordinate and the maximum x-coordinate of the trailing edge of the HTP and VTP root and tip. Whichever is most aft of the four. Another attribute returns the root length. This is essentially the same method as the tail length attribute, but only the root of the HTP and VTP trailing edges are considered.

The center of gravity of the aircraft is required for the aerodynamic moment and stability & control coefficients. The center of gravity and the weight of the empennage vary throughout the optimization, influencing the center of gravity of the aircraft in turn. To adjust the aircraft's center of gravity, the center of gravity is calculated based on the method described by Roskam [43]. The HTP center of gravity is at 42% chord of the leading edge at 38% of the semi-span. The VTP center of gravity depends on the relative height of the HTP. It is also at 42% chord of the leading edge, but varies between 38% and 55% of the VTP span from the root. It should be interpolated between 38% and 55% based on H_{HTP}.

4.2.4. Main Wing

The main wing is based on a CAD model that is imported from a STEP file based on the data from Orlita [44] for the A320 main wing. The main wing is identical for the A320 family, and thus for the A321 and APPU aircraft as well. However, there were two problems with the imported geometry. First of all, the imported wing geometry had a blunt trailing edge. This is visible in Figure 4.9. Blunt trailing edges work well with high order solvers, but lower order solvers such as panel method solvers often have a hard time dealing with them. In addition, some of the edges were created from multiple curves. This brings its own set of problems when trying to generate a mesh for the aerodynamic solver. For these two reasons, it has been decided to recreate the geometry of the wing with some minor adjustments.

The original wing is constructed out of three airfoils, one at the root, one at the kink, and one at the tip. The airfoil curves at each of these locations are found by intersecting the wing with planes at these locations. This is visualized in Figure 4.10.

The upper and lower surfaces of these airfoils are scaled and repositioned such that their chord length is 1 and their leading edge at the origin and trailing edge at $(1, 0, 0)$. Coordinates of the airfoil are created by taking 100 equispaced points along both the upper and lower surfaces. These coordinates are used to find the CST coefficients of a best fit airfoil. This is done with the same method that is explained

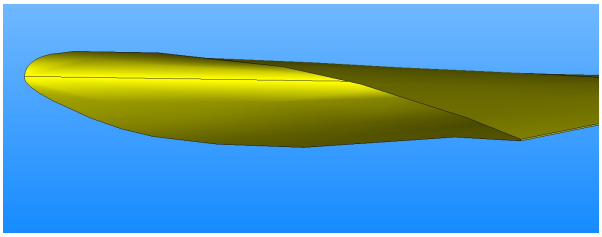

Figure 4.9: Original wing geometry with a blunt trailing edge.

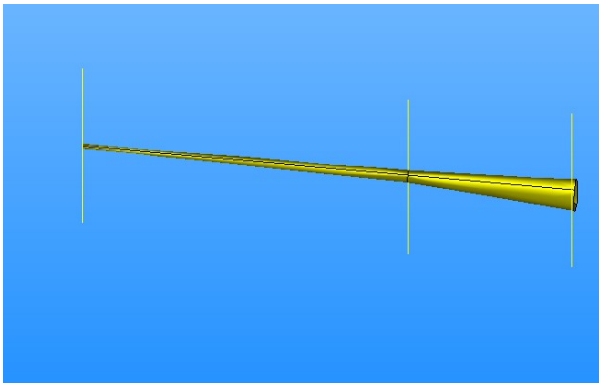

Figure 4.10: Original main wing geometry intersected by planes at the root, kink, and tip.

in subsection 4.1.2. This method does not allow a blunt trailing edge; thus, it will create an airfoil that has the best match with a sharp trailing edge. Since the main wing only needs to be generated once, and the CST coefficients are not part of the design vector, the order can be increased to capture more details of the airfoil. Therefore, the airfoil is generated for different shape function orders. An overlay of the generated root airfoils for a shape function order of 5 to 7 is visible in Figure 4.11a. It is clear that the shape is well matched with a sharp trailing edge by the shape functions of degree 6 and 7. It is also apparent from Figure 4.11b that the error converges for shape function orders larger than 6. For these reasons, it has been decided to use a sixth order shape function to generate the airfoils for the reconstructed main wing.

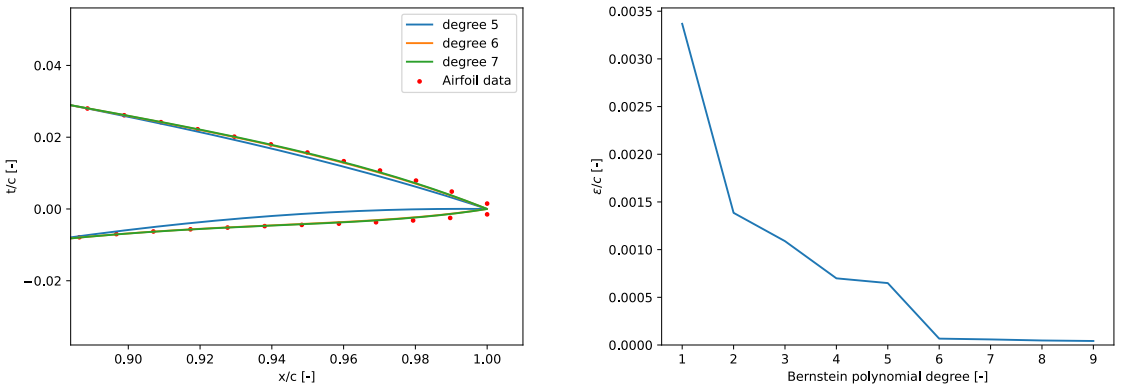

(a) Fit of the CST-generated airfoil at the trailing edge.

(b) Error convergence with increasing shape function order.

Figure 4.11: Convergence study on the main wing root airfoil.

Once the CST coefficients are known, three instances of the airfoil class described in subsection 4.2.1 are created. The chord is set such that it matches the chord lengths of the original airfoils, and they are positioned at the same position as the airfoils found from the intersection. A ruled solid is created

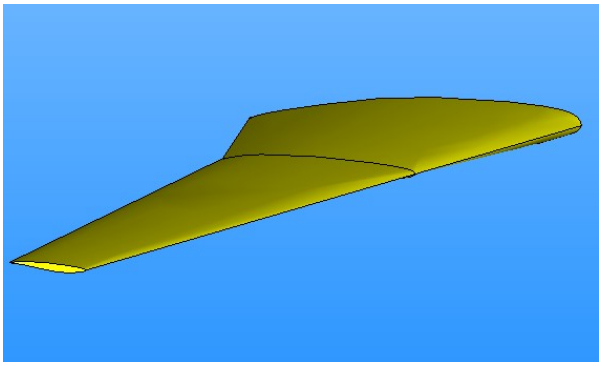

(a) Isometric view of the reconstructed main wing.

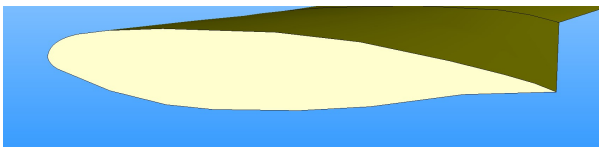

(b) Reconstructed wing root with a sharp trailing edge.

Figure 4.12: Reconstructed main wing.

between the root, kink, and tip airfoil to find the reconstructed geometry of the main wing. An isometric view of the reconstructed main wing can be seen in Figure 4.12a. The root of the reconstructed wing is visible in Figure 4.12b, where it is clear that the blunt trailing edge has been removed. This whole process was done for the right main wing. The left main wing was created by mirroring the right main wing along the xz-plane. An input is created to position the main wing either at the location of the A321neo main wing position or at the APPU aircraft main wing position, which is moved 1.2m aft with respect to the A321neo wing position.

4.2.5. Fuselage

Similarly to the main wing, a CAD model of the fuselage of the APPU aircraft was available from a STEP file. However, upon closer inspection, it appeared that some of the edges of the CAD model consisted of multiple curves. Just as it was the case for the main wing, this resulted in some issues when trying to generate a surface mesh for the aircraft. The imported fuselage geometry can be seen in Figure 4.13.

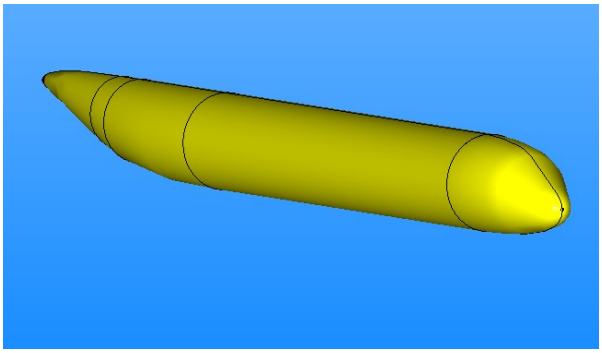

Figure 4.13: Imported APPU aircraft fuselage geometry from STEP file.

To eliminate these edges that consist of multiple curves, the fuselage used in this study has been reconstructed in a similar way as the main wing, using 21 planes distributed according to a cosine function along the fuselage axis. The cosine spreading ensures that the density of planes is higher near the tip and tail of the empennage where there is more curvature in the fuselage outline. The positioning of these planes is visible in Figure 4.14a. The profiles that result from the intersections of the fuselage with the planes are shown in Figure 4.14b. When trying to create a lofted solid from

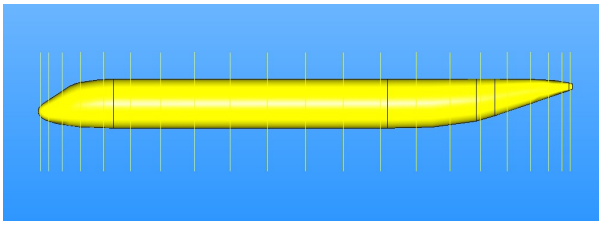

(a) Cosine spreading of the planes that intersect the fuselage.

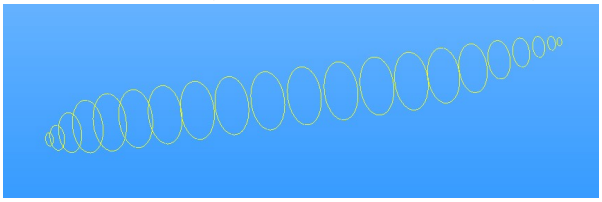

(b) Intersections of the fuselage with the planes.

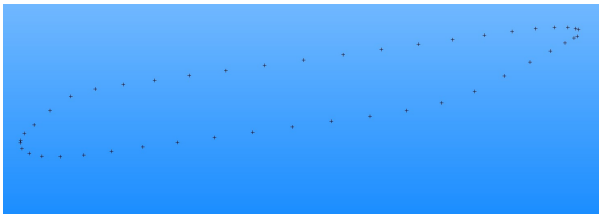

(c) Top and bottom point of the intersections.

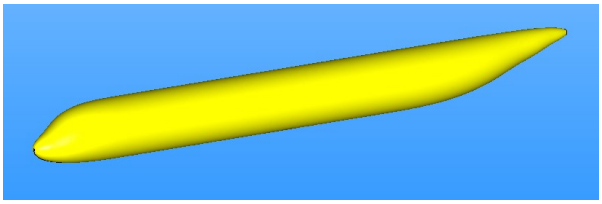

(d) Reconstructed fuselage.

Figure 4.14: Reconstruction of the fuselage.

the profiles, it became apparent that some of the profiles were oriented upside-down compared to the others. To solve this issue, the top and bottom point of each profile was taken as is shown in Figure 4.14c. New profiles that all had the same orientation are created by generating circles through these points. Since these profiles are the same as the profiles in Figure 4.14b, but all with the same orientation, a lofted solid is generated that resembles the fuselage of the APPU aircraft. It has fewer edges than the imported geometry. This can also further facilitate the generation of a mesh. The final result is visible in Figure 4.14d.

4.2.6. Aircraft

The aircraft class integrates all the subclasses from Figure 4.5. This subsection starts off with a description of how the geometries of the subclasses are merged to form the aircraft geometry. Afterwards, some attributes are discussed that are of importance in determining the weight, center of gravity, and specific fuel consumption of the aircraft. These attributes play an important role in the analysis of the disciplines.

Geometry

The outer shells of the solids of the empennage, main wing, and fuselage classes are positioned such that the origin is at the nose of the fuselage. The main wing is already positioned at the location of the A321neo main wing since it takes its position from the CAD file. As mentioned in subsection 4.2.4, the position can easily be changed to the main wing position of the APPU aircraft with an input that is

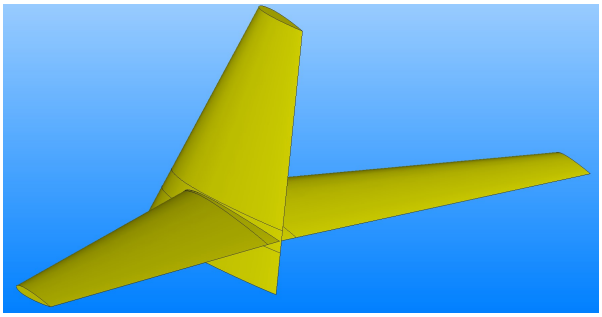

Figure 4.15: Empennage split into quadrilateral faces.

passed on to the main wing class. The positioning of the empennage is controlled with another input and depends on the study case. When the propulsor is present in the case, no part of the empennage should cross the propulsor plane. This is to avoid damage to the empennage in the event of a propulsor failure. When the propulsor is not part of the study case, the empennage is positioned such that there is a small offset between the trailing edge of the root of the VTP and the rear of the fuselage. In case there is a conventional tail, the root trailing edge of the HTP should not be beyond the fuselage tail either. As a result, the position of the VTP leading edge is determined by boolean input, APPU empennage position, and either the tail length, root length, or VTP chord length of the empennage, which have been discussed in subsection 4.2.3.

With the eye on creating a mesh of the aircraft geometry, it is important to have quadrilateral faces cover as much area of the shells as possible. Quadrilateral faces enable the usage of a structured mesh which tends to need fewer cells to capture the same amount of detail as unstructured meshes. For the main wing, no adjustments need to be made to the geometry since both the upper and lower surfaces already consist of quadrilateral faces. Only the airfoil at the tips needs an unstructured grid. For the fuselage, quadrilateral faces are created by splitting the fuselage in longitudinal direction slightly ahead and behind both the main wing and the empennage. The fuselage section at the main wing is split vertically above and below the wing such that a structured mesh can be generated at the top and bottom of the fuselage at this section. The same is done for the bottom of the fuselage section at the empennage. The fuselage divided into quadrilateral faces can be seen in Figure 4.16a.

For the empennage, quadrilateral faces are created for the VTP by splitting the VTP right above and below the HTP. This results in a quadrilateral face at the top and bottom at each side of the VTP. If the configuration is either a conventional tail or a T-tail, the VTP is only split either above or below the HTP, depending on the configuration. Both sides of the HTP are split outward of the widest point of the VTP. This is to ensure that the upper and lower surface faces do not contain five edges in case the left and right side of the HTP touch either in front or behind the VTP. The result is visible in Figure 4.15. This way a structured mesh will be able to be generated for the majority of the surface area of the empennage, leaving only the tips and the area where the VTP and HTP merge with an unstructured grid.

All the shells that make up the aircraft need to be trimmed. For the fuselage, this means that there needs to be a cut-out for the main wing, VTP, and HTP in case the configuration is a conventional tail. For the main wing and empennage, this means that the parts of the shells that are inside of the fuselage are removed. Additionally, there is a cut-out for the HTP in the VTP, and the part of the HTP inside of the VTP is removed in case the HTP and VTP meet. These trimmed shells are obtained by subtracting the relevant solids from the shells. The trimmed shells together form a compound that represents an outer shell of the aircraft geometry that is ready to be meshed. An example of a trimmed fuselage can be seen in Figure 4.16a. A clear cut-out is visible for the main wing, VTP, and HTP. The compound of all the trimmed shells that make up the aircraft geometry is shown in Figure 4.16b.

The mesh is required for the aerodynamics discipline which returns the lift, drag, and pitching moment from FlightStream. An easy way to speed up this process is to create a mesh of only one side of the air-

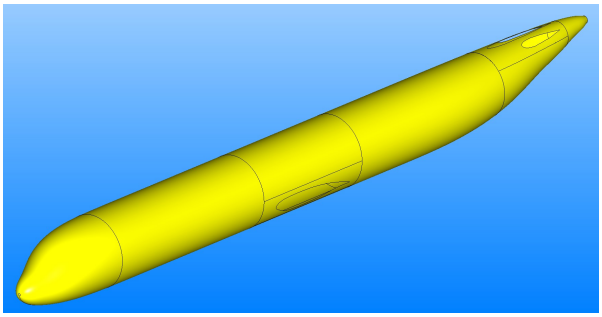

(a) Trimmed fuselage for an aircraft with a conventional tail.

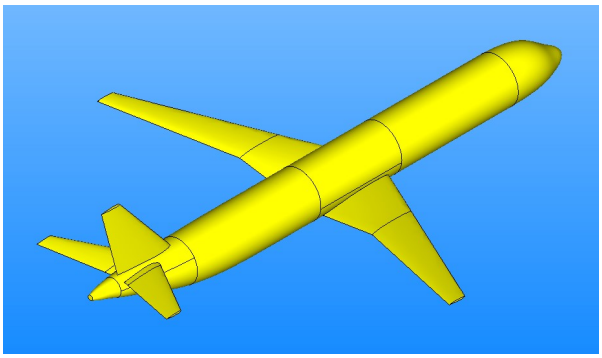

(b) Compound of the trimmed shells that make up the aircraft.

Figure 4.16: Trimmed aircraft.

craft and assume symmetric flow since all of the variables of interest are measured in symmetric flight conditions. In order to obtain a compound of shells that make up the right side of the aircraft, a half-space solid is subtracted from all the shells that form the aircraft. The result can be seen in Figure 4.17.

Weights & Centers of Gravity

Three aircraft versions are considered in the APPU project. First, there is the standard A321neo version that serves as a baseline for the project. Next, there is an A321v3 version; it is an estimate of what the next generation of the A321 could be based on the current developments in jet engine technology. Finally, there is the APPU version that incorporates a hybrid propulsion system consisting of the same main engines of future technology as the A321v3 and a hydrogen-driven propulsor at the back of the fuselage. This study uses the propulsion system, wing position, and empennage position of the A321neo and APPU versions to create four different aircraft configurations that are optimized. The selection of the propulsion system and wing position influences the configuration's operative empty weight, center of gravity, and specific fuel consumption. More details about these configurations are provided in section 5.1. Since the A321v3 version is not used to create these configurations, the remainder of this section focuses solely on the A321neo and APPU versions.

Some attributes are added to the aircraft class to help determine the design and approach weights and centers of gravity of the aircraft. These are required by the aerodynamics and stability & control disciplines. The first step is to find the OEW of the aircraft without the main wing and empennage. This is done by subtracting the HTP, VTP, and main wing weight from OEW as shown in Equation 4.16. The result is denoted as $OEW_{fuselage}$, even though masses like the engines are still included. The results for each aircraft version used in the APPU project are presented in Table A.2. These values for HTP, VTP, and main wing weight are found from estimates earlier in the APPU project.

$$OEW_{fuselage} = OEW - W_{HTP} - W_{VTP} - W_{wing} \tag{4.16}$$

The center of gravity of the operative empty aircraft without the main wing and tail is found from Equation 4.17. The original estimates of the APPU study for the centers of gravity, as well as the results for

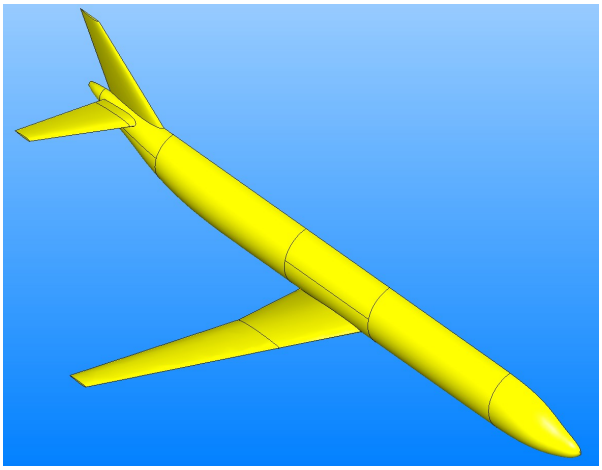

Figure 4.17: Compound of the right side of the aircraft.

the center of gravity without the main wing and tail, can be seen in Table A.3.

$$x_{CG,OE_{fuselage}} = \frac{x_{CG,OE} \cdot OEW - x_{CG,HTP} \cdot W_{HTP} - x_{CG,VTP} \cdot W_{VTP} - x_{CG,wing} \cdot W_{wing}}{OEW_{fuselage}} \tag{4.17}$$

Next, the empennage weight is found from the weight discipline that uses the Raymer equations to calculate the HTP and VTP weight. The implementation of the Raymer equations in the weight discipline is discussed in section 4.3. Two of the inputs of the weight discipline are the tailless OEW and the fuel weight. The tailless OEW is obtained by subtracting the HTP and VTP weight from the OEW. The fuel weight is an input of the aircraft class. The OEW of the aircraft with the current empennage geometry is the sum of the fuselage OEW, the main wing weight, and the empennage weight found from the Raymer equations, as is shown in Equation 4.18. The center of gravity of the operative empty aircraft with the current empennage geometry is calculated with Equation 4.19. The estimation of the center of gravity of the HTP and VTP is explained in subsection 4.2.3. The wing position during the optimization is determined by an input that selects either the APPU or the A321neo wing position.

$$OEW = OEW_{tailless} + W_{HTP} + W_{VTP} + W_{wing} \tag{4.18}$$

$$x_{CG,OE} = \frac{x_{CG,OE_{fuselage}} \cdot OEW + x_{CG,HTP} \cdot W_{HTP} + x_{CG,VTP} \cdot W_{VTP} + x_{CG,wing} \cdot W_{wing}}{OEW} \tag{4.19}$$

The design point for this study is at half fuel load. It is the sum of the operative empty weight, the payload weight, and half the fuel weight as can be seen in Equation 4.20. The approach weight is considered to be the sum of only the OEW and the payload weight as is shown in Equation 4.21. The design weight is used for aerodynamic calculations during cruise, while the approach weight is used for the stability and control derivatives.

$$W_{des} = OEW + W_{payload} + \frac{W_{fuel}}{2} \tag{4.20}$$

$$W_{app} = OEW + W_{payload} \tag{4.21}$$

The center of gravity of the fuel is dependent on the propulsion system and the wing position. If the propulsion system is from the A321neo, there is only a main tank in the wing which fully determines the center of gravity. If the propulsion system is from the APPU aircraft, there is also a hydrogen tank in the back of the aircraft and the center of gravity of the fuel is a weighted average between the two. The center of gravity of the main tank in the wing is determined by the wing position. The center of gravity of the fuel in the case of the APPU version is determined with Equation 4.22. cap_{ker} and cap_{hyd}

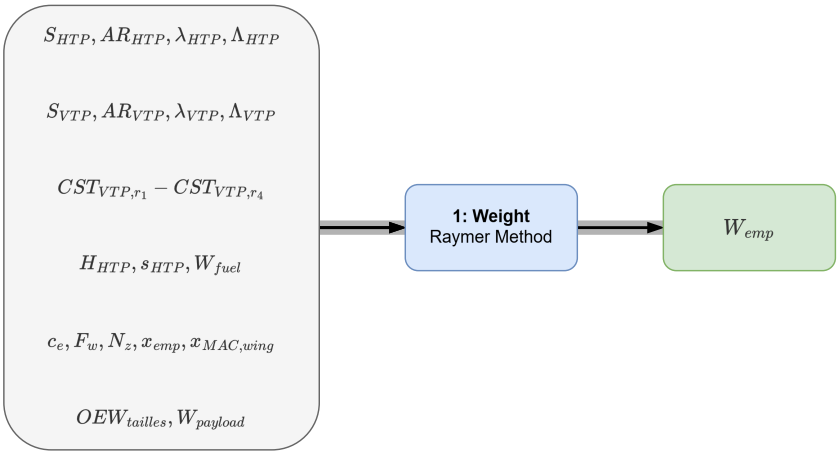

Figure 4.18: Input and output of the weight discipline.

are the maximum capacity of the kerosene and hydrogen tanks. Their values are $18,510kg$ and $832kg$, respectively. $l_{ker,TO}$ and $l_{hyd,TO}$ are the fuel levels in each tank at take-off. According to estimates from the APPU projects, a fuel level of $l_{ker,TO}$ of 0.7578 is sufficient to cover the mission design range with a full hydrogen tank, or $l_{hyd,TO}$ equal to 1.

$$x_{CG,fuel} = \frac{l_{ker,TO} \cdot cap_{ker} \cdot x_{CG,ker} + l_{hyd,TO} \cdot cap_{hyd} \cdot x_{CG,hyd}}{l_{ker,TO} \cdot cap_{ker} + l_{hyd,TO} \cdot cap_{hyd}} \tag{4.22}$$

The center of gravity at the design point and approach are finally calculated with Equation 4.23 and 4.24, respectively.

$$x_{CG,des} = \frac{x_{CG,OE} \cdot OEW + x_{CG,fuel} \cdot \frac{W_{fuel}}{2} + x_{CG,payload} \cdot W_{payload}}{W_{des}} \tag{4.23}$$

$$x_{CG,app} = \frac{x_{CG,OE} \cdot OEW + x_{CG,payload} \cdot W_{payload}}{W_{app}} \tag{4.24}$$

Specific Fuel Consumption

The specific fuel consumption of the aircraft is necessary to calculate the fuel weight from the Breguet equation in the performance discipline. The specific fuel consumption is dependent on the propulsion system. If the propulsion system is the one from the A321neo, the specific fuel consumption is fixed at the specific fuel consumption of its main engines. For the APPU version, a weighted average is considered between the specific fuel consumption of the main engines and the APPU propulsor. The weighted average is based on the thrust fraction delivered by each propulsion system during cruise. The specific fuel consumption for the APPU version is calculated with Equation 4.25. Here, $\phi_{APPU,prop}$ is the thrust delivered by the APPU propulsor as a fraction of the total thrust. $sfc_{APPU,prop}$ and $sfc_{APPU,main}$ are the specific fuel consumption of the APPU propulsor and main engines for the APPU version, respectively. The specific fuel consumption values for the aircraft in this study are described in Table A.5.

$$sfc_{APPU} = \phi_{APPU,prop} \cdot sfc_{APPU,prop} + (1 - \phi_{APPU,prop}) \cdot sfc_{APPU,main} \tag{4.25}$$

4.3. Weight Discipline

A schematic representation of the weight discipline is shown in Figure 4.18. The input of the discipline is visible on the left, while the discipline output is visible on the right. The inputs of the discipline are slightly different from those in the Raymer equation. However, all the required variables in Equation 3.2 and 3.3 can be found from these inputs.

First, all inputs are converted from metric units and degrees to British units and radians because the Raymer equations are designed for British units. There are some variables in Equation 3.2 and 3.3 that

can be taken directly from the input design variables. These include AR_{HTP}, AR_{VTP}, H_{HTP}, S_{HTP}, and S_{VTP}. Other inputs are the parameters of Equation 3.2 and 3.3 that remain constant throughout the optimization process. Their values can be seen in Table A.1 and A.2. F_w is the width of the fuselage intersection near the HTP described in subsection 4.2.5. The ultimate load factor value, N_{ult}, is prescribed by EASA for CS-25 aircraft in this weight category [45]. The operative empty weight excluding the empennage, $OEW_{tailless}$, is found by subtracting the original empennage weight from the operative empty weight (OEW). The OEW depends on the propulsion system.

The remainder of the variables in the Raymer equations are calculated from the discipline inputs. First, b_{HTP} and b_{VTP} are found again from Equation 4.1. Then, the root and tip chords of both the HTP and VTP are calculated from Equation 4.2 and 4.3. The quarter chord sweep angle for the HTP and VTP is found from Equation 4.26. Here, Λ is the leading edge sweep angle and b_{semi} is the semi-span. Since the VTP does not have a mirror wing element at the bottom of the fuselage, the full span is in essence the semi-span, and thus the full span is used for b_{semi} in Equation 4.26 for the VTP.

$$\Lambda_{c/4} = \arctan\left(\frac{\frac{1}{4}c_{tip} + \tan(\Lambda)\, b_{semi} - \frac{1}{4}c_{root}}{b_{semi}}\right) \tag{4.26}$$

The elevator area is determined by Equation 4.27. c_e is the chord fraction of the HTP included in the elevator. K_{uht} is entirely dependent on c_e. if $c_e = 1$, $K_{uht} = 1.143$ else $K_{uht} = 1$.

$$S_e = c_e S_{HTP} \tag{4.27}$$

The next step is to find L_{HTP}, the distance between wing quarter-MAC and tail quarter-MAC. However, to get there, the location of the HTP quarter-MAC must first be determined. The HTP MAC and its y-location are calculated with Equation 4.28 and 4.29, respectively [2].

$$MAC = \frac{2}{3}c_{root}\frac{1+\lambda+\lambda^2}{1+\lambda} \tag{4.28}$$

$$y_{MAC} = \frac{b}{6}\frac{1+2\lambda}{1+\lambda} \tag{4.29}$$

The x-location of the HTP quarter-MAC measured from the nose of the aircraft is found from Equation 4.30. x_{emp} is the x location of the leading edge of the VTP root. $c_{VTP_{HTP}}$ is the local chord of the VTP at the HTP. It is found from Equation 4.31.

$$\begin{aligned} x_{MAC,HTP} = \frac{1}{4}MAC_{HTP} \\ + \tan(\lambda_{HTP})\, y_{MAC,HTP} \\ + s_{HTP} \cdot c_{VTP_{HTP}} \\ + \tan(\lambda_{VTP})\, H_{HTP} b_{VTP} \\ + x_{emp} \end{aligned} \tag{4.30}$$

$$c_{VTP_{HTP}} = H_{HTP} c_{VTP_{tip}} + (1 - H_{HTP})\, c_{VTP_{root}} \tag{4.31}$$

The input quarter-MAC location of the main wing, $x_{MAC,wing}$, is subtracted from $x_{MAC,HTP}$ to find L_{HTP} as shown in Equation 4.32.

$$L_{HTP} = x_{MAC,HTP} - x_{MAC,wing} \tag{4.32}$$

According to Raymer [2], the pitching radius of gyration, K_y, and yawing radius of gyration, K_z, of the aircraft can be estimated by $0.3L_{HTP}$ and L_{HTP}, respectively. The CST coefficients of the VTP root, CST_{VTP,r_1} - CST_{VTP,r_4}, are used to find the thickness to chord ratio at the root, $(t/c)_{root}$. An array of 100 airfoil x-coordinates between zero and one is created. The corresponding y-coordinates are calculated based on the CST coefficients. In general, thickness to chord ratio is the maximum difference between the upper and lower y-coordinates. However, since the VTP has symmetric airfoils, it is simply twice the maximum y-coordinate.

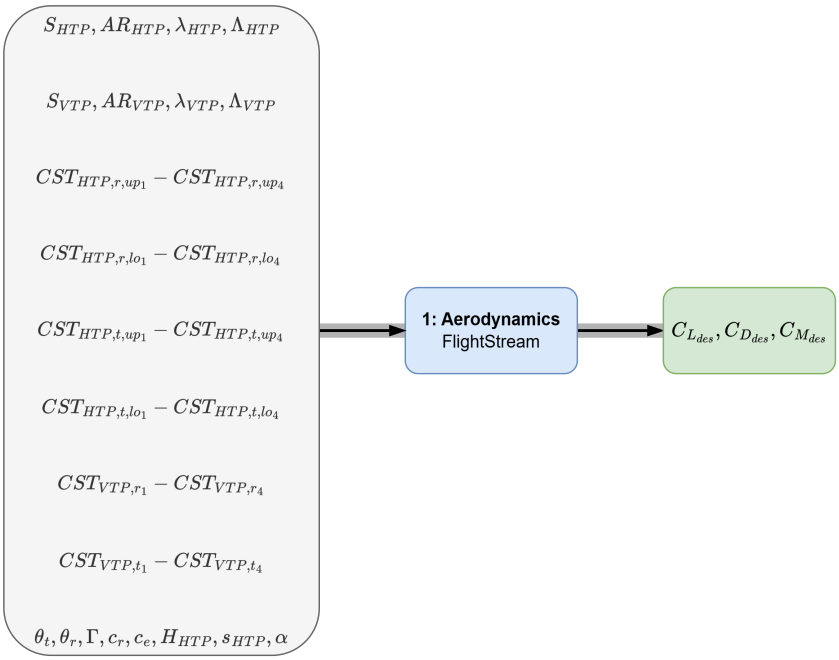

Figure 4.19: Input and output of the aerodynamics discipline with the FlightStream solver.

The only variable of the Raymer equations that is still unknown is the flight design gross weight. However, since this does include the weight of the empennage, there is no way to know the gross weight in advance. To solve this, an iteration loop is set up. Initially, the empennage weight, W_{emp}, is assumed to be 0. The flight design gross weight is calculated using Equation 4.33. Now all the variables in the Raymer equations are known, and the weights of the HTP and the VTP are calculated with Equation 3.2 and 3.3, respectively. The total empennage weight, W_{emp}, is found by adding the two together. The obtained empennage weight is compared with the empennage weight used as input for the flight design gross weight, $W_{emp,old}$ by calculating the relative error shown in Equation 4.34. The iteration loop is stopped when the error is less than 0.001 or 0.1%. Once the final value of W_{emp} is known, it is converted back to the metric unit kg.

$$W_{dg} = OEW_{tailless} + W_{emp} + W_{fuel} + W_{payload} \tag{4.33}$$

$$e = \frac{|W_{emp} - W_{emp,old}|}{W_{emp}} \tag{4.34}$$

4.4. Aerodynamics Discipline

Two separate aerodynamics disciplines have been created in order to investigate the attainable fidelity level of the aerodynamic solver in optimization studies such as this one. The high-fidelity version of the discipline is based on the FlightStream flow solver, while the low-fidelity version is based on AVL. First, the implementation of the high-fidelity version is presented, followed by the low-fidelity solver implementation.

4.4.1. FlightStream

FlightStream version 24.1 is used for the aerodynamics discipline with the higher fidelity level of the two. The schematic representation of the aerodynamics discipline with FlightStream is shown in Figure 4.19. This subsection discusses how the mesh generation is automated for the generated geometries, some settings that are set to run the simulations as desired, and finally a mesh convergence study and some issues that were discovered throughout the process.

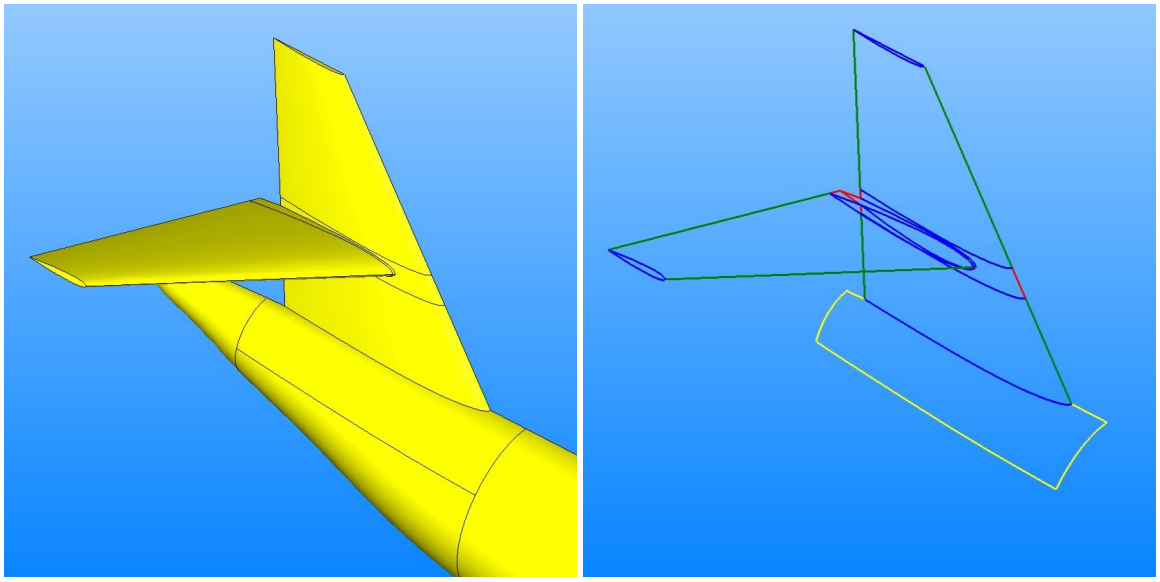

(a) Right side empennage geometry **(b)** Separated edge.

Figure 4.20: Empennage edges automatically separated into categories (fuselage edges in yellow, short edges in red, leading and trailing edges in green, and airfoil edges in blue).

Mesh

The mesh class takes an aircraft from the aircraft class as an input and automatically applies a mesh to it. A mesh is generated for a compound of the right side of the aircraft described in subsection 4.2.6 with the Salome library in ParaPy. In order to create a surface mesh with Salome, 1D controls need to be applied to the geometry edges and 2D controls to the geometry faces.

The first step is to group all the edges where the same 1D controls need to be applied. The same controls cannot be applied to every edge. For instance, airfoils need to have good curvature resolution, while spanwise leading and trailing edges need to resolve spanwise lift distribution and have matching numbers of mesh elements. For the fuselage and main wing, these groups are hard-coded by using the edge indices. Since their geometry does not change throughout the optimization process, their index does not vary either. This prevents controls from being applied to the wrong edge, which might result in bad or even infeasible meshes. This method of indexing cannot be applied to the empennage because the number of edges does vary throughout the optimization process. The classification of edges in the empennage happens automatically depending on certain criteria that are met for the edge or not.

Regarding the empennage, the edges are divided into 9 different categories. A separate category exists for the leading and trailing edges of both the HTP and VTP. Edges that are part of airfoils are separated, as well as short edges that connect other elements. The three edges at the base of the empennage that border the fuselage geometry are classified individually such that the controls applied to the corresponding fuselage edges can easily be copied. The next group of edges that get classified are short edges. An edge is considered a short edge when its length is less than 10% of the HTP span. If an edge is longer than the cut-off length, it is passed on to the next criteria. Edges that are straight and lie completely on the aircraft's symmetry plane are classified as VTP spanwise edges. A difference is made between leading and trailing VTP edges based on the sweep angle of the edge. If the taper ratio is limited to values below 1, the sweep angle of the leading and trailing edges cannot be the same. Edges that are long enough, straight, but do not lie entirely on the aircraft's symmetry plane are HTP spanwise edges. Again, a differentiation is made between the leading and trailing edges based on the sweep angle. The edges that do not meet any of these previous criteria are classified as airfoil edges. The resulting classification of an example empennage is visualized in Figure 4.20.

To classify the faces of the aircraft geometry, two groups are created: quad faces and triangular faces. Quad faces are faces where a structured grid will be created, and triangular faces are faces where

Setting	Value
quad_dominant	False
only_2d	False
growth_rate	0.05
fineness	'UserDefined'
nb_seg_per_edge	1
nb_seg_per_radius	10
limit_size_by_surface_curvature	False

Table 4.1: 2D control inputs for the triangular faces.

an unstructured grid will be generated. An unstructured grid is created on faces that do not have four edges and have a harder geometry to create a structured grid, such as wing tips and the areas where wing elements are mounted onto other elements. Similar to the edges, the faces of the fuselage and main wing are classified based on their index. For the empennage, an automated solution is required again. The faces where one of the leading edges from both HTP and VTP from the edge classification is part of the face are classified as quad faces. All others are triangular faces. This results in a structured mesh on both upper and lower surfaces of wing elements, except at the 'seams', and an unstructured mesh elsewhere.

The 1D controls determine the location of mesh nodes on the edges. On lifting surfaces, except for the unstructured areas, nodes are positioned on the edges such that their density increases towards both ends of the edge in both chordwise and spanwise directions. This means that the mesh density increases towards the leading and trailing edge in chordwise direction and towards the wing tip and root in spanwise direction. For the main wing, the mesh density also increases at the kink in spanwise direction. The distance between two consecutive nodes increases exponentially towards the middle until a maximum distance between two consecutive nodes is reached. At this point, the distance between consecutive nodes no longer increases but remains constant until it starts decreasing again at the other side. The distance between nodes at both ends of the edge and the maximum distance between nodes are determined by inputs as a fraction of the edge length. Separate inputs exist for these fractions for the chord- and spanwise edges of both the main wing and empennage. Additionally, the growth rate in chord- and spanwise directions can be set with the inputs as well, resulting in a total of ten inputs to determine the mesh on lifting surfaces.

The nodes on the fuselage in longitudinal direction are spaced at increasing distances from the nose and remain at a constant distance between nodes past the cockpit to capture the curvature at the nose well. The distance between nodes at the nose and the constant distance between nodes past the cockpit are controlled by two inputs. A fixed number of nodes is placed on fuselage edges in radial direction. The number of nodes is set as an input of the mesh class. The remaining 1D controls are imposed on the short edges of the empennage. Here, nodes are placed at constant intervals. The distance between two neighboring nodes is set equal to the smallest distance between two nodes on the HTP leading edge.

The unstructured parts of the mesh are mainly determined by the 2D controls on the faces with an unstructured mesh. The same 2D controls have been applied to all of these faces. The settings of these controls can be seen in Table 4.1. Two separate VTK files are written containing all the mesh edges and nodes: one for the structured grid and one for the unstructured grid. These VTK files are imported into FlightStream. An example of a mesh can be seen in Figure 4.21. Some more detailed views of the mesh can be seen in Appendix B.

FlightStream Settings

Table 4.2 shows some of the basic settings for the CFD simulations in FlightStream. The only results of the FlightStream simulations that are of interest during the optimization process are the lift, drag, and pitching moment during cruise. Based on these criteria, the sideslip angle is set at zero. FlightStream does not allow users to set a target lift coefficient and calculate the required angle of attack

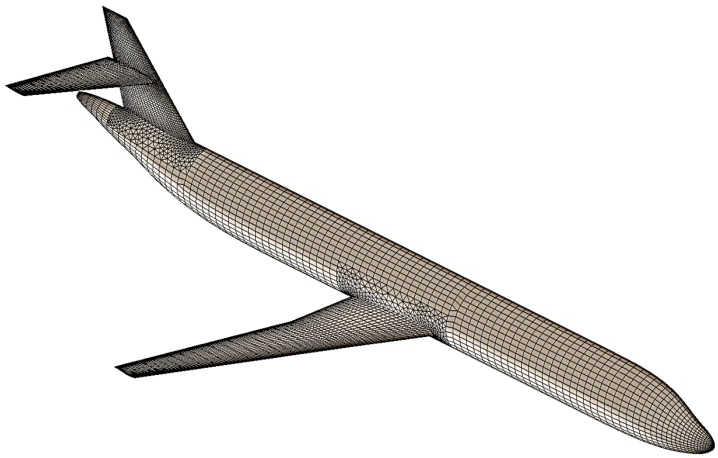

Figure 4.21: automatically generated mesh on an aircraft with an example empennage design.

Setting	Value	Unit
sideslip angle	0	°
freestream velocity	V_{cruise}	m/s
reference velocity	V_{cruise}	m/s
reference area	S_{wing}	m^2
reference length	MAC_{wing}	m
iterations	2000	-
convergence limit	$1{\cdot}10^{-5}$	-
forced run	False	-
wake size	100	%
moments model	pessure	-

Table 4.2: FligthStream settings.

automatically, like in many simpler solvers such as AVL. The angle of attack is therefore added to the design vector, and an equality constraint is used to guarantee that the lift is equal to the weight. The angle of attack for each FlightStream simulation is set by the value determined by the optimizer. The freestream velocity and reference velocity are set equal to the cruise speed of the A321neo and APPU aircraft. The reference area and length are the A321 main wing surface area and mean aerodynamic chord [46]. The convergence limit is set equal to the default value, which is supposed to be well converged. The maximum number of iterations is set at 2000. It has been found from practice that this is high enough such that the convergence limit is reached before the maximum number of iterations is reached. The solver is not forced to run all iterations when the convergence limit has been reached to reduce the computational time. The wake size is set at 100% of the average surface mesh size. This is considered fine compared to the default value. It could be increased to increase the computational speed. The pressure model is used to calculate the aerodynamic moments instead of the vorticity model. The vorticity model outperforms the pressure model only in specific cases, such as when modeling propellers and rotors with thin mean camber surfaces instead of solid bodies [47].

FlightStream has different compressibility models that can be selected on the basis of the Mach number. The cruise conditions for this study are at Mach 0.78. FlightStream's transonic compressibility model is valid between Mach 0.6 and Mach 1. The cruise conditions are close to the middle of the applicable domain, making it the obvious choice. However, there are also some limitations to the transonic model. Currently, clean shocks are not captured by the transonic solver. The shocks are smeared in the pressure distribution. Despite the smeared shocks, the transonic model produces accurate loads for supercritical transonic flows and is readily applied to subcritical transonic flows. This solver limitation is expected to be addressed in the near future. An additional drawback of the transonic solver is the

Property	Value	Unit
density	ρ_{cruise}	kg/m^3
pressure	p_{cruise}	Pa
temperature	T_{cruise}	K
viscosity	μ_{cruise}	Ns/m^2
speed of sound	a_{cruise}	m/s

Table 4.3: Fluid properties at cruise altitude.

relatively high runtime and memory usage compared to other models, such as the sub- and supersonic models [47].

The fluid properties for the FlightStream simulations are obtained from the international standard atmosphere at cruise altitude. The fluid properties set during the simulations can be seen in Table 4.3. The exact values for these properties are given in Table A.4.

Base regions and trailing edges are detected automatically. The trailing edge maximum sweep angle is set at 35°. The trailing edge bluntness angle is the maximum vector angle between the two mesh face normal vectors that share a single mesh edge. It is kept at the default value of 140°. The base region bending angle is set at the default value of 15°. The wake is terminated at the default distance, which is equal to the length of the geometry downstream of the last mesh face [47].

Mesh Convergence & Issues

In order to study the mesh convergence of the aerodynamics discipline, the lift, drag, and pitching moment are calculated at different levels of mesh refinement. The plan is to start with a fine mesh in all directions, increase the size in one direction until the results diverge, and repeat in another direction until the whole mesh has been done. This should result in values for the mesh class inputs that return reliable results while keeping the run time to a minimum by making the mesh coarser.

The first direction to be studied is the wing elements in chordwise direction. There are four inputs that control the chordwise node distribution of the wing elements. There are two inputs for the main wing and two inputs for the empennage chordwise distribution: the edge fraction at the leading and trailing edge (they are the same), and at the center chord for both the main wing and empennage. In order to study the mesh convergence as a function of the chordwise mesh refinement, these inputs are all varied simultaneously. The result is a mesh with a uniform distribution along the chord that gets coarser with increasing values for the inputs. Once the critical level has been found for the uniform distribution in chordwise direction, the spacing at the center chord can be increased while keeping the spacing at the leading and trailing edges constant until it diverges again. This is because there is less rounding and variation in the pressure distribution near the center of an airfoil. This would result in a lower face count and a lower run time.

For the uniform chordwise distribution, the four inputs are varied between 0.01 and 0.05. The most refined mesh has 100 nodes along the chord for both the upper and lower faces of the wing elements. The coarsest mesh has 20 nodes in chordwise direction per face. 25 data points are created between these two extrema. The values of the remaining inputs of the mesh class can be seen in Table 4.4. These inputs are in accordance with the guidelines for simulations in FlightStream or even more refined than what is advised [47].

The results of the uniform mesh convergence study are visualized in Figure 4.22. As stated before, low values for mesh edge length fraction correspond to fine meshes and high values to coarse meshes. Note that the viscous drag component $C_{D_{0,des}}$ is not calculated in the mesh refinement study. Consequently, the total drag $C_{D_{des}}$ would overlap with the induced drag $C_{D_{i,des}}$ on the plot, and is thus not plotted. The viscous drag is not calculated because all physics are based on the inviscid pressure distribution in FlightStream. The angle of attack is set at 1 degree during the convergence study. A non-zero angle of attack is advised for mesh convergence studies [47]. The lift, drag, and pitching

Input	Value
main wing outer span fraction	0.02
main wing inner span fraction	0.04
empennage outer span fraction	0.02
empennage inner span fraction	0.04
fuselage radial nodes	30
fuselage longitudinal distance	0.25
fuselage longitudinal distance at nose	0.05

Table 4.4: Constant mesh class inputs during the mesh refinement in chordwise direction.

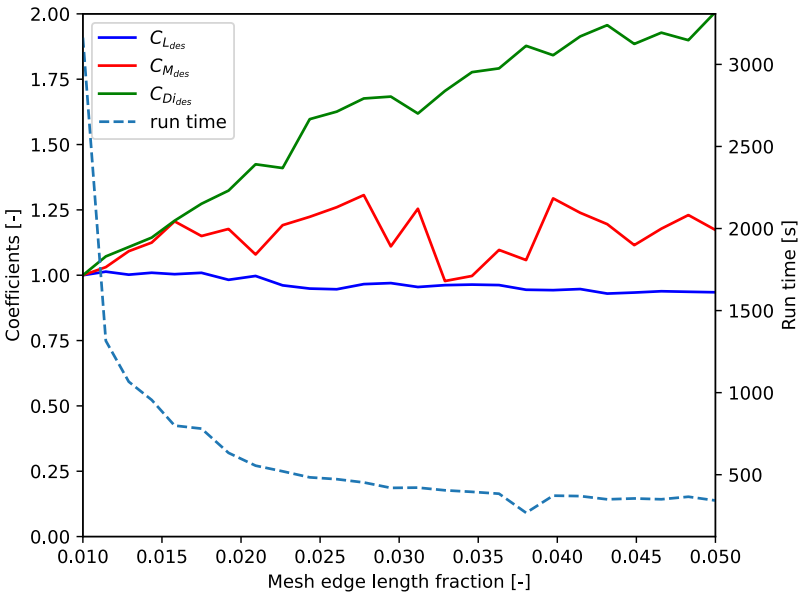

Figure 4.22: Mesh convergence for uniform chordwise mesh refinements.

moment are normalized with respect to their values for the most refined mesh. The lift appears to be relatively stable throughout the convergence study. This is not the case for the drag and pitching moment, which do not look stable for any part of the studied domain. The pitching moment fluctuates between a normalized value of 1 and 1.25. The drag keeps diverging throughout the entire tested domain. This issue could possibly be resolved by creating even more refined meshes. However, the run time of the finest mesh is already higher than an acceptable level for this optimization study. The run time of the FlightStream simulations is represented with the blue dashed line in Figure 4.22. The scale for the run time is on the right y-axis. The run time of the finest mesh is above 3,000 seconds, or 50 minutes. If each aerodynamics discipline evaluation takes 50 minutes or more, the total optimization process could easily take weeks or even months.

There are more issues in the current FlightStream implementation that hinder its usefulness in optimization studies such as this. The first of these issues reveals itself upon taking a closer look at the pressure distribution of one of the FlightStream solutions. Figure 4.23 shows the pressure coefficient at the root of the trailing edge for the suction side of the main wing and horizontal tail plane. It is clear that the pressure coefficient drops significantly to unexpected values at the cell that is closest to the trailing edge root on the suction side of both the main wing and horizontal tail plane. Such low values are not expected in these regions. Refining the grid seems to have an adverse effect on the issue, resulting in an even bigger drop in pressure. The best results were obtained for a chordwise mesh length fraction of 0.02 at the leading and trailing edges. These are the results shown in Figure 4.23.

Despite the issues mentioned above, a test run of the optimization using FlightStream for the aerody-

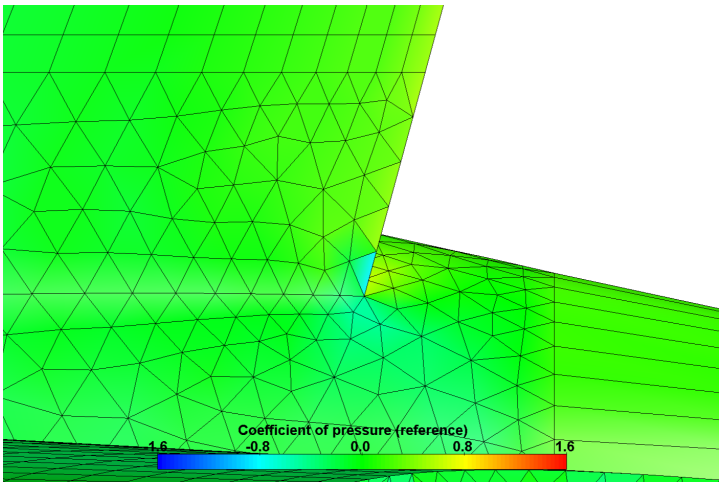

(a) Horizontal tail plane (upper surface).

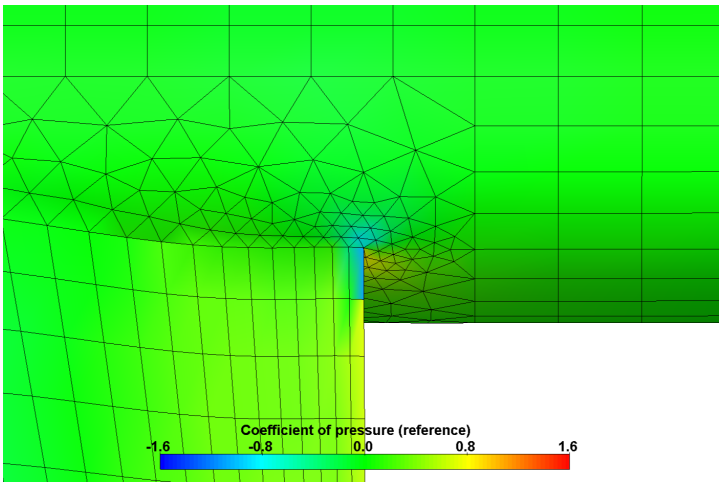

(b) Main wing (lower surface).

Figure 4.23: FlightStream solution for pressure distribution on pressure side of wing elements.

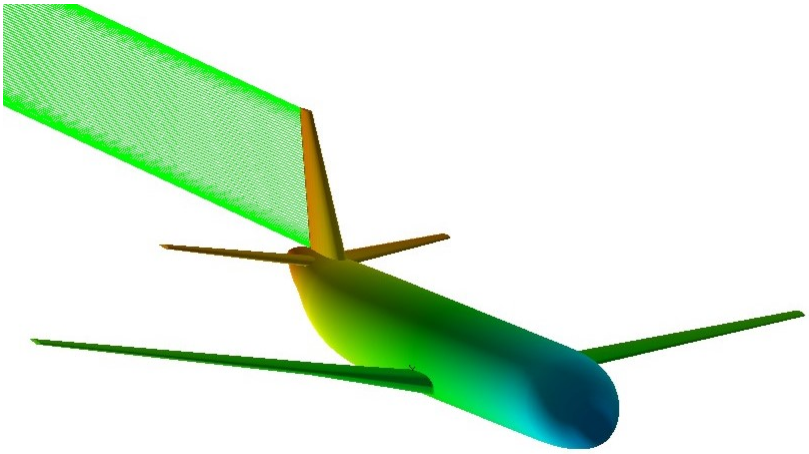

Figure 4.24: Failed trailing edge detection on the main wing and HTP.

namic analysis has been performed. This test run uncovered some additional issues. The automatic trailing edge detection did not consistently work as required. The trailing edges of both the main wing and HTP did not get detected as trailing edges by FlightStream. An example of such a run can be seen in Figure 4.24. The trailing edge detection failure is apparent from the lack of wake strands propagating from the respective trailing edges. It is worth noting that either both the main wing and HTP trailing edges got detected or neither, never only one of them. Additionally, the geometry and mesh of the main wing do not change throughout the optimization process, making it even more peculiar that the trailing edge on the main wing is not consistently detected. Runs where the trailing edges are not properly detected result in very low estimates for the lift and induced drag. The issue is not present constantly, but frequently enough to potentially have a significant influence on the gradient evaluations.

Another issue became apparent after the first iteration of the test run. The estimate of the optimum after the first iteration results in a design that is unfeasible in reality. The design after iteration one of the optimization test run can be seen in Figure 4.25. The main issue here is that the mesh class crashes the entire optimization run. The base of the empennage is positioned very forward, which causes the split plane at the front of the empennage to be in front of the aft split plane of the wing. As a result, the fuselage gets split at the wrong location, and the indices of the edges no longer correspond to the assumed indices in the mesh class for the fuselage. Another issue, although less drastic, with designs like these is that the Raymer equations to estimate the empennage mass are no longer valid. Empirical methods, such as the Raymer equations, are based on data from real aircraft. This makes them only applicable within a domain of realistic designs that are somewhat similar to existing designs. This design is far from any empennage designs that are out there at the moment, making the use of the Raymer equations questionable at least. This issue could potentially be solved by applying more reasonable bounds on some design variables. The very forward position, for instance, is mainly a result of the high sweep angle, aspect ratio, and surface area of both the HTP and VTP. Reducing the upper bound on (some of) these design variables could prevent designs such as this one. If still required after altering the bounds, changes could be made to the mesh class to make it more robust.

After the optimization test run, it has been decided that all of these issues could not be fixed in a timely manner. Especially since it appears that the run time of individual cases would be too long to be applicable in this optimization study. Therefore, it is concluded that enhanced panel methods, such as FlightStream, are not viable within optimization studies run on personal computers such as this one at the moment.

4.4.2. AVL

AVL version 3.36 is used for the low-fidelity level aerodynamics discipline. Since AVL is also the tool that is used for the stability and control derivatives, it makes sense to combine the two disciplines into one when the low-fidelity aerodynamics discipline is used. Therefore, the stability and control derivatives

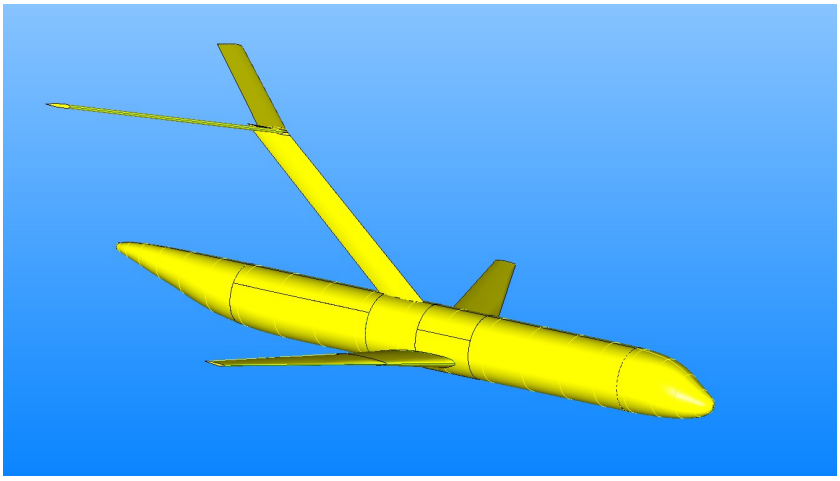

Figure 4.25: Unfeasible estimate for the optimum design after one iteration of the optimization test run.

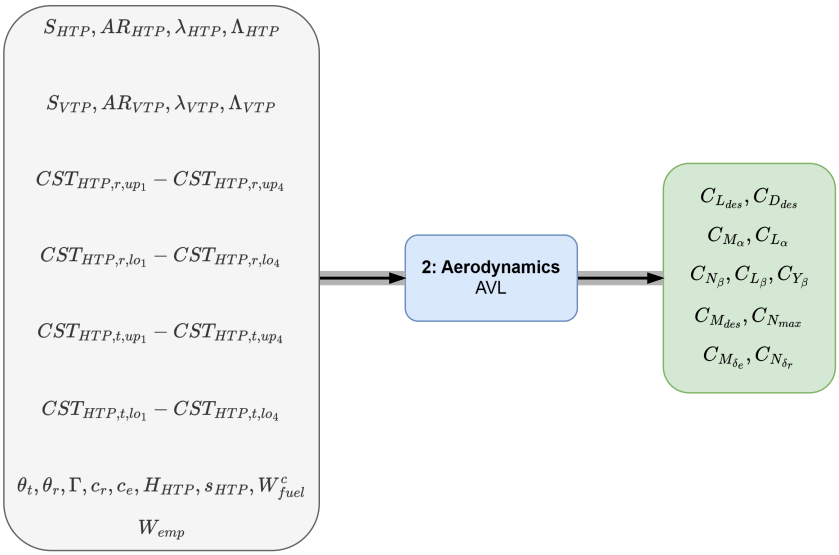

Figure 4.26: Input and output of the aerodynamics discipline with the AVL solver.

are also shown as outputs of the AVL aerodynamics discipline in Figure 4.26. First, the conversion of the aircraft geometry to AVL lattices is presented, followed by the AVL settings for the aerodynamic performance at the design point. Finally, an expansion on the drag model in AVL is outlined. The settings for the stability and control derivatives are described in section 4.5. A convergence study for both the AVL aerodynamics and the stability & control discipline is discussed in section 4.6.

AVL geometry

In AVL, it is common practice to ignore the fuselage and extend the wings to the center line so that the left and right sides meet [23]. Adaptations must be made to the geometry generated as described in section 4.2. More particularly, the main wing does not extend to the center line. The main wing is extended as shown in Figure 4.27a. An airfoil is placed on the symmetry plane. Next, a ruled solid is created between the root airfoil of the right and left wings and the center airfoil. The center airfoil has the same shape as the root airfoil but is scaled and positioned such that the sweep angles and dihedral angles of the leading and trailing edges are constant from the center to the kink in the middle of the wing on each side. This is accomplished by extrapolating the chord length, leading edge position, and incidence angle from the kink and root.

AVL requires a flat plate geometry that represents the wing planform and sections that describe the

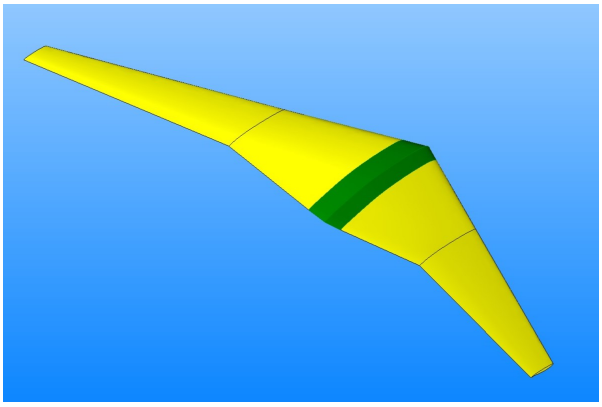

(a) Extended main wing to the center line.

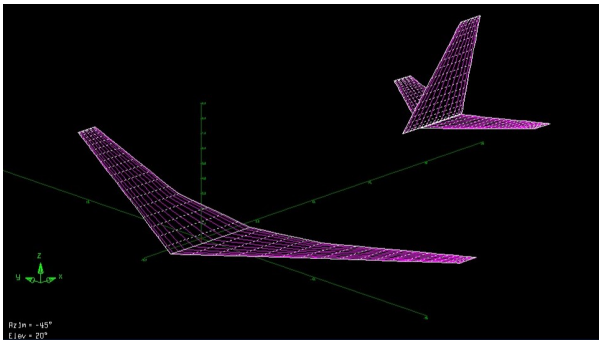

(b) AVL vortex lattice.

Figure 4.27: Geometry to AVL model conversion.

mean camber line and incidence angle at different locations as inputs [48]. The VTP, right side of the HTP, and extended main wing are converted into flat plates. A duplicate is created in AVL to obtain the left side. Sections are created from the center, root, kink, and tip airfoil of the main wing and the root and tip airfoil of both the HTP and VTP. Controls are applied to the sections of the HTP and VTP to be able to investigate the elevator and rudder effectiveness. The location of the hinge line is determined by the design vector, and the gain is set at 1 for both the elevator and the rudder. The duplicate sign is set at 1 for the elevator controls such that the left side of the elevator deflects symmetrically [23].

AVL generates a vortex lattice on the wing surfaces. For the main wing and the HTP, a cosine spreading is applied to the lattice in chordwise direction and a negative sine spreading in spanwise direction. The cosine spreading increases the density of the lattice towards the leading and trailing edge, while the negative sine spreading increases the density from the center line towards the wing tip. No dense lattice structure in spanwise direction is necessary at the center line since the main wing and HTP are duplicated. A cosine spreading is applied in both chordwise and spanwise direction for the VTP since there is no duplicate present. The resulting lattice can be seen in Figure 4.27b.

AVL Settings

Table 4.5 shows the remaining settings required for AVL. The exact values for this study are presented in Appendix A. Note that AVL uses the reference span to define roll and yaw moments instead of the reference chord, such as in the FlightStream aerodynamics discipline described in subsection 4.4.1. AVL uses the Prandtl-Glauert correction to treat compressibility. The Prandtl-Glauert correction is valid up to a perpendicular Mach number of 0.7. Transonic flow is likely to occur between Mach 0.7 and 0.8, making the use of the Prandtl-Glauert correction questionable. Beyond Mach 0.8, there is almost certainly going to be transonic flow, making Prandtl-Glauert invalid. The perpendicular Mach number can be calculated with Equation 4.35, where M_{perp} is the perpendicular Mach number and M is the freestream Mach number. Λ is the wing sweep angle [23]. When allowing for a maximum perpendicular Mach number of 0.7, a critical sweep angle can be found for Mach numbers higher than 0.7. The

Setting	Value	Unit
Mach number	M_{cruise}	-
reference area	S_{wing}	m^2
reference chord	MAC_{wing}	m
reference span	b_{wing}	m

Table 4.5: AVL settings [46].

freestream Mach number in this study is 0.78. This results in a critical sweep angle of 26°. If any sweep angles in the final design are less than this critical value, the results need to be interpreted with caution. Since transonic effects are known to occur on the main wing of the A321neo, the resulting aerodynamic forces and moments are expected to deviate from reality.

$$M_{perp} = M \cos(\Lambda) \tag{4.35}$$

The angle of attack for the simulation is constrained by the required lift coefficient at the design point. AVL automatically calculates the required angle of attack to meet this lift coefficient. The lift coefficient at the design point is calculated with Equation 4.36. The design weight varies throughout the optimization and is found from Equation 4.20. ρ_{cruise} and V_{cruise} are the density at cruise altitude and cruise velocity. S_{wing} is the main wing surface area that is used as the reference area for AVL. The only results of interest from the cruise conditions are the drag and pitching moment coefficients. The conditions to obtain the remaining stability and control derivatives are explained in section 4.5.

$$C_{L_{des}} = \frac{2W_{des}}{\rho_{cruise} V_{cruise}^2 S_{wing}} \tag{4.36}$$

Drag Model

AVL calculates only the induced drag and ignores other forms of drag. This results in theoretically very efficient aircraft with high lift-to-drag ratios. As a result, the estimates for the fuel load from the Breguet equation are very low. In order to overcome this issue, a friction drag component is added to the induced drag to obtain the drag coefficient at the design point, as is shown in Equation 4.37. Here $C_{D_{i,des}}$ is the induced drag coefficient at the design point from AVL and C_{D_f} is the friction drag coefficient.

$$C_{D_{des}} = C_{D_{i,des}} + C_{D_f} \tag{4.37}$$

The friction drag coefficient varies linearly with the wetted surface area, as can be seen in Equation 4.38 [49]. C_f is the friction coefficient. S_{wet} and S_{wing} are the wetted surface area and the wing reference area, respectively.

$$C_{D_f} = C_f \left(\frac{S_{wet}}{S_{wing}} \right) \tag{4.38}$$

The value of C_f is calibrated such that the required fuel load for the design range is equal to the fuel load of the A321neo in reality.

4.5. Stability & Control Discipline

AVL version 3.36 is used for the stability and control discipline. As discussed in subsection 4.4.2, AVL is also the tool that is used for the low-fidelity aerodynamics discipline. The two disciplines are combined into one when the AVL version of the aerodynamics discipline is used. The inputs and outputs of the stability and control discipline are shown in Figure 4.28. The conversion of the aircraft geometry to AVL lattices has already been presented in subsection 4.4.2. This section discusses the AVL settings that apply for the stability and control derivatives and a mesh convergence study of these derivatives.

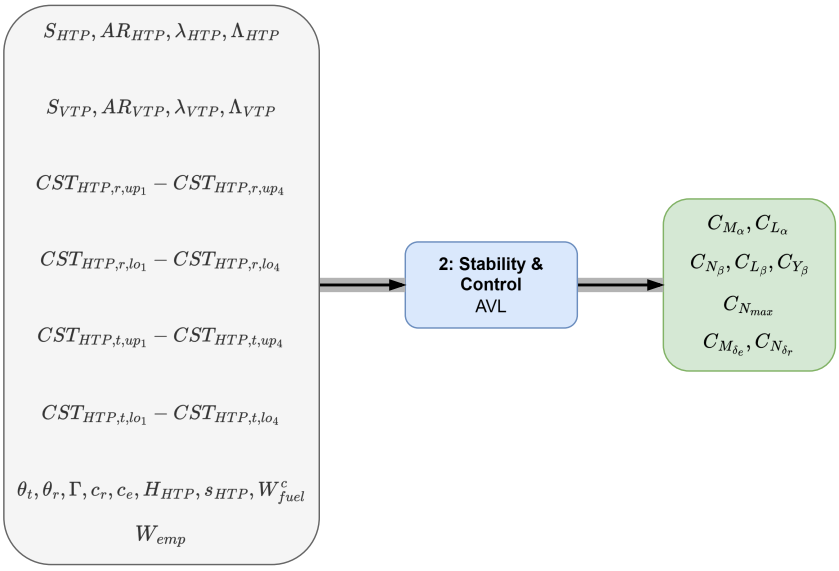

Figure 4.28: Input and output of the stability and control discipline.

4.5.1. AVL Settings

Unlike the drag and moment at the design point, the stability and control derivatives are calculated at the lowest speed to occur during flight, which is typically at approach. The Mach number at approach is 0.21 for this study, at which incompressible flow can be assumed. Therefore, the Mach number is set at 0 for the calculation of the stability and control derivatives since this decreases the computational time of AVL [23]. The required lift coefficient is calculated with Equation 4.39. Here W_{app} is the aircraft weight at approach. This is assumed to be the OEW plus the payload weight. The approach speed, V_{app}, and density, ρ_{gr}, are given in Table A.4. The air density is taken at ground level. The main wing surface area, S_{wing}, remains unchanged and can be found in Table A.1. $\Delta c_{L_{flaps}}$ is the difference in lift coefficient that is obtained by deploying the flaps at a fixed angle of attack. This is subtracted from the approach lift coefficient such that the AVL simulations occur at the correct angle of attack. Based on findings from literature, $\Delta c_{L_{flaps}}$ has been set at 0.6 [50].

$$c_{L_{app}} = \frac{2W_{app}}{\rho_{gr} V_{app}^2 S_{wing}} - \Delta c_{L_{flaps}} \tag{4.39}$$

All the stability and control derivatives are calculated at zero sideslip, except for the maximum yawing moment $C_{N_{max}}$. The maximum yawing moment is calculated at the maximum sideslip angle before the VTP stalls. Based on findings from literature, the maximum sideslip angle has been set at 25° [51].

4.6. AVL Mesh Convergence

A similar mesh convergence study to the FlightStream version of the aerodynamics discipline is performed for the aerodynamics and stability & control discipline based on AVL. First, the effect of the number of nodes in chordwise direction is considered. The number of nodes on every wing element in spanwise direction is set constant at 30. The nodes in chordwise direction are varied between 2 and 30. Next, the spanwise direction is investigated by setting the number of nodes on every wing element in chordwise direction constant at 20. The nodes in spanwise direction are varied between 13 and 41.

4.6.1. Aerodynamics

The normalized induced drag and pitching moment coefficients are plotted in Figure 4.29a along with the influence of the number of nodes on the run time of a single discipline evaluation. It can be seen that for 12 nodes in chordwise, both coefficients have converged within 99% of their final value. The run time is still relatively low at 12 nodes.

The normalized induced drag and pitching moment coefficients for the spanwise variation are shown

in Figure 4.29b. The induced drag and pitching moment may not seem to converge at first glance, but upon closer inspection, it can be seen that neither of both varies more than approximately 1.5% from its final value. The variance throughout the domain could be explained by the kink in the trailing edge of the main wing. The results may vary depending on how well the nodes align with the location of the kink. Nonetheless, the results are considered converged throughout the entire tested domain within 98.5%.

4.6.2. Stability & Control

For the stability and control discipline, instead of the drag and pitching moment, the convergence of the stability and control derivatives is investigated. This time a convergence criterion is set. The criterion for measures of stability is that the discretization error should be smaller than the effect of changing HTP and VTP size by 1%. For controllability, it should be smaller than the effect of changing control surface size by 1%. To investigate the stability derivatives, the HTP and VTP surface areas are increased by 1%. For the control derivatives, the elevator and rudder area are increased by 1%. Throughout the convergence studies, the hinge line of both the elevator and rudder is located at 70% of the chord. To increase the control surface area by 1%, the hinge line is relocated to 69.7%. Just like the other stability and control derivatives, the results of the increased empennage and control surface area are normalized with respect to the results of the finest mesh. The difference between these results and the finest results is added and subtracted to and from the finest results to find an upper and lower bound for each of the stability and control derivatives. The stability and control derivatives are considered converged when each derivative is within its own lower and upper bound.

The results of the chordwise convergence study are visualized in Figure 4.30a, and Figure 4.30b for the spanwise convergence study. The lower and upper convergence bounds for each derivative are represented by the dashed line in the same color as the derivative. The stability derivatives are all converged for the same number of nodes as is set in the AVL convergence study of the aerodynamics discipline, both in chord- and spanwise direction. The control derivatives appear to require more chordwise nodes to converge. Convergence only occurs at 20 chordwise nodes. All derivatives are converged in spanwise direction for the entire tested domain. Based on these findings, combined with the results of subsection 4.6.1, the final grid is set at 20 nodes in both chord- and spanwise direction to find a balance between accuracy and computational speed.

4.7. Performance Discipline

The schematic representation of the performance discipline is shown in Figure 4.31. The input of the discipline is visible on the left, again, while the discipline output is visible on the right. These inputs need some operations to make them useful for the Breguet range equation.

First, the final weight is calculated as the sum of the operative empty weight without tail, empennage weight, and payload weight as is shown in Equation 4.40. Note that the Breguet equation is designed for weights in units of force (N). Although it is technically not correct, weights are expressed in units of mass (kg) in this study. As a result, the masses are scaled by the gravitational constant, g, to obtain the final weight in Newtons. Additionally, the specific fuel consumption, sfc, also needs to be scaled by g since Equation 3.25 uses N/Ns as the unit for sfc. Often, like in this study, the specific fuel consumption is expressed in kg/Ns.

$$W_f = g\left(OEW_{tailless} + W_{emp} + W_{payload}\right) \tag{4.40}$$

The performance discipline estimates the fuel load required to cover the mission design range. Equation 3.25 is reordered so that the result is the initial weight as a function of the design range and the final weight as is shown in Equation 4.41.

$$W_i = \left(\frac{R}{2}\sqrt{\frac{\rho S_{wing}}{2c_{L_{des}}}} \times sfc \times c_{D_{des}} + \sqrt{W_f}\right)^2 \tag{4.41}$$

The fuel weight required for the design range is calculated by subtracting the final weight and dividing by the gravitational constant again, as can be seen in Equation 4.42.

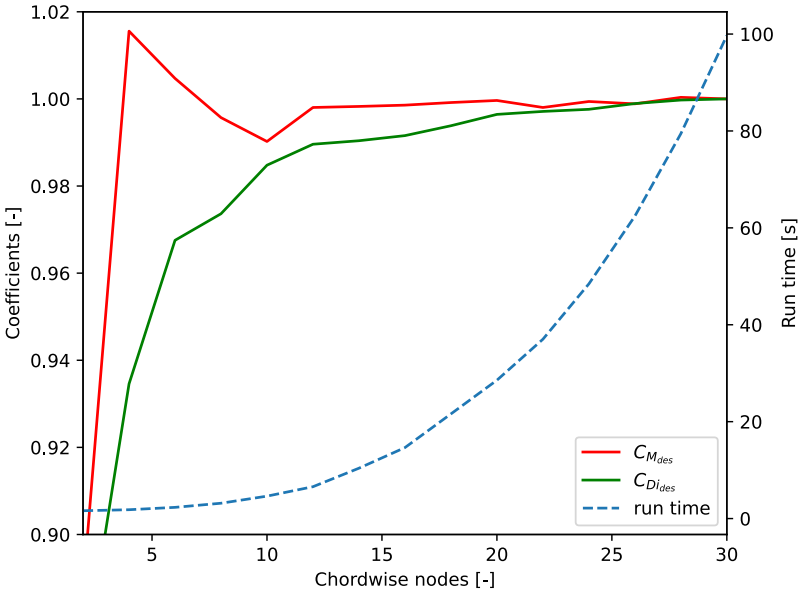

(a) Mesh convergence in chordwise direction with 30 nodes in spanwise direction on every wing element.

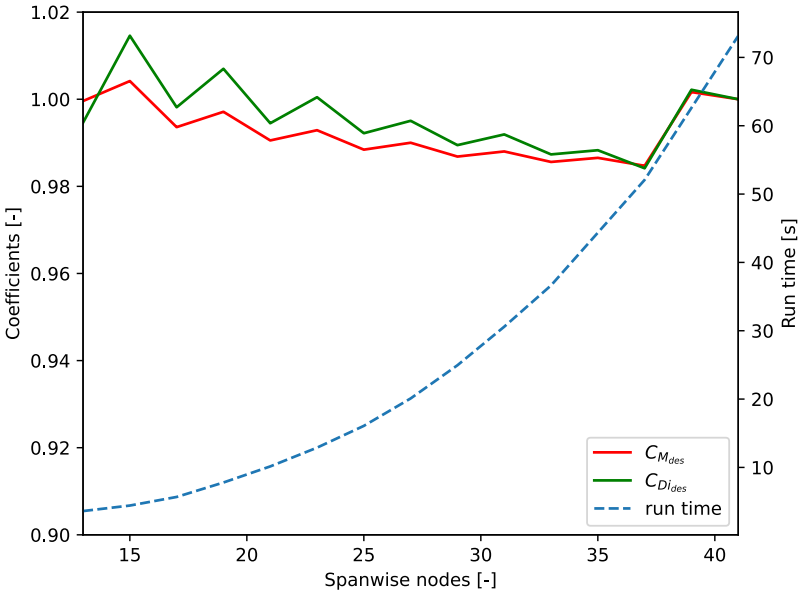

(b) Mesh convergence in spanwise direction with 20 nodes in chordwise direction on every wing element.

Figure 4.29: AVL mesh convergence.

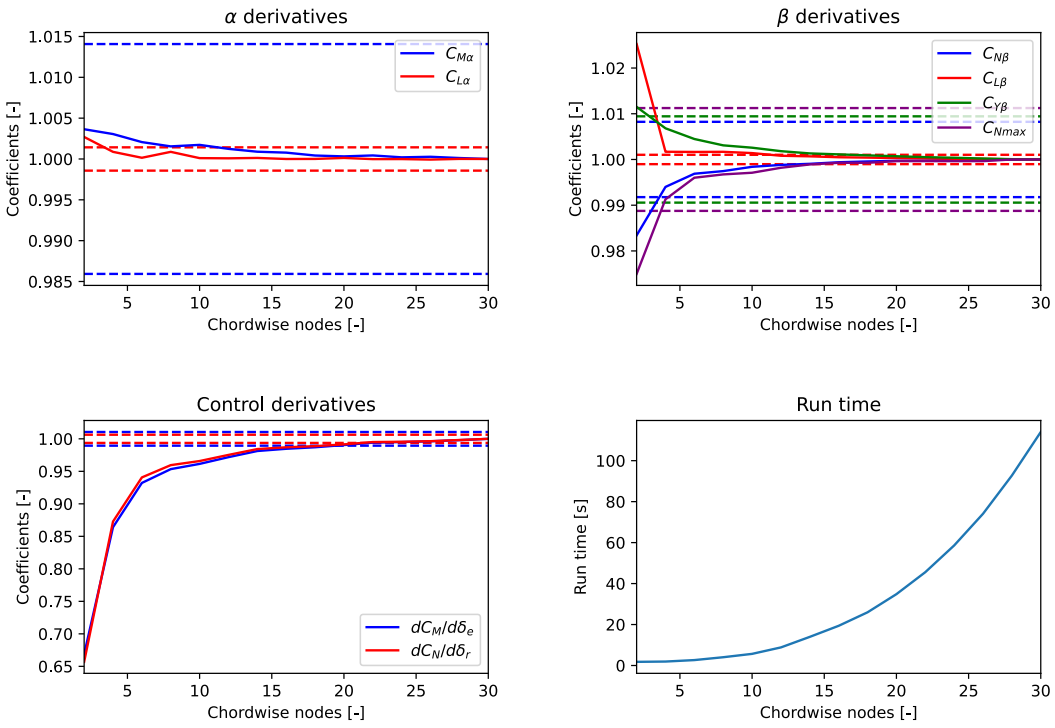

(a) Mesh convergence in chordwise direction with 30 nodes in spanwise direction on every wing element.

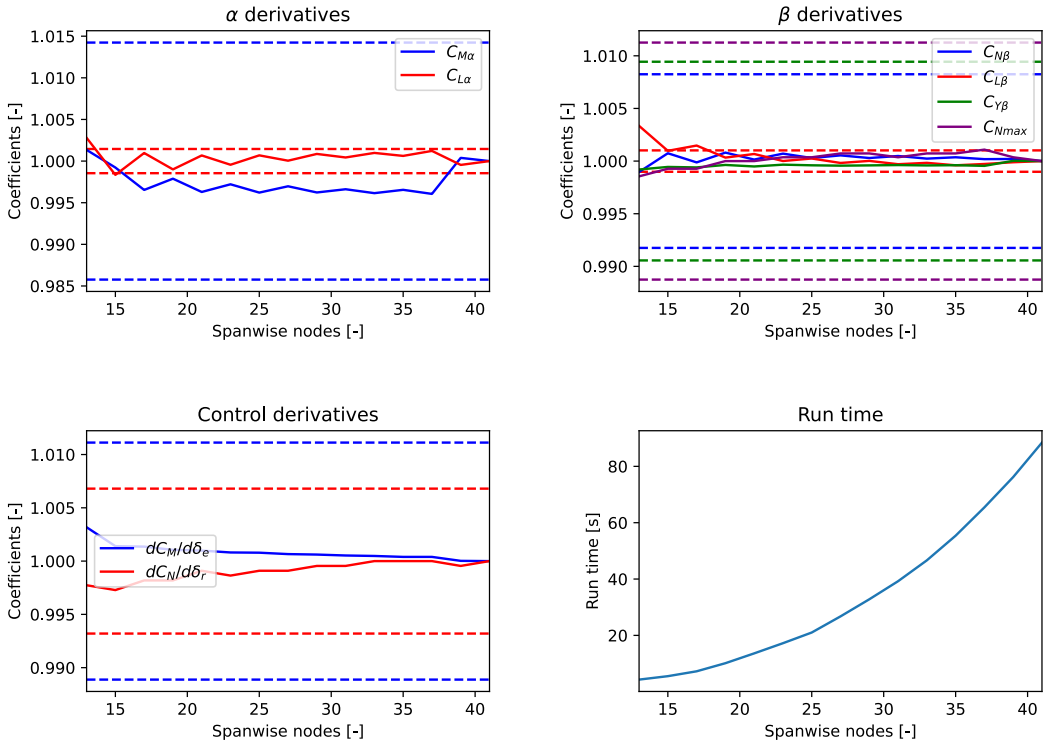

(b) Mesh convergence in spanwise direction with 20 nodes in chordwise direction on every wing element.

Figure 4.30: Stability and control mesh convergence. Dashed lines represent the effect of changing empennage or control surface area size by 1%, evaluated with the highest-resolved mesh resolution.

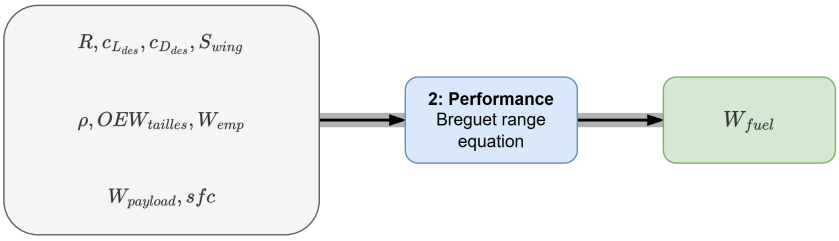

Figure 4.31: Input and output of the performance discipline.

$$W_{fuel} = \frac{W_i - W_f}{g} \tag{4.42}$$

The performance discipline inputs can be divided into two categories: parameters that are constant throughout the optimization and outputs of other disciplines. The values of some of these parameters depend on the aircraft version at hand and are given in Appendix A. The air density, ρ, is taken at cruise altitude for the performance calculations.

The specific fuel consumption depends on the propulsion system. The values for each propulsion system in the APPU project are presented in Table A.5. The APPU version contains two separate propulsion systems, the main engines and the APPU propulsor, and thus has two specific fuel consumption values. As explained in subsection 4.2.6, the final specific fuel consumption is the weighted average between the two based on the thrust fraction delivered by the APPU propulsor.

$c_{L_{des}}$ and $c_{D_{des}}$ are outputs of the aerodynamics discipline, while the empennage weight, W_{emp}, is obtained from the weight discipline described in subsection 3.2.1.

4.8. Constraints

Constraints are used to guarantee that the empennage performs its main functions. As discussed in subsection 3.2.3, this includes three functions: providing longitudinal and directional trim, stability, and control. Stability can be divided into two separate categories: static and dynamic stability. Calculating all the parameters required for the dynamic stability constraints that have been presented in subsection 3.2.3 is rather computationally expensive. Therefore, it is decided in subsection 3.2.3 to focus solely on static stability.

The remaining constraints for static stability and control are gathered in four separate sets. These include longitudinal static stability, lateral directional static stability, trim, and control. The set of constraints for longitudinal static stability is shown in Equation 4.43 [24, 28]. As discussed in subsection 3.2.3, the main requirement for longitudinal static stability is a negative pitching moment slope with respect to the angle of attack. In addition, the static margin should be within a certain domain to guarantee both enough longitudinal static stability and maneuverability.

$$C_1 = C_{m_\alpha} < 0 \tag{4.43a}$$

$$C_2 = S.M. < 0.1 \tag{4.43b}$$

$$C_3 = S.M. > 0.05 \tag{4.43c}$$

Note that the requirement on the static margin is split into two separate inequality constraints. This is because inequality constraints are considered active by optimization algorithms when their value is negative. Since the static margin must be within a range with minimum and maximum values, it must be separated into two inequality constraints. The set of constraints that guarantee lateral directional static stability can be seen in Equation 4.44 [24].

$$C_4 = C_{N_\beta} > 0 \tag{4.44a}$$

$$C_5 = C_{L_\beta} < 0 \tag{4.44b}$$

$$C_6 = C_{Y_\beta} < 0 \tag{4.44c}$$

As presented in section 4.5, the design point for the stability and control coefficients is at approach. That is, approach velocity, ground level atmospheric conditions, no fuel load, and full flaps extended. In order to achieve longitudinal trim, the design pitching moment coefficient should be zero and the design lift should be equal to the design weight of the aircraft during cruise. The design weight for these trim constraints is at half fuel load, as presented in Equation 4.20.

The set of constraints that guarantees trim can be seen in Equation 4.45 [4, 24, 25]. The requirements for lift equilibrium, as well as maintaining longitudinal and directional trim, are each translated into an equality constraint. For directional trim, it is important that the aircraft can be trimmed in case one of the engines fails, as discussed in subsection 3.2.3. As a result, there is a constraint that dictates that the maximum aerodynamic yawing moment at minimum dynamic pressure should be enough to counteract the yawing moment created by one engine. The A320neo family uses the LEAP-1A engines. It is used as the reference engine for the yawing moment, independent of the propulsion system of the case in this study. The LEAP-1A engine produces a maximum thrust of $35,000lbf$ or $155,688N$ per engine [52]. The engines on the A321neo are mounted at $5.73m$ from the center line [46]. This means that, at maximum thrust and one engine inoperative, a yawing moment, N_{engine}, of $892,092Nm$ is generated. Note that the design point for maximum yawing moment is different from the design point for the other trim constraints. The same approach conditions are applied for the maximum yawing moment as for the stability derivatives, but at a sideslip angle of 25 degrees, as mentioned in section 4.5.

$$C_7 = \frac{L_{des} - W_{des}}{L_{des}} = 0 \tag{4.45a}$$

$$C_8 = C_{M_{des}} = 0 \tag{4.45b}$$

$$C_9 = \frac{N_{max} - N_{engine}}{N_{max}} > 0 \tag{4.45c}$$

The control that the empennage provides over the aircraft can be measured as the elevator and rudder effectiveness. Minimum values that should be met by commercial aircraft have been presented in subsection 3.2.3. Like the stability derivatives, the control derivatives are calculated at approach conditions. This results in the final two design constraints that are shown in Equation 4.46 [32, 24]. Note that the units are changed from per radian to per degree.

$$C_{10} = C_{M_{\delta_e}} < -0.0035 \tag{4.46a}$$

$$C_{11} = C_{N_{\delta_r}} > 0.004 \tag{4.46b}$$

An additional constraint is introduced to control the absolute height of the HTP. The architecture is used to optimize multiple aircraft configurations to assess the impact of various design changes. One of these configurations excludes the use of a conventional empennage. This requirement is enforced by an inequality constraint, C_{HTP}, which ensures that the absolute height of the HTP exceeds a specified minimum. The constraint is defined in Equation 4.47, where Z_{HTP} represents the absolute height of the HTP and $Z_{HTP,min}$ denotes the minimum required height. Note that this constraint is not included in the design structure matrix of Figure 3.9 and 3.10, as only constraints related to trim, stability, and control are represented there.

$$C_{HTP} = \frac{Z_{HTP} - Z_{HTP,min}}{Z_{HTP,min}} \tag{4.47}$$

To prevent division by zero and ensure numerical stability, C_{HTP} is defined to return a value of 1 when Z_{HTP} equals zero, thereby satisfying the constraint by default in such edge cases.

Variable	Lower Bound	Initial Value	Upper Bound	Unit
HTP surface area	20	31	40	m^2
HTP aspect ratio	3	5	7.5	-
HTP taper ratio	0.25	0.388	0.7	-
HTP leading edge sweep angle	20	32	40	°
elevator hinge line	0	0.47	1	-
VTP surface area	10	21.5	30	m^2
VTP aspect ratio	1	1.755	2.5	-
VTP taper ratio	0.25	0.33	0.6	-
VTP leading edge sweep angle	25	40	50	°
rudder hinge line	0	0.303	1	-
HTP relative height	0	0	1	-
HTP relative set-back	0	0.3	1	-
HTP dihedral	-10	5	10	°

Table 4.6: Initial values and bounds for the planform design variables.

4.9. Initial Design & Bounds

The initial design for the optimization can have a big influence on the result with gradient-based optimization algorithms. Therefore, it is important to find a good initial design that preferably meets the constraints. The APPU project uses the A321neo as the baseline, so it makes sense to use it for the initial design as it is supposed to be close to the optimum and meet all the constraints. First, the design variables of the empennage planform and airfoils' initial values and bounds are discussed in subsection 4.9.1. Next, a small optimization study is performed to find the initial values for the HTP twist distribution in subsection 4.9.2. Finally, an additional friction drag coefficient parameter is calculated in subsection 4.9.3.

4.9.1. Empennage Planform & Airfoils

The initial values for the design variables are mainly based on the actual values for the empennage of the Airbus A320 family [46]. Some design variables' initial values are based on measurements done by hand on technical drawings since more accurate data have not been found. The lower and upper bounds of the design variables are determined based on an assessment of reasonable and practical constraints, informed by engineering judgment. The initial values and lower and upper bounds for these design variables can be found in Table 4.6.

Typically, symmetric airfoils are used for empennage designs. The initial values for the CST coefficients of all airfoils of the empennage are based on the NACA 0012 airfoil. In order to limit the airfoil design variables to shapes that are somewhat similar to a traditional airfoil but still offer freedom to the optimizer, the upper and lower bounds are set at 80% and 120% of the initial value, respectively.

4.9.2. HTP Twist Distribution

The remaining design variables control the twist distribution of the HTP. The twist is determined by two design variables: twist angle at the root and at the tip of the HTP. Between the root and the tip, the twist varies linearly. The initial value of the twist angles is found from a separate aerodynamic shape optimization study where the fuel and empennage weight remain constant. The only two design variables are the twist angles. The fuel weight is set at $16350kg$, which is the fuel left in the tank at the top of climb for the A321neo. The design point for the study is at half fuel load, so $8175kg$ is actually in the tank. The empennage weight is determined by the Raymer equations for the initial values of the remaining design variables. The objective of the optimization is the induced drag from AVL normalized with respect to the induced drag for the initial design. Both twist angles are zero for the initial design and can vary between -5 and 5 degrees. The main constraint that must be satisfied is C8, which states that the pitching moment at the design point must be zero.

The results of the optimization study can be seen in Figure 4.32. The final values for HTP root and tip twist are -1.48° and -0.48°, respectively. The pitching moment constraint is well converged; how-

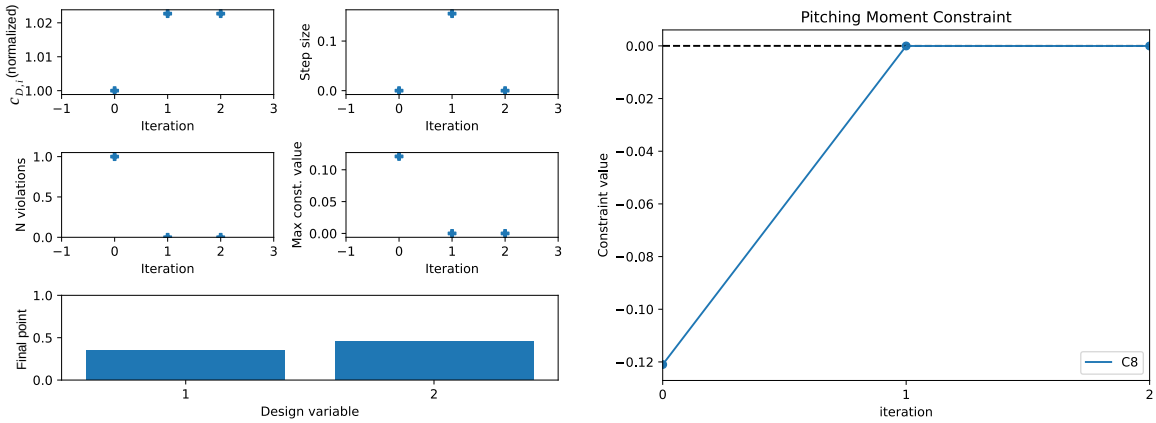

(a) Optimization summary.

(b) Equality constraints.

Figure 4.32: Aerodynamic optimization of the initial twist in the HTP. Empty bars in the bar graph mean that the variables are at the lower bound and a full bars mean that the variables are at the upper bound. Design variable 1 and 2 are the root and tip twist, respectively.

ever, the induced drag has to increase more than 2% compared to the initial design in order to meet this constraint. The reduced twist angles increase the downforce generated by the HTP, which needs to be made up for by an increase in lift from the main wing. Consequently, the induced drag increases as well. Additionally, all inequality constraints are met as well, which makes for a good starting point for the optimizations.

4.9.3. Friction Drag

AVL calculates only the induced drag and ignores other forms of drag. Therefore, a friction drag component is added to the induced drag to obtain the drag coefficient at the design point, as described in subsection 4.4.2. The value of the friction coefficient for this study is set such that the initial design for the A321neo case results in a required fuel load of $16350kg$ to cover the design range, which has been used for the baseline aircraft throughout the APPU project. The first step is to determine the total drag coefficient required to obtain this fuel load. Therefore, the Breguet equation is reordered to the form shown in Equation 4.48. The design lift coefficient is determined by the $8175kg$ fuel load at the design point. The initial weight is the weight at top of climb, including $16350kg$ of fuel, and the final weight is at approach, excluding fuel. All weights and the specific fuel consumption are expressed in Newtons. The values of the remaining parameters are explained in section 4.7.

$$C_{D_{des}} = 2\sqrt{\frac{2C_{L_{des}}}{\rho S_{wing}}}\frac{\sqrt{W_i} - \sqrt{W_f}}{sfc \times R} \tag{4.48}$$

The required total drag coefficient, $C_{D_{des}}$, to obtain the target fuel load is 0.02402. The induced drag coefficient, c_{D_i}, for the initial design is 0.01399. The friction drag coefficient, C_{D_f}, is found by subtracting the induced drag coefficient from the design drag coefficients, or 0.01003. The wetted surface area is dependent on the empennage design, as it is found from the total surface area of the faces that make up the aircraft compound described in subsection 4.2.6. The reference area of the wing is constant at $122.4m^2$. The friction coefficient for the initial design is found to be 0.001516 and remains fixed at this value throughout the optimization process.

5
Results

The method outlined in chapter 3 and chapter 4 is applied to optimize four distinct configurations, aimed at addressing the research questions. The resulting empennage designs for these configurations are presented in section 5.1. Subsequently, a comparative analysis of the optimized designs is conducted in section 5.2 to extract meaningful insights, followed by a discussion in section 5.3. Finally, a series of validation studies is included in section 5.4 to assess the reliability of different components of the methodology.

5.1. Configurations

A total of four different aircraft configurations are created to answer the research questions: the optimized A321neo, APPU propulsion, APPU wing and propulsion, and APPU configuration. Three inputs for the aircraft geometry distinguish these configurations: propulsion system, wing position, and empennage position. An overview of the selected options for each configuration can be seen in Table 5.1.

The selection of the propulsion system influences the OEW, the center of gravity, and the specific fuel consumption of the aircraft. Two different propulsion systems are used in these aircraft configurations: the standard propulsion system of the A321neo with the LEAP-1A engines and the hybrid APPU system. The APPU system increases the mass of the aircraft and shifts the center of gravity back, but decreases the specific fuel consumption. The wing position can be set either at the standard A321neo wing position or at the APPU wing position, which is shifted back 1.2 meters to cope with the shift in center of gravity. The empennage is either positioned like the empennage on the A321neo or according to the APPU requirements. In the case of the A321neo positioning, the empennage is positioned such that the trailing edge of the VTP, or the HTP in the case of a conventional tail, is located at a fixed distance from the fuselage tail. The APPU aircraft requires that no part of the fuselage intersects with the propulsor plane. In the case of the APPU positioning, the most aft point of the empennage lines up with the propulsor plane. When the APPU positioning is selected for the empennage, a non-zero minimum empennage is selected in C_{HTP} such that no structural elements of the HTP intersect with the hydrogen tank.

The optimized A321neo configuration aims to find an empennage design that is tailor-made for the A321neo, instead of for an entire aircraft family. The APPU propulsion configuration is used to investigate the effect of the added weight on the empennage due to the addition of the APPU propulsion

Variable	A321 Opt	APPU P	APPU W&P	APPU
Propulsion system	A321neo	APPU	APPU	APPU
Wing position	A321neo	A321neo	APPU	APPU
Empennage position	A321neo	A321neo	A321neo	APPU

Table 5.1: Overview of the different configurations that are analyzed.

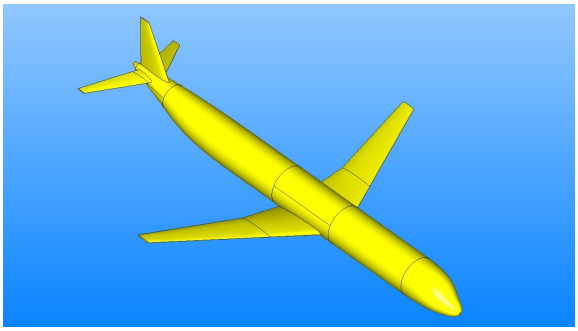

(a) Optimized A321neo.

(b) APPU propulsion.

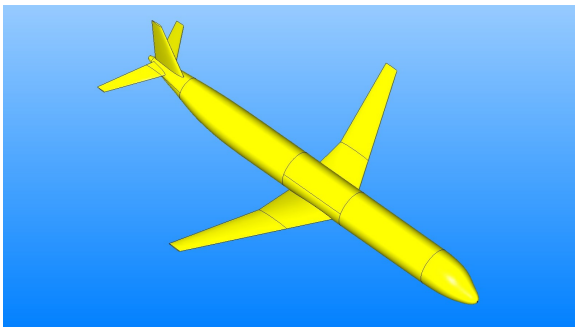

(c) APPU wing and propulsion.

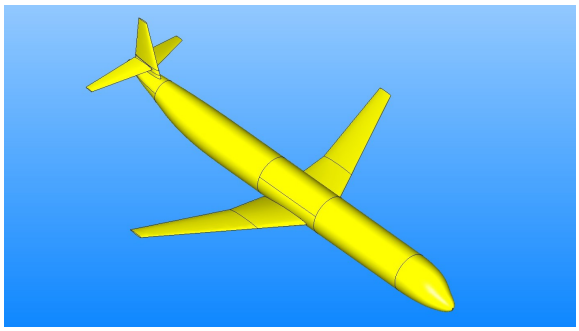

(d) APPU.

Figure 5.1: Overview of the final geometry for each optimized configuration.

system. The APPU wing and propulsion configuration is used to inspect the effect of the wing repositioning on the empennage. The optimal empennage design for the APPU aircraft is found from the APPU configuration.

5.2. Comparison

A visual representation of the final design for each configuration is given in Figure 5.1. All of the design variables, except the CST coefficients, can be seen in Table 5.2. For each design variable, the variable index, initial value, and final value for each of the configurations presented in Table 5.1 are given. The same information for all of the CST coefficients is given in Table C.1. The convergence history, as well as some more views of the optimized empennage geometry, are provided in Appendix D for each of the aircraft configurations.

5.2.1. Surface Area

The surface area of the horizontal tailplane is reduced to the lower bound at $20m^2$ for all of the configurations except the APPU wing and propulsion configuration, where the final value is slightly above the lower bound at $20.415m^2$. It is typically not desirable to have final values for design variables close to their bounds. However, the lower bound for the surface areas is set with the use of AVL in mind. AVL assumes lift increases linearly with angle of attack and does not model stall. In addition, it considers only induced drag. Therefore, AVL could predict small wings at very high angles of attack that produce equal amounts of lift at similar aerodynamic efficiency levels as normal-sized wings at moderate angles of attack. To avoid this scenario, the lower bound for the HTP surface area is set at $20m^2$.

A similar reduction is visible for the surface areas of the vertical tailplanes. The VTP surface area is significantly reduced for all configurations; however, not all the way to the lower bound. Note that the optimized surface area of the VTP for the APPU propulsion configuration is approximately $3m^2$ larger than the optimized VTP surface areas for the other configurations. This is due to the additional weight of the APPU system that is installed in this configuration compared to the optimized A321neo configuration. This additional weight is positioned at the rear of the fuselage, causing the center of gravity

Nr.	Variable	Initial	A321 Opt	APPU P	APPU W&P	APPU	Unit
1	HTP area	31.000	20.000	20.000	20.415	20.000	m^2
2	HTP aspect ratio	5.000	7.380	5.170	7.500	7.500	-
3	HTP taper ratio	0.388	0.372	0.367	0.419	0.349	-
4	HTP LE sweep	32.0	33.5	30.4	33.0	20.0	°
5	VTP area	21.500	14.220	17.841	14.978	13.974	m^2
6	VTP aspect ratio	1.755	2.008	1.881	2.046	2.362	-
7	VTP taper ratio	0.330	0.288	0.300	0.323	0.295	-
8	VTP LE sweep	40.0	33.4	33.9	33.6	25.0	°
25	Root twist	-1.476	-2.149	-1.260	-2.744	-2.177	°
26	Tip twist	-0.480	-0.214	0.635	-0.542	-1.840	°
27	Elevator hinge line	0.470	0.393	0.458	0.448	0.420	-
28	Rudder hinge line	0.303	0.327	0.299	0.380	0.358	-
29	HTP height	0.000	0.000	0.000	0.000	0.174	-
30	HTP set-back	0.300	0.292	0.197	0.387	0.217	-
31	Dihedral	5.0	-10.0	-1.633	-10.0	-10.0	°

Table 5.2: Initial and final values of the design variables for all configurations.

to shift aft. This results in a decreased moment arm from the vertical tailplane to the center of gravity. In addition, the main wing is positioned farther forward relative to the center of gravity for the APPU propulsion configuration because the main wing is not repositioned. This increases the yaw instability. To cope with this increased yaw instability with a reduced moment arm, the VTP surface area must be increased. Shifting the main wing aft 1.2m, as is done for the APPU wing and propulsion, and the APPU configuration, has a stabilizing effect on the yaw instability. Consequently, the surface area of the vertical tailplane can be reduced again.

For the optimized A321neo configuration, a surface area of 20m^2 and 14.22m^2 are found for the horizontal and vertical tailplane, respectively. This corresponds to a reduction of 35.5% and 33.9% in surface area for the HTP and VTP, respectively. This supports the findings of Morris [6], who also found that the empennage surface area of a larger aircraft within a family could be reduced significantly without losing stability.

5.2.2. Twist Distribution

It can be seen in Table 5.2 that the twist at the root of the HTP is more negative than the twist at the tip for each configuration. This helps create a more elliptical lift distribution, thus reducing the induced drag. Furthermore, it can be seen from the twist angles that the shift in center of gravity due to the additional weight of the APPU system reduces the required downforce generated by the HTP. The aircraft's center of gravity is in front of the aerodynamic center of the main wing. When the center of gravity shifts aft, the distance to the main wing's aerodynamic center is reduced, resulting in a reduced nose-down pitching moment. Less downforce is required from the HTP to counter the nose-down pitching moment, leading to less negative twist angles for the APPU propulsion configuration. There is even positive twist at the root of the horizontal tailplane. Shifting the main wing aft 1.2m reverses this effect, increasing the required downforce level from the HTP. Due to a reduction in the moment arm of the HTP, the required downforce level from the HTP for the APPU wing and propulsion, and APPU configuration is slightly higher compared to the optimized A321neo configuration. Therefore, slightly more negative twist is required in the HTP for these two configurations.

5.2.3. Empennage Configuration

From the HTP height in Table 5.2, it is apparent that the optimizer aims to position the HTP as low as possible. The HTP height is zero for all optimized configuration configurations except for the APPU configuration. A HTP height of zero corresponds to a conventional tail. This is not allowed for the APPU configuration since this would mean that structural elements of the HTP would intersect the hydrogen tank. Therefore, a minimum height of 1m was set through the C_{HTP} constraint. The optimizer

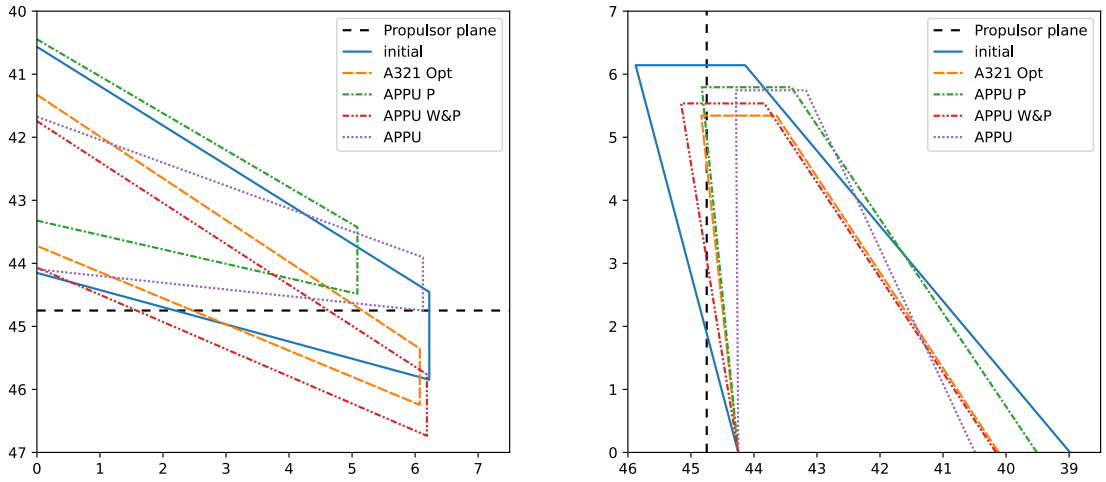

(a) HTP planforms.

(b) VTP planforms.

Figure 5.2: Overlay of the empennage planforms of the final design for every optimized configuration and the initial design.

positions the HTP so that this constraint is just met for the APPU configuration, indicating that the optimizer still tries to position the horizontal tailplane as low as possible or allowed. Therefore, a low cruciform empennage is found to be optimal for the APPU configuration. The preference to position the HTP as low as possible is also visible in the HTP dihedral for all optimized configurations, except the APPU propulsion configuration. The dihedral for the other configurations is at the lower bound of -10°. By introducing negative dihedral, or anhedral, the overall height of the horizontal tailplane is further reduced. A more in-depth discussion on the HTP height is provided in subsection 5.3.4.

5.2.4. Planforms

Figure 5.2 shows the optimized planforms of both the horizontal and vertical tailplanes drawn on top of the initial design. It is visible that the optimized planforms vary strongly from the initial design in some aspects. There are also some clear differences between the different optimized configurations. All of the optimized HTP platforms, except for the APPU propulsion configuration, have high aspect ratios. From Table 5.2 it can be seen that the HTP aspect ratio is even all the way at the upper bound for some configurations. This indicates that model prefers aerodynamic efficiency over structural weight. The low aspect ratio observed for the APPU propulsion configuration may be attributed to the reduced downforce generated by the HTP, which results from the more positive twist angles. Since the HTP produces less downforce, the reduction in fuel mass due to the increased aerodynamic efficiency is minimal compared to the other configurations. The increase in fuel mass due to the structural weight penalty that comes with high aspect ratios outweighs the reduction due to the increased aerodynamic efficiency. Therefore, the optimizer moves to a lower aspect ratio design for the APPU propulsion configuration. A similar trend is visible for the vertical tailplanes, but less pronounced. All configurations, except the APPU propulsion configuration, move to higher aspect ratios for the VTP compared to the initial design. The VTP aspect ratio for the APPU propulsion configuration is slightly higher than the initial design aspect ratio, but not much. The difference in VTP aspect ratio cannot be explained by a difference in downforce levels. However, a possible explanation is that the structural weight penalty becomes too large due to the increased VTP surface area for the APPU propulsion configuration compared to the other optimized designs.

Another disadvantage of high aspect ratio wings, other than the structural weight penalty, is that they suffer more from friction drag in reality. The increased aspect ratio decreases the mean aerodynamic chord of the wing element. This in turn, reduces the Reynolds number and lower Reynolds numbers correspond to higher friction drag coefficients. This effect is ignored in the friction drag model that is applied in this study. Therefore, it is decided to validate the drag model by investigating the effect of the aspect ratio on the required fuel load while comparing the current drag model with a flat plate friction drag model. The flat plate drag model does take the Reynolds number into account. This validation

study and its results are presented in subsection 5.4.1.

The optimal leading edge sweep angle for the horizontal tailplane does not appear to vary much from the initial sweep angle for most configurations in Figure 5.2a. Only the heavily reduced leading edge sweep angle for the APPU configuration's horizontal tailplane seems to be drastically different from the initial design. The values for the leading edge sweep angles can also be seen in Table 5.2. For the APPU configuration, the HTP sweep is reduced to the lower bound of 20°. Such low sweep angles are atypical for transonic aircraft. Normally, the position of the HTP root is fixed on the tail cone. As a result, introducing sweep into the horizontal tailplane generally shifts its aerodynamic center aft. For the APPU configuration, the empennage is positioned such that the trailing edge at the tip of the HTP lines up with the propulsor plane. Since the location of the tip is constrained, reducing the sweep angles shifts the root and aerodynamic center of the HTP aft. This increases the tail volume coefficient in turn. One can see in Figure 5.2a that the trailing edge of the HTP tip for the APPU configuration indeed lines up perfectly with the propulsor plane. This indicates that the HTP is positioned as far aft as possible without intersecting the propulsor plane, which is only a requirement for the APPU configuration. The moderate sweep angle for the other configurations could be the optimizer balancing placing the aerodynamic center aft and reducing structural weight.

The leading edge sweep angle of the vertical tailplane appears to be slightly reduced for most optimized configurations in Figure 5.2b. It can be seen in Table 5.2 that the VTP leading edge sweep angle is reduced from 40° to approximately 33° to 34° for all configurations, except the APPU configuration. This change in sweep angle could be the optimizer balancing the structural benefit of low sweep with the benefit of positioning the VTP aerodynamic center further aft by increasing sweep. Similarly to the HTP sweep angle, the VTP sweep angle for the APPU configuration is reduced to the lower bound, which is 25° for the VTP. This heavy reduction can be explained by the same reasoning as for the HTP sweep reduction for the APPU configuration. However, the VTP trailing edge does not line up perfectly with the propulsor plane. This could be either because the optimizer prefers to have the HTP and VTP staggered, or because the optimizer did not find this optimum within the termination criteria. The results for the APPU configuration should be treated with caution, as the sweep at the leading edge is below the 29° critical sweep angle found in subsection 4.4.2. With a taper ratio lower than 1, this means that the quarter-chord sweep angle is below the critical sweep angle as well. Therefore, transonic flow is likely to occur at the given sweep angles. Additionally, wings with less sweep are more prone to stall, which can be critical for the empennage.

5.2.5. Airfoils

Apart from optimizing the planforms of the horizontal and vertical tailplane, the goal of this study is to optimize the empennage airfoils as well. However, it is not possible to optimize the airfoils of the vertical tailplane with this architecture. AVL is used for the aerodynamic analysis, which neglects the airfoil thickness and only models the camber line. The vertical tailplane always consists of symmetric airfoils which have a straight camber line. Therefore, the optimizer was only given the freedom to adapt the root and tip airfoils of the HTP.

Figure 5.3 shows the camber lines of the optimized airfoils both at the root and at the tip of the horizontal tailplane drawn on top of the initial design camber lines. The amount of camber is in the range of 0.1%, which is very little. Therefore, it is possible that these airfoil geometries and camber lines are the results of random movement of the optimizer around the initial point instead of a true optimum found by the optimizer. The initial design has NACA0012 symmetric airfoils at both the root and tip of the horizontal tailplane. As a result, the camber lines for the initial design are straight. The camber lines for the optimized configurations have more negative camber, or less positive camber, at the root compared to the tip of the horizontal tailplane. This could help with a better spanwise lift distribution, but is more likely due to random movement of the optimizer around the initial point. The final values for the HTP CST coefficient and airfoil geometries for each configuration are presented in Appendix C. Note that the optimizer does not move to thicker airfoils for the HTP. This is because the Raymer equations consider only the thickness of the VTP. The thickness of the HTP has no influence on the empennage weight. Therefore, there is no benefit for the optimizer to increase the HTP thickness.

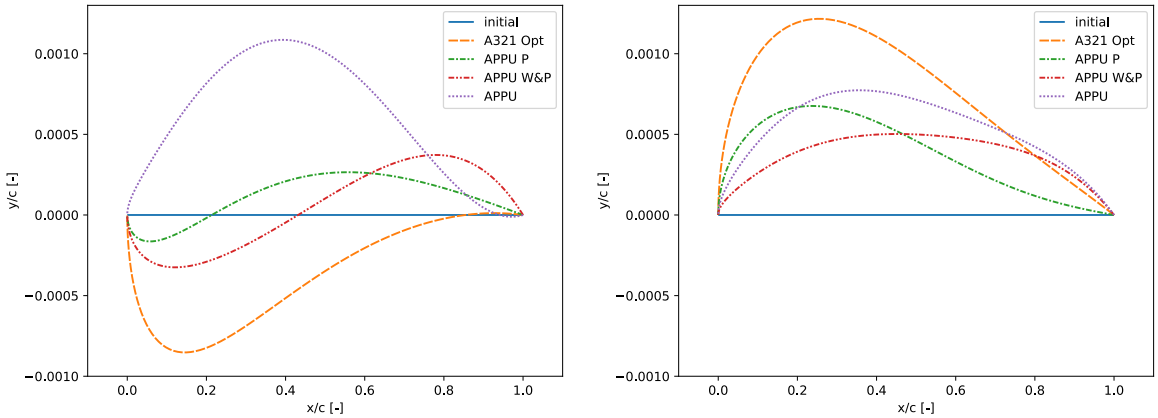

(a) HTP root.

(b) HTP tip.

Figure 5.3: Overlay of the horizontal tailplane camber lines of the final design for every optimized configuration and the initial design.

Output	Initial	A321 Opt	APPU P	APPU W&P	APPU	Threshold	Unit
W_{fuel}	16,350	15,800	12,890	12,950	13,080	-	kg
W_{emp}	1,364	1,075	1,070	1,130	1,050	-	kg
$C_{L_{des}}$	0.600	0.596	0.604	0.605	0.605	-	-
$C_{D_{des}}$	0.0240	0.0232	0.0236	0.0237	0.0239	-	-
$C_{M_{des}}$	0.000	0.000	0.001	0.000	0.000	$= 0$	-
C_{M_α}	-0.0879	-0.0677	-0.0488	-0.0697	-0.0709	< 0	1/°
C_{L_α}	0.0891	0.0852	0.0841	0.0847	0.0853	-	1/°
$S.M.$	0.987	0.795	0.580	0.822	0.831	$[0.05, 0.1]$	-
C_{N_β}	0.00485	0.00422	0.00440	0.00434	0.00434	> 0	1/°
C_{L_β}	-0.00435	-0.00405	-0.00437	-0.00417	-0.00422	< 0	1/°
C_{Y_β}	-0.00702	-0.00604	-0.00652	-0.00634	-0.00642	< 0	1/°
$C_{N_{max}}$	0.647	0.542	0.553	0.550	0.550	≥ 0.550	-
$C_{M_{\delta_e}}$	-0.0589	-0.0457	-0.0425	-0.0476	-0.0513	≤ -0.0035	1/°
$C_{N_{\delta_r}}$	0.0221	0.0186	0.0205	0.0190	0.0205	≥ 0.004	1/°
α_{cruise}	1.7	1.7	1.6	1.9	1.8	-	°
$\alpha_{approach}$	11.7	12.0	12.7	12.9	12.8	-	°

Table 5.3: Disciplinary outputs for initial design and all configurations. The threshold indicates the target range to satisfy the trim, stability, and control constraints.

5.2.6. Disciplinary Outputs

The results of each discipline for the initial design and the final design of each configuration can be seen in Table 5.3. Each optimized configuration has an additional element from the APPU aircraft compared to the baseline. The first configuration is the optimized A321neo. The APPU propulsion differs by the inclusion of the APPU propulsion system, resulting in a higher mass, shift in center of gravity, and lower specific fuel consumption. The APPU wing and propulsion configuration implements the main wing relocation to account for the shift in center of gravity. The APPU configuration adds the geometrical constraints on the empennage.

The fuel weight is reduced for each configuration compared to the initial design. However, there is a big drop between the optimized A321neo and APPU propulsion configuration. This is due to the addition of the APPU system, which has a lower specific fuel consumption compared to the main engines. This results in lower fuel consumption to cover the design range. The increase in fuel weight between the different configurations that use the APPU system can be attributed to a decrease in aerodynamic efficiency. This is the increased downforce level on the HTP for the APPU wing and propulsion configuration, and the less optimal empennage configuration and sweep angles for the APPU configuration.

Due to the size reduction of the optimized empennages, the empennage weight is significantly reduced compared to the initial design. Two things are noteworthy. First, the empennage for the APPU propulsion configuration is lighter than the empennage for the optimized A321neo and APPU wing and propulsion configuration despite its larger size due to the increased VTP surface area. This may result from its moderate aspect ratio compared to the high aspect ratio of the other two configurations. High aspect ratio wings are slender and their structures are heavier. Secondly, the APPU configuration has the lightest empennage of all the configurations despite its cruciform tail configuration, which is typically heavier than conventional tails. This is due to its low sweep angles since adding sweep increases the structural weight of wing elements.

It can be seen that the design lift coefficients for the optimized configurations are close to the design lift coefficient of 0.600 for the initial design. However, the lift coefficient for the optimized A321neo configuration is slightly below the initial design lift coefficient. This reduction is due to the reduction in fuel weight, which also decreases the aircraft weight at the design point. The lift coefficients for the configurations with the APPU propulsion system are slightly above the initial value. Their lower fuel mass is countered by the added mass of the APPU engine and tank, resulting in a heavier aircraft.

From the design pitching moment, it can be seen that the aircraft is very well trimmed at the design point. The maximum pitching moment coefficient for a configuration is 0.001. This is so small that it is negligible. The static margin is outside the optimal range for all optimized configurations, which is between 0.05 and 0.1 [28]. Constraint C_2 states that the static margin should be less than 0.1. The constraint is deactivated for the optimization process. Higher static margins correspond to higher stability. The optimizer has not been able to meet this constraint within the design space. This is also the case for the initial design. It is decided to omit C_2 for all configurations, to avoid penalizing the optimized designs because the initial design is too stable. When C_2 is included, the optimizer focuses solely on trying to get the constraint deactivated and gives up on minimizing the objective. However, reducing the HTP surface area has a positive effect on C_2. As a result, the optimized designs are closer to the optimal range compared to the initial design. This supports the decision to remove constraint C_2. A deeper discussion into the accuracy of these predictions for the static margin is presented in subsection 5.3.5. All other stability and control derivatives are within the desirable domain for the initial design and all of the optimized configurations. It is worth noting that the final design for the APPU propulsion configuration is found to be stable despite the backward shift in the center of gravity without the repositioning of the wing. A more in-depth discussion on this is provided in subsection 5.3.3.

5.3. Discussion

This section presents an in-depth discussion of several key findings that contribute to answering some of the research questions. Furthermore, it elaborates on specific aspects of the results that merit additional clarification or contextual explanation, offering a broader perspective on the implications and limitations of the study.

5.3.1. APPU System Effect on Empennage Design

The primary objective of this study is to address the central research question: ”Which implications does the inclusion of an APPU system have on the optimal empennage design for a commercial aircraft?” To evaluate the impact of the APPU system on empennage optimization, the empennage design of the optimized A321neo and APPU configurations are compared. Both optimized empennage designs share certain characteristics, such as high aspect ratios and significantly reduced surface areas for both the horizontal and vertical tailplanes compared to the baseline. However, notable differences also emerge. For the APPU-equipped configuration, reduced sweep angles in the empennage are advantageous, as they shift the aerodynamic center aft as much as possible without the empennage intersecting the propulsor plane. Additionally, the HTP must be elevated for aircraft equipped with an APPU system to prevent structural interference with the hydrogen tank. From the perspective of HTP positioning, a low cruciform empennage is preferable over mid or high cruciform and T-tail empennage configurations to position the HTP as low as possible.

The impact of the additional weight introduced by the APPU system is assessed by comparing the empennage designs for the APPU propulsion and optimized A321neo configurations. The APPU-equipped configuration is heavier, exhibits a more aft center of gravity, and achieves a lower specific fuel flow compared to the optimized A321neo, due to the integration of the APPU propulsion system. As discussed in subsection 5.2.4, the aft center of gravity shift reduces the pitching moment generated by the main wing, thereby decreasing the downforce required from the horizontal tailplane to trim the aircraft. Consequently, the HTP in the APPU propulsion configuration exhibits a more positive twist distribution relative to that of the optimized A321neo configuration. An additional effect of the reduced downforce level is the optimizer's preference for structural efficiency over aerodynamic efficiency, resulting in a more moderate aspect ratio. Furthermore, the aft center of gravity results in increased yaw instability, necessitating a larger VTP surface area to ensure stability and enable trimming in the event of an engine failure. The effect of repositioning the main wing can be seen by comparing the APPU wing and propulsion configuration. Repositioning the main wing 1.2 meters aft counteracts these aforementioned effects, leading to more negative twist angles in the HTP and a reduction in the required VTP surface area.

To investigate the influence of the hydrogen tank and propulsor location on the optimal empennage design, a comparison is made between the APPU wing and propulsion configuration and the full APPU configuration. The only difference between these two configurations lies in the geometrical constraints imposed on the empennage in the latter. Specifically, the empennage must not intersect the propulsor plane, and the horizontal tailplane must avoid structural interference with the hydrogen tank. When the empennage is constrained at the rear, as in the APPU configuration with a propeller, reducing the sweep angles proves beneficial, as it shifts the aerodynamic center of the empennage as far aft as possible. A more detailed explanation of this effect is provided in subsection 5.2.4. Furthermore, if the HTP must be raised to avoid interference with components such as a hydrogen tank located in the tail cone, a low cruciform tail is preferred, as it allows the HTP to be positioned as low as possible while still meeting structural and spatial constraints.

5.3.2. Airfoil Optimization

The investigation into optimal airfoil geometries for the horizontal and vertical tailplanes yielded limited results. Firstly, optimizing the VTP airfoils using AVL is not feasible, as the solver only models the camber line and neglects airfoil thickness. Consequently, optimizing symmetric VTP airfoils, which inherently have straight camber lines, is ineffective. Similarly, the optimization of HTP airfoils was unsuccessful. The resulting airfoil shapes closely resemble the initial design, with minor variations likely attributable to random perturbations rather than genuine optimization, as discussed in subsection 5.2.5. A potential explanation lies in the airfoil parameterization method: each airfoil is defined by separate sets of CST coefficients for the upper and lower surfaces, resulting in a dual-parameter definition of the camber line. This may interfere with the optimizer's gradient-based search process. Therefore, further research is required, ideally employing solvers that account for airfoil thickness to enable more accurate and meaningful airfoil optimization for empennage design. Such solvers could be panel methods or hybrid approaches combining VLM with airfoil design tools like XFOIL.

5.3.3. Main Wing Repositioning

According to estimates from the APPU project, the main wing needs to be shifted aft by 1.2m to achieve stability due to the rearward shift in the center of gravity. This study found that the APPU propulsion configuration, featuring the shifted center of gravity but without repositioning the main wing, is stable. However, it is premature to conclude that repositioning the main wing is unnecessary. Stability derivatives in this study are only evaluated at approach conditions. A comprehensive stability assessment across the entire flight envelope would be required to draw definitive conclusions. Furthermore, an aerodynamic analysis method with a higher fidelity level, particularly one that captures transonic effects more accurately, is necessary to improve confidence in the stability predictions.

5.3.4. HTP height

All of the optimized configurations have the HTP positioned as low as allowed. This results in a reduction of the structural weight of the VTP and a reduction in fuel weight as a consequence. However, it appears that AVL prefers to have the HTP positioned as low as possible from the reduction in dihe-

dral for all configurations. The dihedral is at the lower bound for all configurations, except the APPU propulsion configuration, which is coincidentally the configuration where the HTP produces the least downforce.

In addition, despite having the lowest empennage weight, the APPU configuration does not have the lowest fuel weight. This indicates that it suffers from reduced aerodynamic efficiency compared to the other configurations with the APPU propulsion system. This is further supported when looking at the design drag coefficient in Table 5.3. The design drag coefficient is increased by 2 to 3 drag counts compared to the other configurations equipped with the APPU propulsion system. The relative changes in lift coefficient are much smaller. This indicates again that positioning the optimizer as low as possible is beneficial according to AVL. It is unclear at the moment why AVL appears to prefer this positioning, as the HTP typically operates better further away from the main wing downwash. Therefore, more research is needed into this effect.

5.3.5. Static Margin

The predictions for the static margin are more likely a systematic error than close estimates for the static margin of the aircraft in reality. Three potential sources for this error are identified. First, there could be a constant error in AVL's low-fidelity method. One possible explanation is the reduced tail effectiveness due to the presence of shocks in reality [53]. Second, Equation 3.11 states that the static margin should be evaluated at the most aft center of gravity. The static margin is evaluated at approach in this study, meaning that there is no fuel onboard. Adding fuel shifts the center of gravity aft, therefore decreasing the static margin. Finally, discrepancies between the AVL results and reality may arise from inaccuracies in the modeled wing geometry. As detailed information on the airfoil profiles for the A321neo is not publicly available, the wing model is based on estimates for the geometry. Therefore, the neutral point can deviate from reality. The observed error is likely a combination of these three factors. More research is necessary to be able to say how much each of these factors contributes to the final error.

5.4. Validation

Two separate validation studies are conducted to assess key aspects of the optimization process. First, the constant friction coefficient drag model is evaluated by comparing it to a more accurate flat plate drag model across a range of empennage aspect ratios. Second, the vortex lattice method implemented in AVL is validated against FlightStream's panel method, which incorporates a transonic compressibility model.

5.4.1. Aspect Ratio & Drag Model

As discussed in subsection 5.2.4, a validation study is necessary to assess the accuracy of the current drag model, which assumes a constant friction coefficient. This model is compared to a flat plate drag model that accounts for the increase in friction coefficient with rising aspect ratio. Both models are evaluated across a range of aspect ratios for the horizontal tailplane (HTP) and vertical tailplane (VTP) to examine their influence on the optimizer's gradient search behavior.

Flat Plate Drag Model

The flat plate drag model decomposes the total drag at the design point into three components, as shown in Equation 5.1. In this formulation, D_{des} represents the total design drag force, $D_{i,des}$ the total induced drag force at the design point, $D_{f_{emp}}$ the total friction drag on the empennage, and $D_{f_{a/c}}$ the friction drag on the remainder of the aircraft. The term $D_{f_{a/c}}$ encompasses friction drag from all other components of the aircraft — including the main wing, fuselage, and engines — except the empennage. The induced drag coefficient is obtained from AVL within the aerodynamics discipline, and the total induced drag force is subsequently calculated using the standard drag equation presented in Equation 5.2.

$$D_{des} = D_{i,des} + D_{f_{emp}} + D_{f_{a/c}} \tag{5.1}$$

$$D_{i,des} = \frac{1}{2} c_{D_{i,des}} \rho_{cruise} V_{cruise}^2 S_{wing} \tag{5.2}$$

The empennage friction drag is decomposed into a component resulting from the HTP and a component resulting from the VTP. This distinction is necessary because the friction coefficient depends on the mean aerodynamic chord, which differs between the two tailplanes. However, the same method is applied to both and is therefore described only once here. To determine the total empennage friction drag, the friction drag contributions from each tailplane are summed. The friction drag force for each tailplane is calculated using Equation 5.3, where $D_{f_{TP}}$ and $S_{TP,wet}$ denote the friction drag and wetted area of the respective tailplane. The friction coefficient c_f is determined using flat plate theory for turbulent boundary layers. Çengel and Cimbala [54] provide an empirical correlation to estimate the friction coefficient for turbulent flow over a flat plate, as shown in Equation 5.4. In this equation, Re_{TP} represents the Reynolds number for the respective tailplane, computed using Equation 5.5, where $\mathrm{MAC_{TP}}$ is the mean aerodynamic chord and μ_{cruise} is the dynamic viscosity at cruise altitude.

$$D_{f_{TP}} = \frac{1}{2} c_f \rho_{cruise} V_{cruise}^2 S_{TP,wet} \tag{5.3}$$

$$c_f = \frac{0.074}{Re_{TP}^{1/5}} \tag{5.4}$$

$$Re_{TP} = \frac{\rho_{cruise} V_{cruise} \mathrm{MAC_{TP}}}{\mu_{cruise}} \tag{5.5}$$

The final component of the total drag force is the aircraft friction drag, $D_{f_{a/c}}$. This component is calibrated such that the initial design requires a fuel load of 16,350kg to meet the design range. This calibration approach mirrors the method used to set the constant friction coefficient value in the drag model applied during optimization. The required drag coefficient is determined using the Breguet range equation, based on the known lift coefficient, range, and fuel load of the initial design. The total design drag is then computed using the standard drag equation under cruise conditions. To obtain the calibrated value for $D_{f_{a/c}}$, the induced drag and empennage friction drag of the initial design are subtracted from the total design drag. This yields a calibrated aircraft friction drag of 10.6kN. For any new design, the variable induced drag and empennage friction drag are added to this constant aircraft friction drag to determine the total drag. The overall drag coefficient is then calculated using the standard drag equation, as shown in Equation 5.6.

$$c_{D_{des}} = \frac{2 D_{des}}{\rho_{cruise} V_{cruise}^2 S_{wing}} \tag{5.6}$$

Aspect Ratio Sweep

The flat plate drag model is compared to the constant friction coefficient model by analyzing the fuel load across a range of empennage aspect ratios. The results are presented in Figure 5.4. In the figure, solid lines represent the constant friction coefficient drag model, while dashed lines represent the flat plate drag model. The fuel weight is normalized for each configuration relative to the minimum fuel weight obtained for that configuration using the constant friction coefficient model. It is important to note that both the HTP aspect ratio (shown on the bottom axis) and the VTP aspect ratio (shown on the top axis) are varied simultaneously. The range for both aspect ratios extends from their respective initial values to the maximum optimized aspect ratio observed among all configurations.

From the results obtained using the constant friction coefficient drag model, it is observed that the APPU propulsion configuration exhibits a neutral gradient, whereas the other optimized configurations display a clear negative gradient. Since the SLSQP optimization algorithm follows descending gradients, it is consistent that the optimizer maintains a moderate aspect ratio for the APPU propulsion configuration, while favoring higher aspect ratio empennages for the other configurations. Furthermore, these findings support Airbus's selection of a moderate aspect ratio in the initial design, as it exhibits a similarly neutral gradient to that of the APPU propulsion configuration.

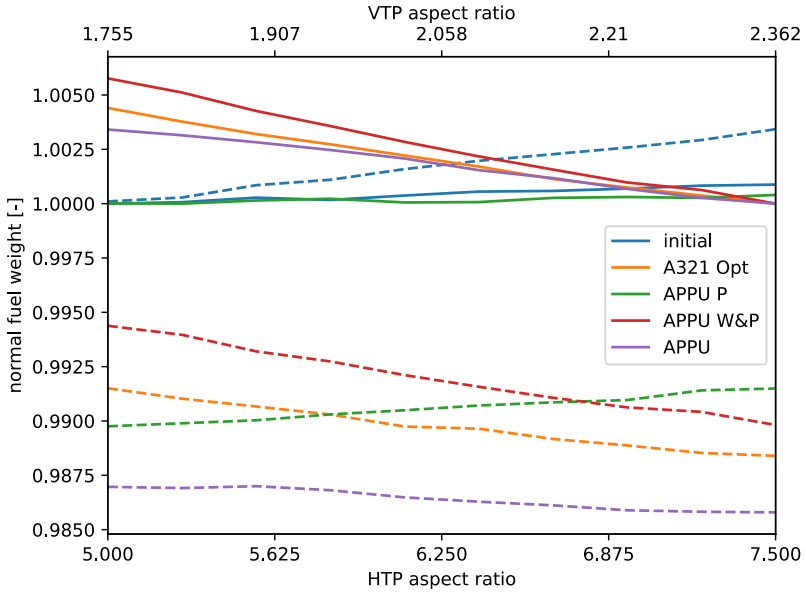

Figure 5.4: Effect of aspect ratio on the objective function for the constant friction coefficient drag model (solid) and the flat plate drag model (dashed).

The results from the theoretically more accurate flat plate drag model show lower fuel weights for the optimized configurations, which can be attributed to reduced friction drag. Since empennage friction drag is proportional to the wetted area, the significant reductions in surface area for both the horizontal and vertical tailplanes lead to a notable decrease in friction drag. In contrast, the initial design retains its original surface areas, which explains why both drag models yield the results for the initial configuration with its baseline aspect ratios. Despite the offset in absolute fuel load, the gradient trends are consistent with those observed in the constant friction coefficient model. All optimized configurations, except for the APPU propulsion configuration, exhibit negative gradients. The initial design and APPU propulsion configuration, however, show a positive gradient rather than the neutral gradient observed with the constant friction coefficient model. However, these positive gradients tend to flatten near the lower bounds of the analyzed domain, suggesting the presence of a local minimum just beyond the tested range. Consequently, this indicates that the resulting optimized configurations are likely to remain similar regardless of which drag model is employed.

5.4.2. Cruise Performance & Trim

In order to validate the flight characteristics at cruise, the AVL results for the final design of each configuration are compared with FlightStream simulations. In this case, the mesh is generated manually using the FlightStream graphical user interface, rather than automatically via ParaPy. The mesh used to validate the initial design is shown in Figure 5.5. This same mesh is applied to the main wing and fuselage for the validation of the optimized configurations. Corresponding meshes are generated for the optimized empennage geometries. These meshes are shown in Figure E.1 of Appendix E.

The same fluid properties used previously in the aerodynamics discipline, as described in subsection 4.4.1, are applied for the validation of cruise performance and trim. All other FlightStream settings remain consistent with those listed in Table 4.2, with two exceptions: the convergence limit is reduced to 10^{-6} to improve numerical accuracy, and the wake size is increased to the default value of 1000% in order to reduce computational run time. The angle of attack is set equal to the value obtained from AVL for each configuration to ensure comparability of results. A turbulent boundary layer and viscous coupling are once again enabled. Additionally, the transonic model is selected to evaluate aircraft performance and trim under cruise conditions. The wake is terminated at the default downstream location.

A comparison between AVL and FlightStream results for the lift, drag, and pitching moment coefficients

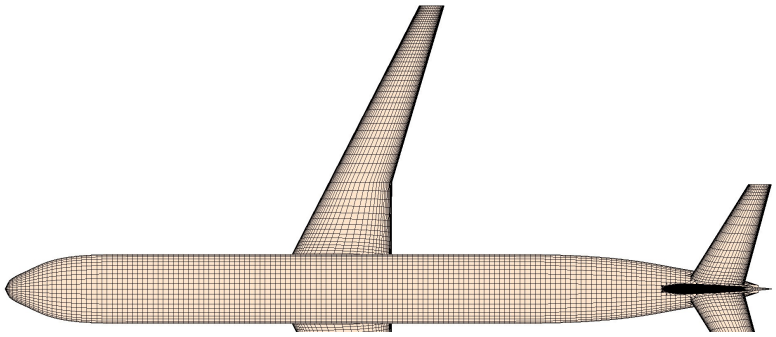

(a) Top view.

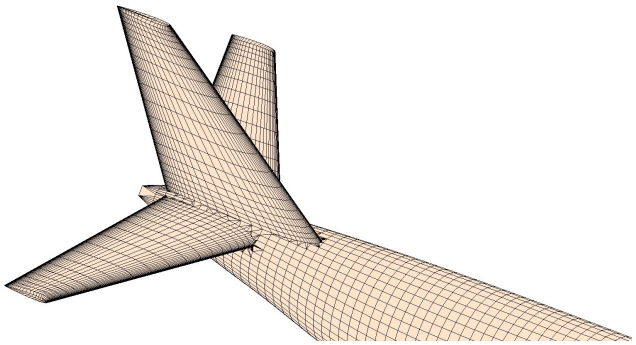

(b) Empennage close-up.

Figure 5.5: Mesh generated in FlightStream to validate the initial design.

	Initial		A321 Opt		APPU P		APPU W&P		APPU	
Solver	**FS**	**AVL**	**FS**	**AVL**	**FS**	**AVL**	**FS**	**AVL**	**FS**	**AVL**
α	1.726	1.726	1.663	1.663	1.583	1.583	1.860	1.860	1.825	1.825
$c_{L_{des}}$	0.465	0.600	0.450	0.596	0.440	0.604	0.468	0.605	0.390	0.605
$c_{D_{des}}$	0.039	0.024	0.039	0.023	0.035	0.024	0.035	0.024	0.039	0.024
$c_{M_{des}}$	-0.061	0.000	-0.021	0.000	0.013	0.001	-0.004	0.000	0.230	0.000

Table 5.4: Lift, drag, and pitching moment comparison at the design point between FlightStream and AVL.

at cruise for the initial design and each optimized configuration is provided in Table 5.4. As previously noted, the FlightStream simulations are performed at the same angle of attack as that determined by AVL to trim the aircraft at the design point. It is observed that the results for the APPU configuration show relatively larger discrepancies between AVL and FlightStream compared to the other configurations. In particular, the HTP generates significantly more downforce in the FlightStream simulation of the APPU configuration. This is likely due to a suboptimal mesh where the HTP intersects with the VTP, leading to local pressure peaks. The mesh on the empennage for the APPU configuration can be seen in Figure E.1d. Consequently, the APPU configuration in FlightStream exhibits reduced total lift, increased trim drag, and a pronounced nose-up pitching moment relative to the other configurations. From the pressure distributions, it appears that the main wing produces less lift for the APPU configuration compared to the other configurations. This strengthens the reduction in lift significantly. The pressure distributions for each configuration can be seen in Figure E.3 and E.4. Given the influence of the mesh irregularities at the HTP–VTP intersection and the resulting pressure effects, the accuracy of the FlightStream results for the APPU configuration is questionable. Therefore, this configuration is excluded from further validation analysis.

For the remaining configurations, FlightStream predicts between 22.5% and 24.5% less lift compared to AVL. This discrepancy can be partially attributed to the extension of wing elements to the centerplane in AVL, which artificially increases the effective span and lift. The spanwise lift distribution for the initial design at cruise, as predicted by both AVL and FlightStream, is shown in Figure 5.6. Although AVL predicts slightly higher lift along the entire main wing span, it is evident that a significant portion of the lift in AVL is generated near the fuselage centerline, beyond the physical extent of the wing in the FlightStream model. Part of the reduced lift observed over the remainder of the wing in FlightStream can be attributed to the decambering effects introduced by the viscous model. However, FlightStream has not consistently demonstrated reliability throughout this study, and its lift predictions in these simulations remain questionable. If a target lift coefficient of approximately 0.6 were to be achieved using FlightStream, the required angle of attack would likely fall outside a realistic operational range.

Additionally, FlightStream estimates higher drag levels than those predicted by the constant friction coefficient drag model used during optimization. This suggests that the calibrated friction coefficient employed in the optimization is underestimated relative to FlightStream's more detailed viscous modeling. In contrast, discrepancies in the pitching moment coefficients between AVL and FlightStream are relatively minor, indicating that all configurations, excluding the APPU configuration, are close to trimmed flight according to FlightStream.

Finally, examining the spanwise downforce distribution on the HTP for the initial design, it is observed that the AVL predictions align very closely with those from FlightStream. However, the agreement is less consistent for the optimized configurations, as shown in Figure E.2. This discrepancy is particularly pronounced for the APPU configuration, where the elevated downforce predicted by FlightStream is clearly visible, consistent with earlier observations.

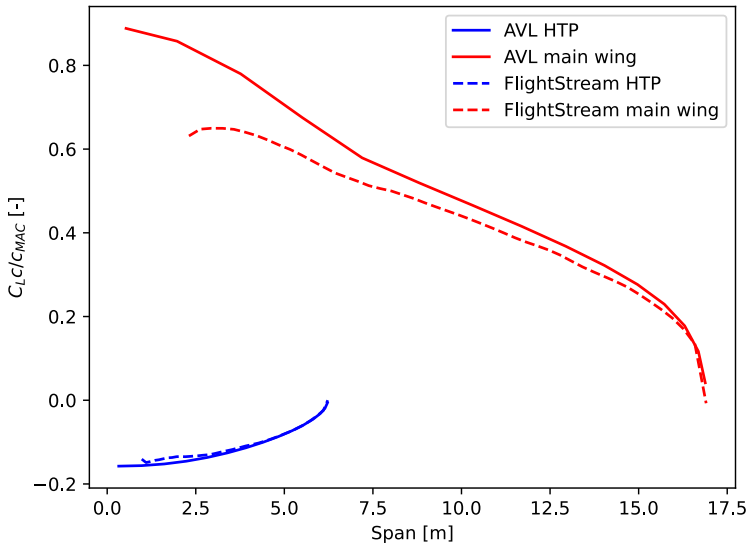

Figure 5.6: Spanwise lift distribution at cruise for the initial design according to AVL and FlightStream.

6

Conclusion

The primary objective of this study is to investigate how the optimal empennage design for an aircraft equipped with an APPU system differs from that of an aircraft without such a system. For both configurations, the optimal empennage is characterized by high aspect ratios and significantly reduced surface areas for the horizontal and vertical tailplanes compared to the baseline. However, notable differences arise in empennage configuration and sweep angles. For aircraft without an APPU system, a conventional tail with moderate sweep angles proves to be optimal. In contrast, APPU-equipped aircraft require a low cruciform tail to accommodate the hydrogen tank in the tail cone and benefit from reduced sweep angles, which help shift the aerodynamic center aft without intersecting the propulsor plane.

The A321neo serves as the baseline for this study. Its optimal empennage configuration is found to be a conventional tail; however, the empennage is over-designed. The horizontal and vertical tailplane surface areas can be reduced by 35.5% and 33.9%, respectively. The additional weight introduced by the APPU system shifts the center of gravity aft. As a result, the horizontal tailplane is required to generate less downforce, leading to more positive twist angles. This reduction in required downforce causes the optimizer to prioritize structural efficiency over aerodynamic efficiency, resulting in a more moderate aspect ratio. The vertical tailplane area needs to be increased to compensate for the increased yaw instability. Repositioning the main wing reverses these effects, resulting in more negative twist angles and a reduction in vertical tailplane area. The low cruciform empennage configuration and reduced sweep angles of an APPU-equipped aircraft are direct consequences of the hydrogen tank and propulsor placement. The horizontal tailplane height is raised to the minimum level needed to accommodate the hydrogen tank within the tail cone. The sweep angles are reduced to move the empennage's aerodynamic center as far aft as possible without intersecting the propulsor plane.

Not all research questions could be fully addressed. The current setup does not allow for effective optimization of airfoil geometries. AVL's modeling of only the camber line makes it unsuitable for optimizing symmetric profiles like those on vertical tailplanes. Additionally, the horizontal tailplane airfoils showed limited variation from the initial design, likely due to the dual-parameter CST definition. FlightStream proved infeasible for use in this study due to long run times and limited mesh robustness. In contrast, AVL offered better performance for integration into the optimization loop. To make panel codes like FlightStream viable in future studies, improvements in automated meshing and increased computational resources are necessary.

Finally, there are some recommendations for future work. Empennage airfoil optimization should be explored using solvers that account for thickness effects, such as panel methods or hybrid approaches combining a vortex lattice method with airfoil design tools like XFOIL. It is found that AVL prefers the horizontal tailplane as low as possible for increased aerodynamic efficiency. It is unclear at the moment what drives this preference. Therefore, more research is needed into this effect. Three potential sources for errors in the static margin estimates for this study are identified. How much each of these factors contributes to the static margin errors should be further investigated.

References

[1] A. Heidebrecht et al. *Development of a Hydrogen-powered Fuselage-mounted BLI Propulsor Add-on for Passenger Aircraft*. Tech. rep. TU Delft, Netherlands, 2022.

[2] D. Raymer. *Aircraft Design: A Conceptual Approach*. 5th ed. Reston, Virginia: American Institute of Aeronautics and Astronautics, 2012.

[3] S. Gudmundsson. *General Aviation Aircraft Design: Applied Methods and Procedures*. 2nd ed. Amsterdam, The Netherlands: Butterworth-Heinemann, 2021.

[4] Y. Liu and T. Jiang. "Conceptual Aircraft Empennage Design Based on Multidisciplinary Design Optimization Approach". In: *International Journal of Aerospace Engineering* 2022 (2022), pp. 1–9.

[5] J. D. Galloway Jr. "Optimization of Conceptual Aircraft Design for Stability/Control and Performance". Master's thesis. Seattle, Washington: University of Washington, 2000.

[6] C.C. Morris. "Flight Dynamic Constraints in Conceptual Aircraft Multidisciplinary Analysis and Design Optimization". Ph.D. thesis. Blacksburg, Virginia: Virginia Polytechnic Institute and State University, 2013.

[7] Skybrary. *B737 Series*. 2024. url: `https://skybrary.aero/aircraft-family/b737-series` (visited on 02/26/2024).

[8] D. Cosenza. "Handling Qualities Optimization in Aircraft Conceptual Design". Master's thesis. Delft, The Netherlands: Delflt University of Technology, 2016.

[9] Y. Denieul. "Preliminary Design of Control Surfaces and Laws for Unconventional Aircraft Configurations". Ph.D. thesis. Toulouse, France: Université de Toulouse, 2016.

[10] D.C. Garmendia. "A Multi-Disciplinary Conceptual Design Methodology for Assessing Control Authority on a Hybrid Wing Body Configuration". Ph.D. thesis. Atlanta, Georgia: Georgia Institute of Technology, 2015.

[11] K. Risse et al. "Central reference aircraft data system (CeRAS) for research community". In: *Central reference aircraft data system (CeRAS) for research community* 7.1 (2016), pp. 121–133.

[12] Skybrary. *A320 Series*. 2024. url: `https://skybrary.aero/aircraft-family/a320-family` (visited on 02/26/2024).

[13] B. Peerlings. "A review of aerodynamic flow models, solution methods and solvers – and their applicability to aircraft conceptual design". Master's thesis. Delft, The Netherlands: Delft University of Technology, Nov. 2018.

[14] J. Blazek. *Computational Fluid Dynamics - Principles and Applications*. 3th ed. Oxford, United Kingdom: Butterworth-Heinemann / Elsevier, 2007.

[15] J. Mariens. "Wing Shape Multidisciplinary Design Optimization". Master's thesis. Delft, The Netherlands: Delft University of Technology, 2012.

[16] J.D. Anderson et al. *Computational Fluid Dynamics: an Introduction*. 3th ed. Springer-Verlag Berlin Heidelberg, 2009.

[17] J.D. Anderson. *Fundamentals of Aerodynamics*. 3rd ed. New York, New York: McGraw-Hill, 2001.

[18] J.J. Bertin and R.M. Cummings. *Aerodynamics for Engineers*. 5th ed. Upper Saddle River, New Jersey: Pearson Prentice-Hall, 2009.

[19] W.H. Mason. "Incompressible Potential Flow Using Panel Methods". In: *Applied Computational Aerodynamics Text*. Virginia Polytechnic Institute and State University, 1995. Chap. 4.

[20] J.L. Hess. “Development and Application of Panel Methods”. In: *Advanced Boundary Element Methods*. Ed. by Thomas A. Cruse. Berlin, Germany: Springer Berlin Heidelberg, 1988, pp. 165–177.

[21] DARcorporation. *FlightStream - Panel Methods Reimagined*. 2024. url: https://www.darcorp.com/wp-content/uploads/2022/12/FlightStream-Brochure-2022.pdf (visited on 03/20/2024).

[22] R. Hartfield, V. Ahuja, and I. Chakraborty. “Aero-Propulsive Analysis for Contemporary Conceptual Design”. In: *AIAA Aviation 2019 Forum*. AIAA 2019-3019. Dallas, Texas, June 2019.

[23] M. Drela and H. Youngren. *AVL 3.36 User Primer*. MIT Aero & Astro and Aerocraft, inc. Feb. 2017.

[24] M.H. Sadraey. *Aircraft Design: A Systems Engineering Approach*. 1st ed. Hoboken, New Jersey: John Wiley & Sons, 2013.

[25] J.E. Williams and S.R. Vukelich. *The USAF Stability and Control Digital DATCOM. Volume I. Users Manual*. Tech. rep. Air Force Flight Dynamics Laboratory, 1979.

[26] P.M. Sforza. *Commercial Airplane Design Principles*. 1st. Oxford, United Kingdom: Butterworth-Heinemann, 2014.

[27] R. Swischuk and D. Allaire. *A Machine Learning Approach to Aircraft SensorError Detection and Correction*. Tech. rep. Texas A&M University, 2018.

[28] E. Torenbeek. *Synthesis of Subsonic Airplane Design*. 1st ed. Delft, The Netherlands: Delft University Press, 1982.

[29] J.P. How. *16.333: Lecture #7 Approximate Longitudinal Dynamics Models*. Lecture notes MIT. 2004.

[30] MIL-STD-1797A. *FLYING QUALITIES OF PILOTED AIRCRAFT*. Tech. rep. DEPARTMENT OF DEFENSE INTERFACE STANDARD, 1997.

[31] B. Etkin and L. D. Reid. *Dynamics of Flight: Stability and Control*. 3rd ed. Chichester, New York: Wiley, 1996.

[32] F. Nicolosi et al. “Experimental analysis of aircraft directional control effectiveness”. In: *Aerospace Science and Technology* 106.106099 (2020).

[33] A.K. Kundu. *Aircraft Design*. 1st. New York, New York: Cambridge University Press, 2010.

[34] A.B. Lambe and J.R.R.A Martins. “A Unified Description of MDO Architectures”. In: *9th World Congress on Structural and Multidisciplinary Optimization*. Shizuoka, Japan, June 2011.

[35] E.J. Cramer et al. “Problem formulation for multidisciplinary optimization”. In: *SIAM Journal on Optimization* 4.4 (1994), pp. 754–776.

[36] D. Kraft. *A Software Package for Sequential Quadratic Programming*. Tech. rep. DFVLR-FB 88-28. Koln, Germany: DLR German Aerospace Center — Institute for Flight Mechanics, 1988.

[37] Q. Ran et al. “Multi-objective optimization design of an umbilical cross-sectional layout based on the sequential least squares quadratic programming algorithm”. In: *Ocean Engineering* 321 (2025), p. 120365. issn: 0029-8018. doi: https://doi.org/10.1016/j.oceaneng.2025.120365. url: https://www.sciencedirect.com/science/article/pii/S0029801825000800.

[38] R.B. Wilson. “A simplicial Algorithm for Concave Programming”. Ph.D. thesis. Boston, Massachusetts: Graduate School of Business Administration, Harvard University, 1963.

[39] J. Nocedal and S.J. Wright. “Line search methods”. In: *Numerical optimization* (2006), pp. 30–65.

[40] N.P. Salunke, R.A. Juned Ahamad, and S.A. Channiwala. “Airfoil Parameterization Techniques: A Review”. In: *American Journal of Mechanical Engineering* 2.4 (2014), pp. 99–102.

[41] B. Kulfan. “A Universal Parametric Geometry Representation Method – “CST””. In: *45th AIAA Aerospace Sciences Meeting and Exhibit*. Boeing Commercial Airplane Group. Reno, Nevada: American Institute of Aeronautics and Astronautics, Jan. 2007.

[42] A. Raju Kulkarni et al. “Assessment of Sub-scale Designs for Scaled Flight Testing”. In: *AIAA Aviation Forum and Exposition*. American Institute of Aeronautics and Astronautics. June 2019.

[43] J. Roskam. *Airplane Design*. Airplane Design pt. 5. DARcorporation, 1985. isbn: 9781884885501.

[44] M. Orlita. “Cruise Performance Optimization of the Airbus A320 through Flap Morphing”. Master’s thesis. Delft University of Technology, Aug. 2016.

[45] EASA. *EASA Easy Access Rules for Large Aeroplanes (CS-25)*. 2023. url: https://www.easa.europa.eu/en/document-library/easy-access-rules/online-publications/easy-access-rules-large-aeroplanes-cs-25?page=15#_DxCrossRefBm548991248 (visited on 11/05/2024).

[46] L. Jenkinson, P. Simpkin, and D. Rhodes. *Civil Jet Aircraft Design*. 2001. url: https://booksite.elsevier.com/9780340741528/appendices/data-a/default.htm (visited on 11/11/2024).

[47] Altair Engineering Inc. *User Manual 24.1 Altair FlightStream*. 2024.

[48] K. Budziak. *Aerodynamic Analysis with Athena Vortex Lattice (AVL)*. Tech. rep. Hamburg University of Applied Sciences, 2015.

[49] S. Gudmundsson. “Chapter 16 - Aircraft Drag Analysis”. In: *General Aviation Aircraft Design (Second Edition)*. Ed. by S. Gudmundsson. Second Edition. Butterworth-Heinemann, 2022, pp. 657–752. isbn: 978-0-12-818465-3. doi: https://doi.org/10.1016/B978-0-12-818465-3.00016-1. url: https://www.sciencedirect.com/science/article/pii/B9780128184653000161.

[50] E. Obert. *Aerodynamic Design of Transport Aircraft*. Amsterdam, The Netherlands: IOS press, Incorporated, 2009.

[51] F. Nicolosi et al. “A comprehensive review of vertical tail design”. In: Sept. 2016. doi: 10.13140/RG.2.2.12606.69448.

[52] Safran. *LEAP-1A, a new-generation engine for the A320neo family*. url: https://www.safran-group.com/products-services/leap-1a-new-generation-engine-single-aisle-commercial-jets (visited on 11/19/2024).

[53] L.K. Fitzgerald. “A Novel Approach to Determining Aircraft Stability Derivatives in Extreme Flight Conditions”. Ph.D. thesis. Limerick, Ireland: University of Limerick, 2024.

[54] Y.A. Çengel and J.M. Cimbala. *Fluid Mechanics: Fundamentals and Applications*. 3th ed. New York, New York: McGraw-Hill, 2014.

[55] A. Heidebrecht et al. “Low-Threshold Hydrogen Propulsion: Outcomes of the APPU Project”. In: *TSAS 2025 #40*. Association Aéronautique et Astronautique de France. Delft, The Netherlands, Jan. 2025, pp. 1–12.

[56] Digital Dutch. *1976 Standard Atmosphere Calculator*. 1999. url: https://www.digitaldutch.com/atmoscalc/ (visited on 02/25/2025).

[57] A. Heidebrecht et al. “Results from the APPU Project: the Potential of Low-Treshold Hydrogen-Powered BLI Propulsion”. In: Internatioanl Council of the Aeronautical Sciences. Delft, The Netherlands, Sept. 2024, pp. 1–16.

A

Parameters

Throughout the implementation of the method, certain parameters are required that are not controlled by the optimization algorithm, but remain constant throughout the process. Two aircraft versions are considered in this study: the standard A321neo and the APPU aircraft. Some general aircraft parameters are given in Table A.1. With the exception of the wing mean aerodynamic chord location, these parameters are valid for both aircraft versions. The wing mean aerodynamic chord location is 22.78m for the APPU aircraft since the wing is shifted back 1.2m. Table A.2 shows some aircraft and component weights that are relevant in the method for each aircraft version. The centers of gravity that are of interest for the method are given in Table A.3.

Two design points are considered throughout this study: cruise and approach. The corresponding atmospheric conditions and freestream velocity at cruise can be seen in the third column of Table A.4. At approach, ground level atmospheric conditions are considered, as can be seen in the fourth column of Table A.4.

Finally, the specific fuel consumptions that are required for the performance discipline are given in Table A.5. It is estimated that 17.1% of the thrust would be delivered by the APPU propulsor during cruise and the remainder by the main engines. This results in a total sfc of $1.262 \cdot 10^{-5} kg/Ns$ for the APPU version, according to the weighted average.

Parameter	Symbol	Value	Unit
Wing span	b_{wing}	33.91	m
Fuselage width at HTP	F_w	1.37	m
Wing mean aerodynamic chord	MAC_{wing}	4.29	m
Ultimate load factor	n_{ult}	3.75	-
Range	R	7,400,000	m
Wing surface area	S_{wing}	122.4	m^2
Single engine thrust	T_{engine}	155,688	N
Wing mean aerodynamic chord location	$x_{MAC,wing}$	21.58	m
Engine location from center line	y_{engine}	5.73	m

Table A.1: General aircraft parameters [46, 52].

Weight	A321neo	APPU	Unit
OEW	50,674	53,123	kg
W_{HTP}	1,189	986	kg
W_{VTP}	415	409	kg
W_{wing}	15,703	15,703	kg
$OEW_{fuselage}$	33,366	36,024	kg
$OEW_{tailless}$	49,069	51,727	kg
$W_{payload}$	25,000	25,000	kg

Table A.2: Aircraft and component weights [46, 55].

Center of Gravity	A321neo	APPU	Unit
$x_{CG,OE}$	20.53	21.76	m
$x_{CG,HTP}$	42.60	42.60	m
$x_{CG,VTP}$	42.13	42.13	m
$x_{CG,wing}$	20.67	21.89	m
$x_{CG,OE_{fuselage}}$	19.41	20.90	m
$x_{CG,ker}$	19.075	20.295	m
$x_{CG,hyd}$	N.A.	40.16	m
$x_{CG,paylaod}$	19.722	19.722	m

Table A.3: Aircraft and component centers of gravity.

Condition	Symbol	Cruise	Approach	Unit
Altitude	h	11,277.6	0	m
Freestream velocity	V	233.4	71	m/s
density	ρ	0.410	1.225	kg/m^3
pressure	p	26,218.	101,325	Pa
temperature	T	222.8	288.15	K
viscosity	μ	$1.467{\cdot}10^{-5}$	$1.812{\cdot}10^{-5}$	Ns/m^2
speed of sound	a	299.2	340.3	m/s
Mach number	M	0.78	0.21	-

Table A.4: Flight Conditions [56, 46].

Propulsion System	Symbol	Value	Unit
A321neo	sfc_{neo}	$1.573{\cdot}10^{-5}$	kg/Ns
APPU main engines	$sfc_{APPU,main}$	$1.425{\cdot}10^{-5}$	kg/Ns
APPU propulsor	$sfc_{APPU,prop}$	$4.717{\cdot}10^{-6}$	kg/Ns
APPU total	sfc_{APPU}	$1.262{\cdot}10^{-5}$	kg/Ns

Table A.5: Specific fuel consumption for different propulsion systems [46, 57].

B

Automatic Mesh Overview

Figure B.1 Provides some more detailed close-ups of the automatically generated mesh shown in Figure 4.21.

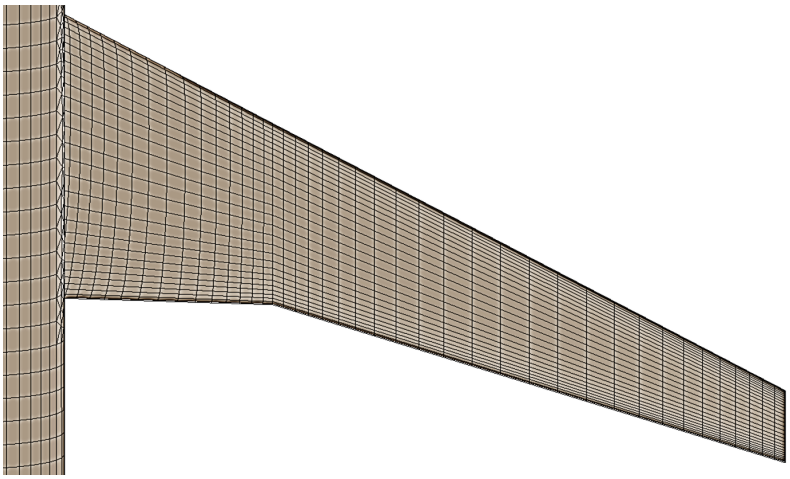

(a) Mesh on the wing.

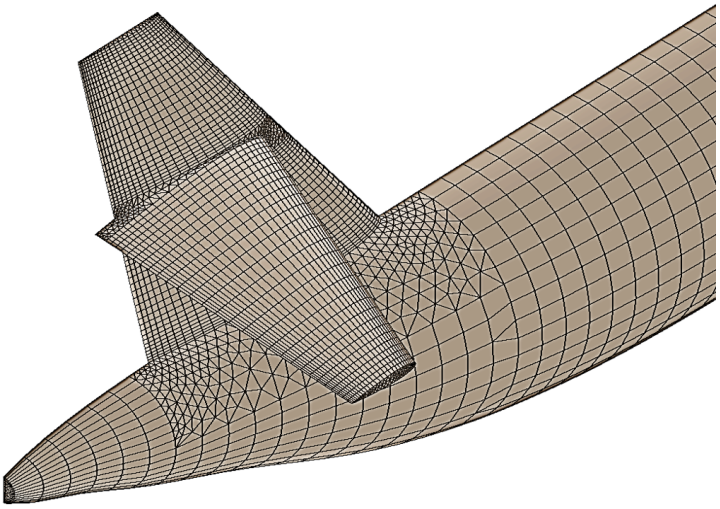

(b) Mesh on the empennage.

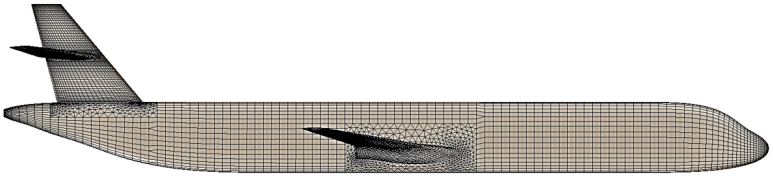

(c) Mesh on the fuselage.

Figure B.1: Detail views of the automatically generated mesh on an aircraft with an example empennage design.

C

HTP Airfoil Optimization Results

Table C.1 shows the initial and final values for the CST coefficients for each configuration. It can be seen that the optimizer did not change the coefficients a lot. The maximum variance in a single CST coefficient for one of the optimized designs compared to the initial design is approximately 5%. However, most optimized coefficients do not vary more than 1% from their initial value. This is also visualized in Figure C.1 where the optimized airfoils both at the root and at the tip of the horizontal tailplane are drawn on top of the initial design airfoils. One can see that there appears to be little to no change from the initial design in the airfoil geometry for both the horizontal tailplane root and tip for any of the configurations.

Nr.	Variable	Initial	A321 Opt	APPU P	APPU W&P	APPU	Unit
9	$\mathrm{CST}_{\mathrm{HTP}_{\mathrm{ur1}}}$	0.169	0.161	0.169	0.170	0.175	-
10	$\mathrm{CST}_{\mathrm{HTP}_{\mathrm{ur2}}}$	0.158	0.152	0.162	0.160	0.165	-
11	$\mathrm{CST}_{\mathrm{HTP}_{\mathrm{ur3}}}$	0.130	0.128	0.132	0.130	0.138	-
12	$\mathrm{CST}_{\mathrm{HTP}_{\mathrm{ur4}}}$	0.159	0.157	0.161	0.161	0.157	-
13	$\mathrm{CST}_{\mathrm{HTP}_{\mathrm{lr1}}}$	0.168	0.168	0.171	0.173	0.173	-
14	$\mathrm{CST}_{\mathrm{HTP}_{\mathrm{lr2}}}$	0.158	0.155	0.160	0.161	0.158	-
15	$\mathrm{CST}_{\mathrm{HTP}_{\mathrm{lr3}}}$	0.130	0.129	0.130	0.130	0.130	-
16	$\mathrm{CST}_{\mathrm{HTP}_{\mathrm{lr4}}}$	0.159	0.157	0.159	0.153	0.159	-
17	$\mathrm{CST}_{\mathrm{HTP}_{\mathrm{ut1}}}$	0.168	0.168	0.168	0.170	0.167	-
18	$\mathrm{CST}_{\mathrm{HTP}_{\mathrm{ut2}}}$	0.158	0.158	0.159	0.157	0.157	-
19	$\mathrm{CST}_{\mathrm{HTP}_{\mathrm{ut3}}}$	0.130	0.129	0.130	0.128	0.134	-
20	$\mathrm{CST}_{\mathrm{HTP}_{\mathrm{ut4}}}$	0.159	0.158	0.160	0.162	0.166	-
21	$\mathrm{CST}_{\mathrm{HTP}_{\mathrm{lr1}}}$	0.168	0.161	0.164	0.169	0.165	-
22	$\mathrm{CST}_{\mathrm{HTP}_{\mathrm{lr2}}}$	0.158	0.152	0.155	0.154	0.151	-
23	$\mathrm{CST}_{\mathrm{HTP}_{\mathrm{lt3}}}$	0.130	0.125	0.129	0.127	0.132	-
24	$\mathrm{CST}_{\mathrm{HTP}_{\mathrm{lt4}}}$	0.159	0.154	0.159	0.156	0.159	-

Table C.1: Initial and final values of the CST coefficients for all configurations.

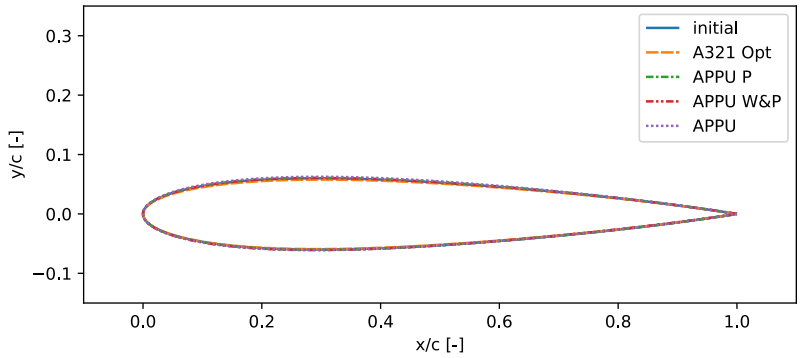

(a) HTP root airfoil.

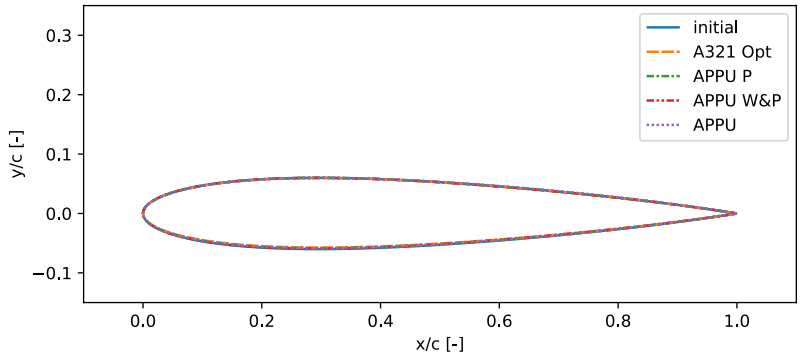

(b) HTP tip airfoil.

Figure C.1: Overlay of the horizontal tailplane airfoils of the final design for every optimized configuration and the initial design.

D

Convergence History & Geometries

The termination criteria for the four different optimization cases remain constant between different configurations, with one exception. The objective tolerance is set at $1{\cdot}10^{-3}$ for all configurations except the APPU configuration, where it is set at $5{\cdot}10^{-4}$. section D.4 provides a deeper insight into the reasoning behind this. The constraint tolerance is set at $1{\cdot}10^{-3}$ for each configuration, and the step size for the gradient search is set at $5{\cdot}10^{-2}$.

All the constraints in this study are presented in Table D.1. C_2 and C_7 are not plotted in the constraint convergence histories in this appendix. C_7 is not plotted because it only applies to FlightStream as AVL can match a target lift coefficient. An explanation for omitting C_2 is provided in subsection 5.2.6.

Name	Constraint
C_1	$C_{m_\alpha} < 0$
C_2	$S.M. < 0.1$
C_3	$S.M. > 0.05$
C_4	$C_{N_\beta} > 0$
C_5	$C_{L_\beta} < 0$
C_6	$C_{Y_\beta} < 0$
C_7	$\frac{L_{des}-W_{des}}{L_{des}} = 0$
C_8	$C_{M_{des}} = 0$
C_9	$\frac{N_{max}-N_{engine}}{N_{max}} > 0$
C_{10}	$C_{M_{\delta_e}} < -0.0035$
C_{11}	$C_{N_{\delta_r}} > 0.004$
C_{HTP}	$\frac{Z_{HTP}-Z_{HTP,min}}{Z_{HTP,min}}$

Table D.1: Overview of all the constraints.

D.1. Optimized A321neo

The first configuration is the optimized A321neo configuration. It has the same mass (excluding the empennage), specific fuel consumption, wing position, and empennage position as the standard A321neo. A summary of the optimization process for the baseline aircraft can be found in Figure D.1. The objective, which is the normalized fuel weight, decreases steadily until it stagnates at 0.966. This corresponds to a reduction in fuel consumption of 3.4%. The final values for the design variables are shown

in the bar graph at the bottom of Figure D.1. The bar graph represents the final values for the design variables with respect to the upper and lower bounds. These bounds are presented in subsection 4.9.1 and 4.9.2.

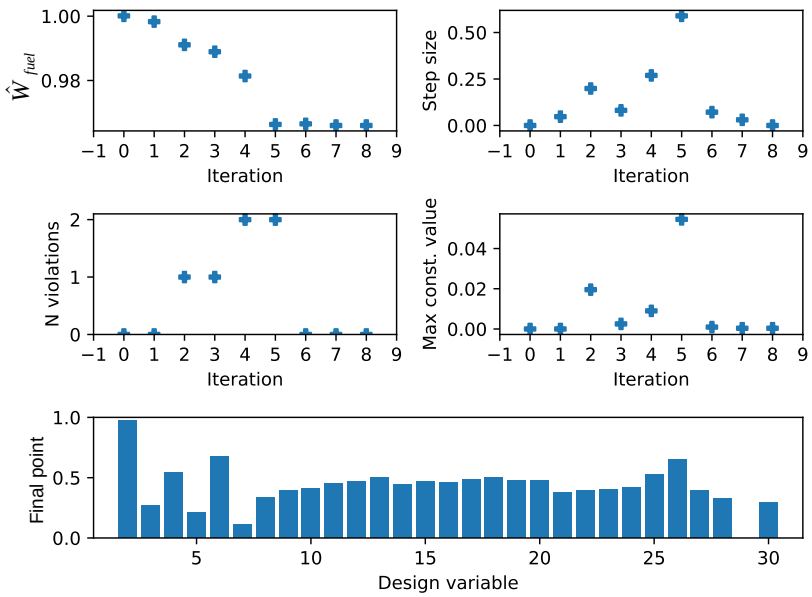

Figure D.1: Summary of the optimization process for the optimized A321neo configuration. Empty bars in the bar graph mean that the variables are at the lower bound and a full bars mean that the variables are at the upper bound. The index of each design variable can be seen in Table 5.2 and C.1.

The convergence of the constraints throughout the optimization process is visualized in Figure D.2. The equality constraint C_8, which states that the pitching moment at trim should be zero, is plotted in Figure D.2a. The inequality constraints are plotted in Figure D.2b. A description of the constraints can be found in Table D.1. From the numbers of constraints violated at each iteration in the summary of Figure D.1 and the convergence of the constraints in Figure D.2, it is clear that all the requirements for stability and control are met with the final design. In addition, the constraint violations throughout the optimization process remain relatively low.

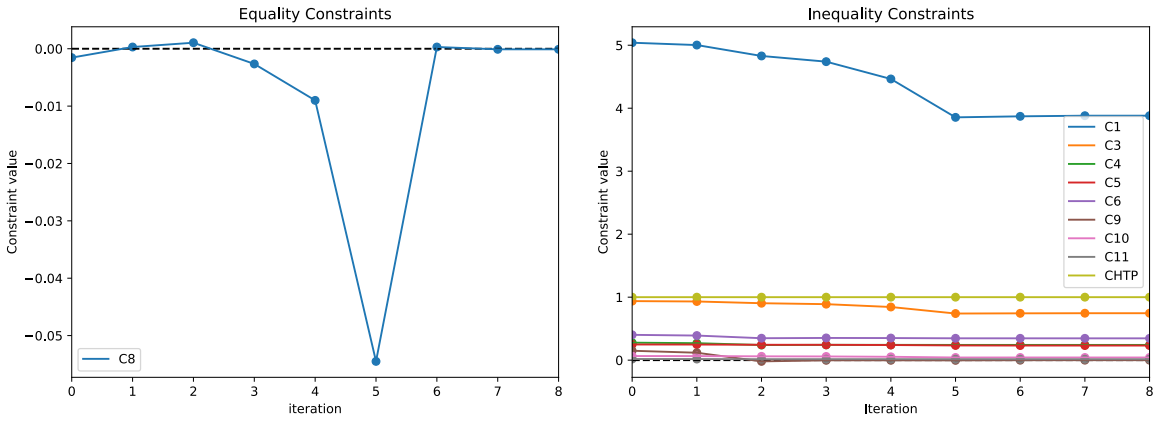

(a) Equality constraints.

(b) Inequality constraints.

Figure D.2: Constraint values throughout the optimization process for the optimized A321neo configuration.

A visual representation of the final design of the optimized A321neo configuration is given in Figure D.3.

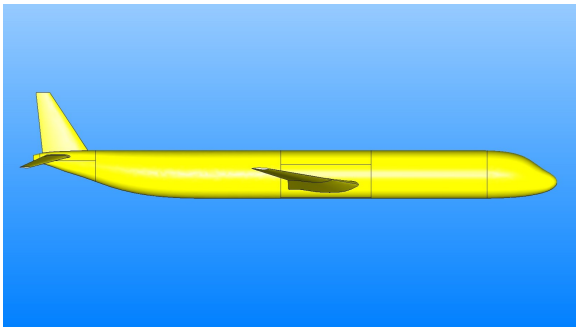

(a) Side view.

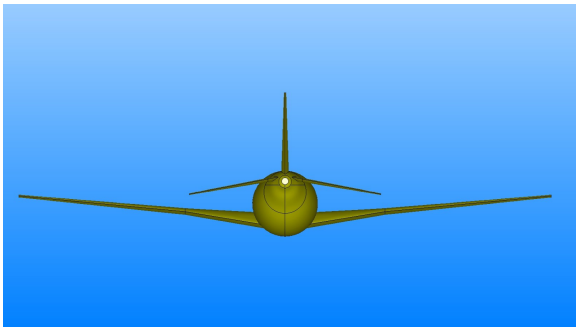

(b) Rear view.

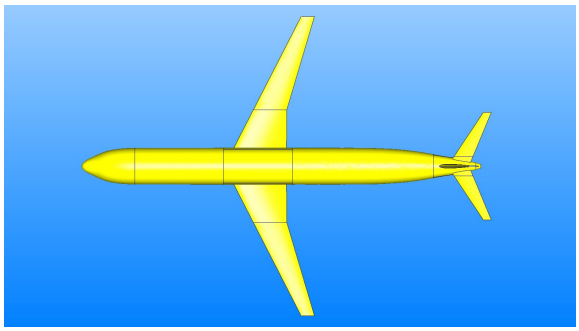

(c) Top view.

Figure D.3: Resulting geometry for the optimized A321neo configuration.

D.2. APPU Propulsion

The second configuration investigated is called the APPU propulsion configuration. The difference with the optimized A321neo configuration is the inclusion of the APPU propulsion system. As a result, the mass, excluding the empennage, and the specific fuel consumption are equal to the tailless OEW and specific fuel consumption of the APPU aircraft. The summary of the optimization process for the APPU propulsion configuration is shown in Figure D.4. The normalized fuel weight plotted in the top-left graph is reduced from 0.813 to 0.788. This is a relative reduction of 3.1%. Note that the objective value does not start at 1 for the initial design. This is due to the reduced specific fuel consumption of the APPU propulsion system, which results in a lower fuel load for the initial design. However, the fuel mass is still normalized with respect to the fuel mass for the initial design with the A321neo propulsion system. A graphic representation of the final values for the design variables is given by the bar graph at the bottom of Figure D.4.

The constraint convergence for the APPU propulsion configuration can be seen in Figure D.5. The equality constraint on the pitching moment at cruise is plotted in Figure D.5a, while the remaining inequality constraints are plotted in Figure D.5b. The definition of each constraint is given in Table D.1. The number of constraint violations and the maximum violation at each iteration of the optimization process are shown in the two middle graphs of Figure D.4. It can be seen that the aircraft is not trimmed for the initial design. This is caused by the shift in weight and center of gravity as a result of the change in the propulsion system. The optimizer is able to trim the aircraft after one iteration.

The final design of the empennage for the APPU propulsion configuration is visible in Figure D.6.

D.3. APPU Wing & Propulsion

The third configuration is the APPU wing and propulsion configuration. It differs from the APPU propulsion in the main wing position. The main wing is repositioned 1.2m aft to cope with the shift in center of gravity. The optimization summary for the APPU wing and propulsion configuration is shown in Figure D.7. The normalized fuel weight is minimized from 0.814 for the initial design to 0.792 for the

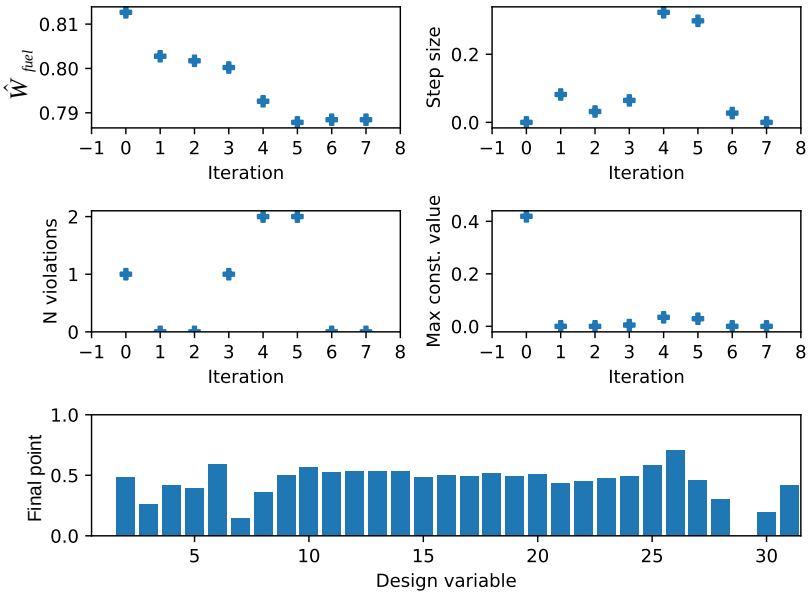

Figure D.4: Summary of the optimization process for the APPU propulsion configuration. Empty bars in the bar graph mean that the variables are at the lower bound and a full bars mean that the variables are at the upper bound. The index of each design variable can be seen in Table 5.2 and C.1.

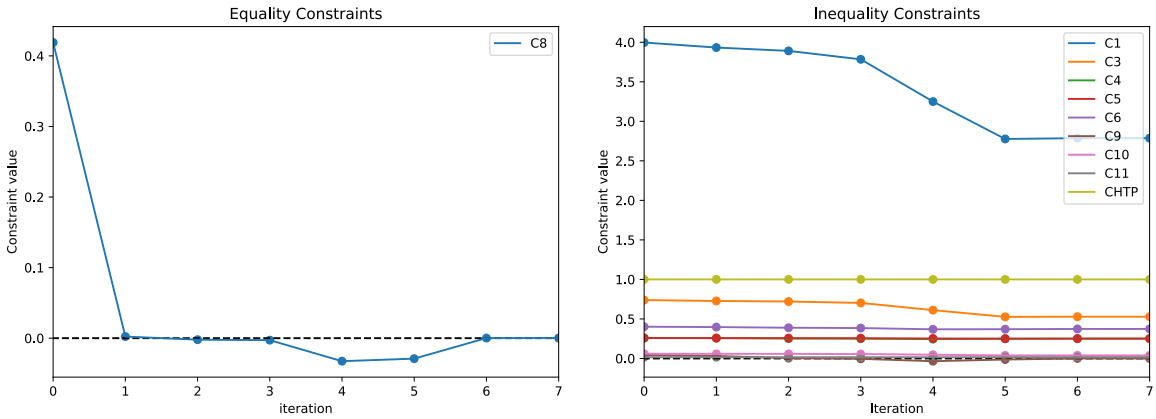

(a) Equality constraints.

(b) Inequality constraints.

Figure D.5: Constraint values throughout the optimization process for the APPU propulsion configuration.

final design, corresponding to a reduction of 2.7%. Note that the function value is increased in the first iteration to bring the number of constraint violations down to zero. A bar graph with the final values for the design variables is shown at the bottom of Figure D.7.

The convergence history of the constraints is shown in Figure D.8 with the pitching moment equality constraint plotted in Figure D.8a and the inequality constraints plotted in Figure D.8b. The definitions of all the constraints are given in Table D.1. The number of constraint violations and the maximum violation are presented in the optimization summary in Figure D.7. The only constraint violated at the initial design is the equality constraint on the pitching moment which is negative instead of zero. This means that the aircraft is not trimmed at the initial design, but pitches nose down. The only inequality constraint that is violated during the optimization process is C_9, which states that the aerodynamic yawing moment at the maximum sideslip angle during approach should be strong enough to counter a one engine inoperative situation. No constraints are violated for the final design, indicating that the aircraft meets all the stability and control requirements that have been set.

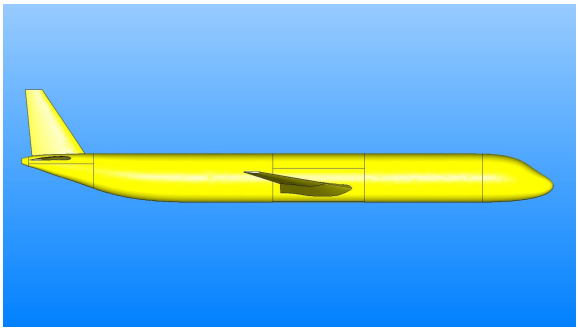

(a) Side view.

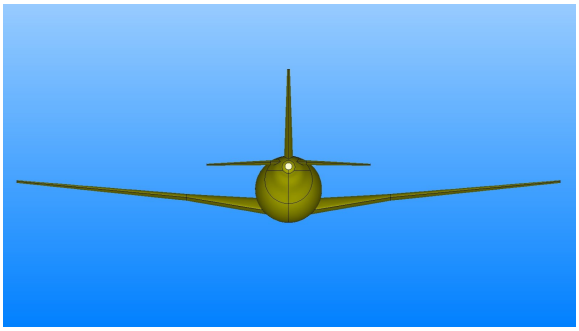

(b) Rear view.

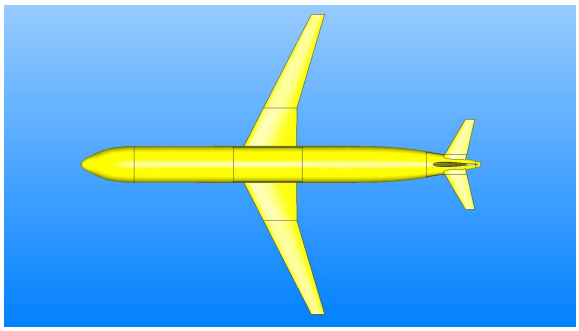

(c) Top view.

Figure D.6: Resulting geometry for the APPU propulsion configuration.

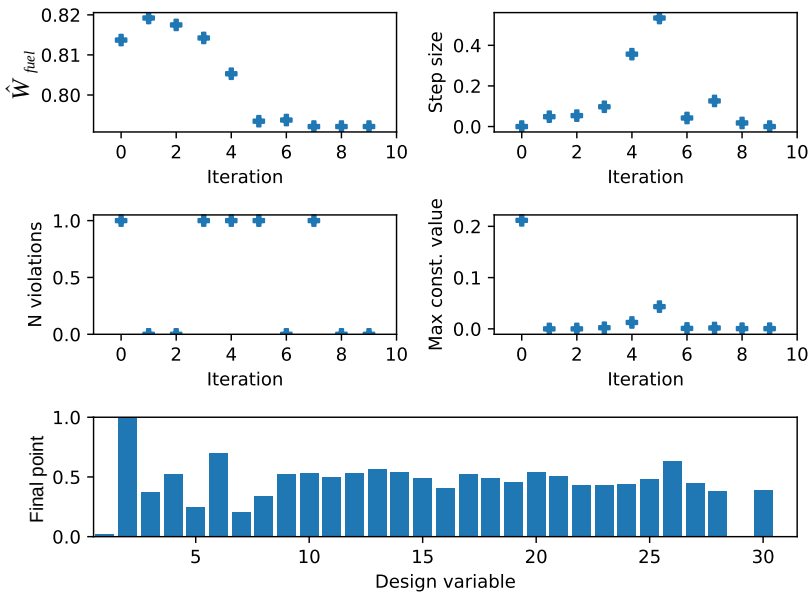

Figure D.7: Summary of the optimization process for the APPU wing and propulsion configuration. Empty bars in the bar graph mean that the variables are at the lower bound and a full bars mean that the variables are at the upper bound. The index of each design variable can be seen in Table 5.2 and C.1.

The final empennage design for the APPU wing and propulsion configuration is visualized in Figure D.9.

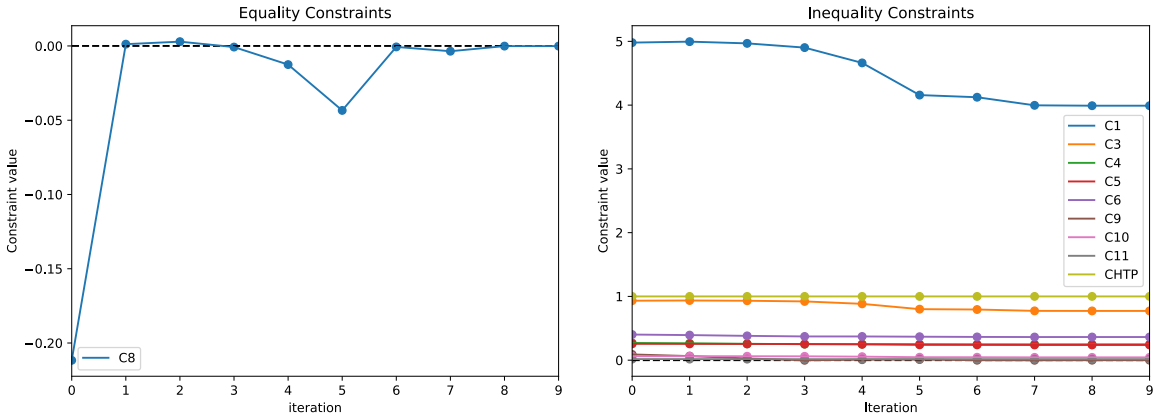

(a) Equality constraints.

(b) Inequality constraints.

Figure D.8: Constraint values throughout the optimization process for the APPU wing and propulsion configuration.

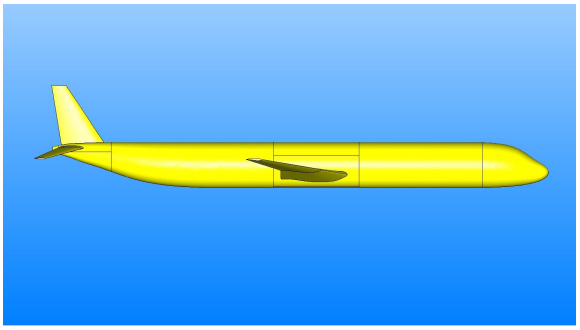

(a) Side view.

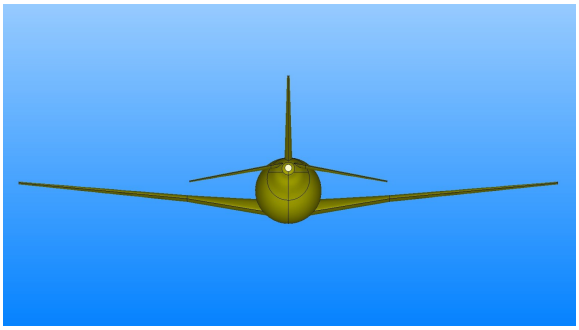

(b) Rear view.

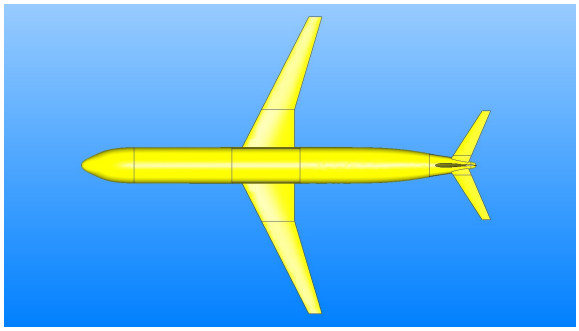

(c) Top view.

Figure D.9: Resulting geometry for the APPU wing and propulsion configuration.

D.4. APPU

The final configuration is the full APPU configuration. Compared to the APPU wing and propulsion configuration, it takes the geometrical constraints on the empennage due to the installation of the APPU system into account. These geometrical constraints on the empennage imply two limitations. First, the empennage is positioned such that no part of the empennage intersects with the propulsor plane. Second, the minimum height for the HTP in C_{HTP} is set to 1m instead of 0m, as is the case for the other configurations. The summary of the optimization process can be seen in Figure D.10. The normalized fuel weight is reduced from 0.813 for the initial design to 0.800 for the final design. This is a relative reduction of 1.6%. After two iterations, all constraint violations have been eliminated and the optimizer starts looking for more optimal designs. Notice that the optimizer needed approximately two to three times as many iterations as for the other three configurations. This is because of the lower

objective tolerance of $5 \cdot 10^{-4}$ for this configuration compared to the objective tolerance of $1 \cdot 10^{-3}$ for the other configurations. This lower objective tolerance is required to prevent the optimization process from terminating after the second iteration.

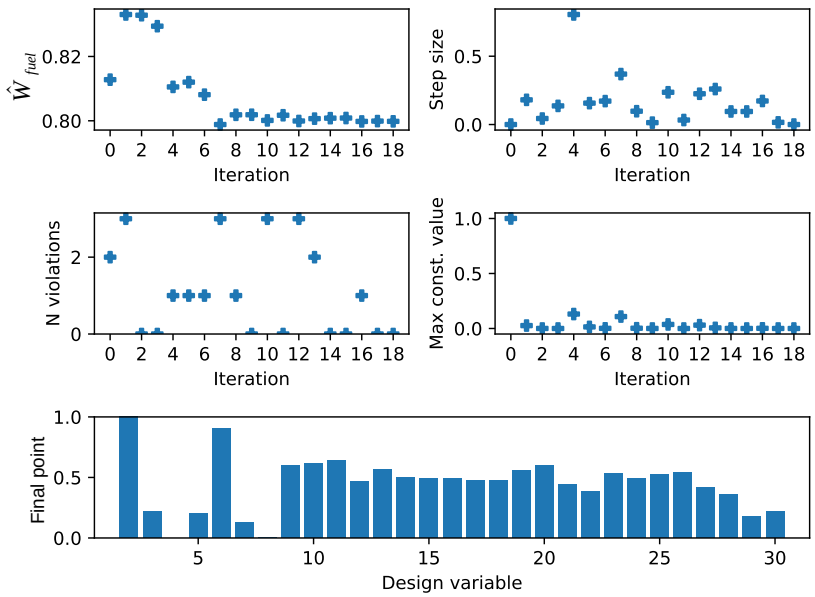

Figure D.10: Summary of the optimization process for the APPU configuration. Empty bars in the bar graph mean that the variables are at the lower bound and a full bars mean that the variables are at the upper bound. The index of each design variable can be seen in Table 5.2 and C.1.

The constraint convergence at each iteration of the optimization process is plotted in Figure D.11. The only equality constraint, C_8, is plotted in Figure D.11a. It states that the pitching moment coefficient should be zero at cruise. The remainder of the constraints are plotted in Figure D.11b. The definition of each of the constraints in Figure D.11 is given in Table D.1. Looking at the number of constraint violations in Figure D.10, it can be seen that the optimizer is having more trouble eliminating the violations compared to the other configurations. A maximum of three constraint violations is recorded at multiple iterations. These violations include the pitching moment constraint C_8, the maximum aerodynamic yawing moment constraint C_9, and the constraint on the HTP height C_{HTP}. However, the magnitude of the violations appears to decrease with additional iterations, and no constraint violations are present at the final design. This indicates that the aircraft meets all the stability and control requirements that have been set for this study, as well as the minimum height of the HTP.

The final design of the APPU configuration can be seen in Figure D.12.

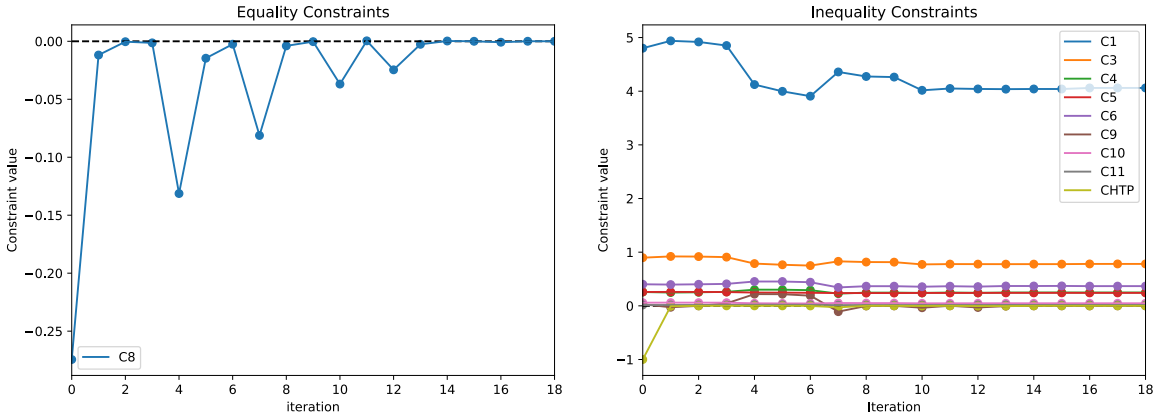

(a) Equality constraints.

(b) Inequality constraints.

Figure D.11: Constraint values throughout the optimization process for the APPU configuration.

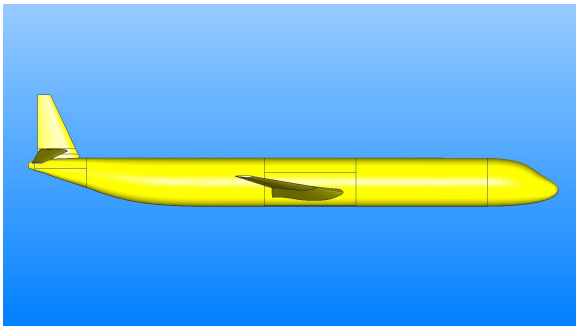

(a) Side view.

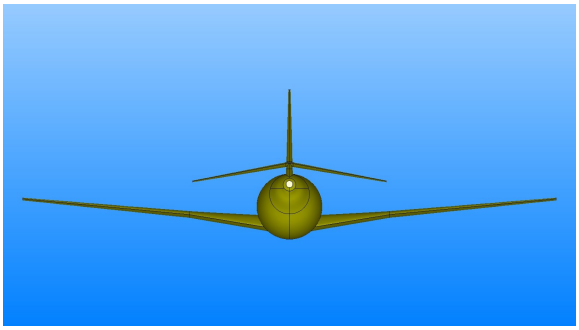

(b) Rear view.

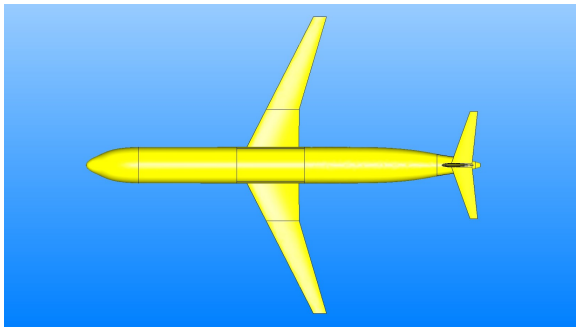

(c) Top view.

Figure D.12: Resulting geometry for the APPU configuration.

E

FlightStream Validation

E.1. Empennage Mesh

Figure E.1 shows the different FlightStream meshes for the optimized configurations. A suboptimal mesh is present at the HTP-VTP intersection for the APPU configuration.

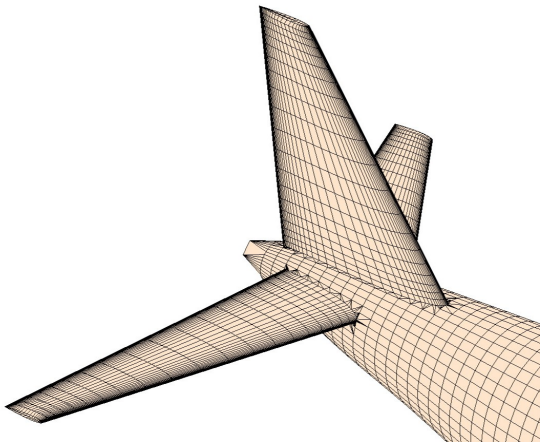

(a) Optimized A321neo.

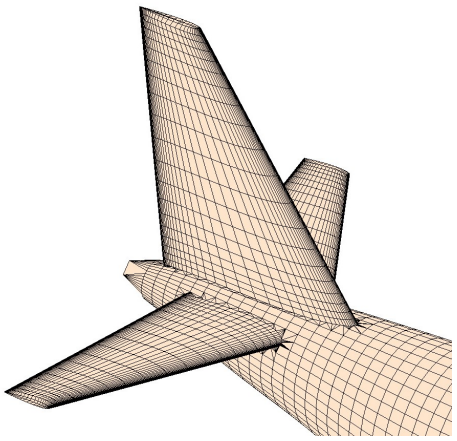

(b) APPU Propulsion.

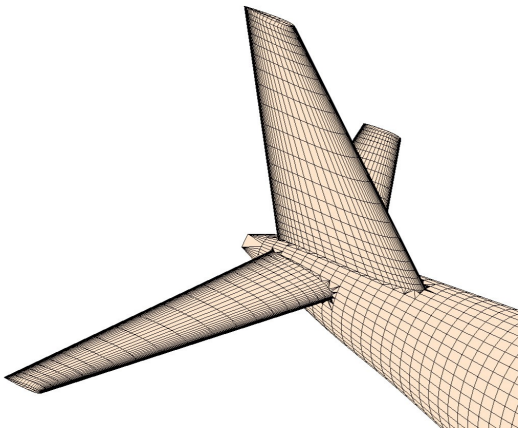

(c) APPU Wing & Propulsion.

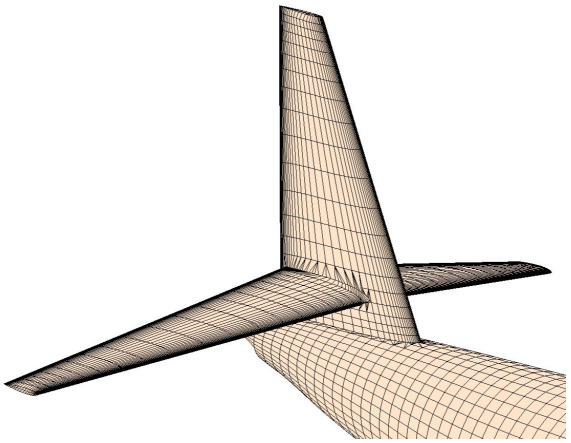

(d) APPU.

Figure E.1: Empennage meshes on optimized geometries generated in FlightStream.

E.2. Spanwise Lift Distribution

Figure E.2 shows the spanwise lift distributions for the optimized configurations. It is evident that FlightStream predicts more triangular lift distributions on the HTP, whereas AVL produces more elliptical distributions. The increased downforce level on the HTP for the APPU configuration is also clearly visible and remains consistent with discrepancies noted in subsection 5.4.2.

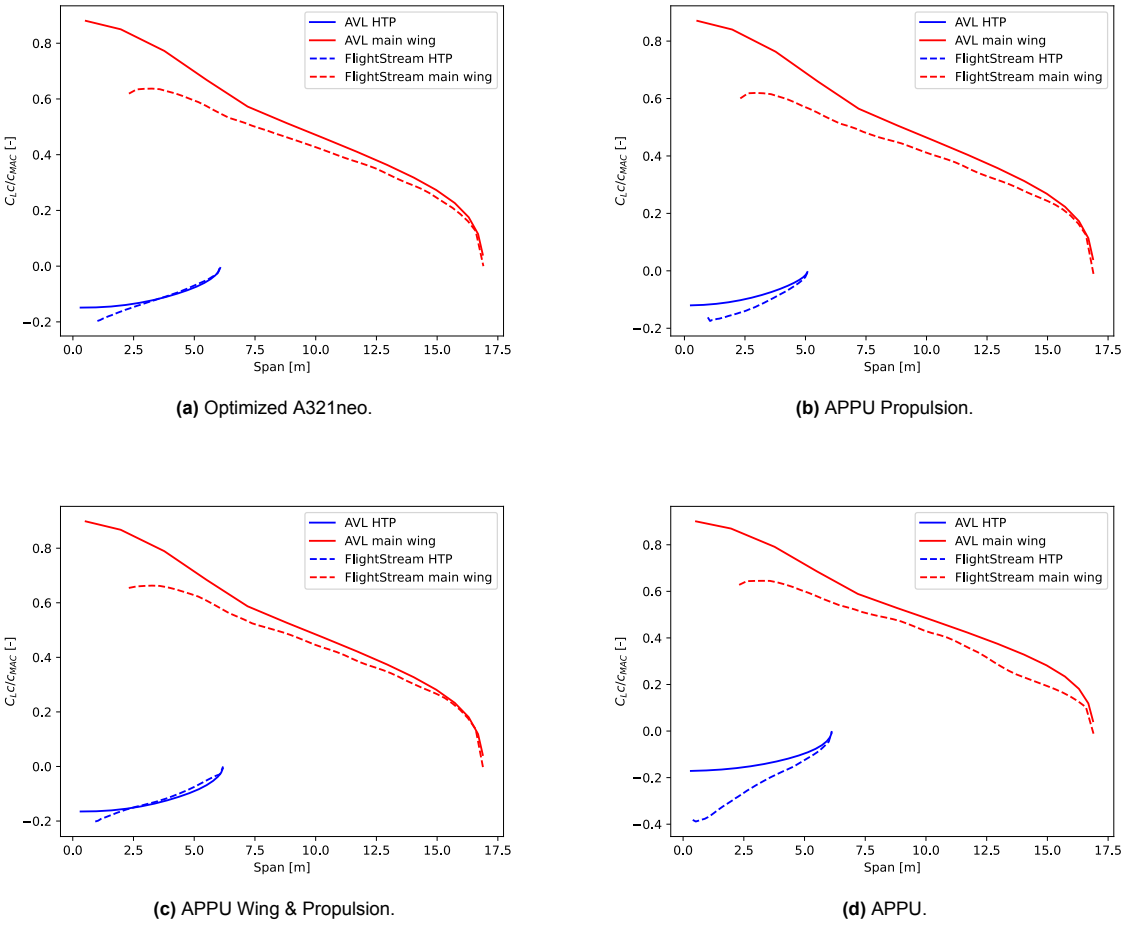

(a) Optimized A321neo.

(b) APPU Propulsion.

(c) APPU Wing & Propulsion.

(d) APPU.

Figure E.2: Spanwise lift distribution at cruise for the optimized configurations according to AVL and FlightStream.

E.3. Pressure Distribution

Figure E.3 and E.4 present the top and bottom views of the pressure distributions for the different configurations. The elevated downforce on the HTP of the APPU configuration is again visible. Additionally, the upper surface of the main wing in this configuration exhibits less negative pressure coefficients compared to the other configurations, resulting in a reduction in lift generated by the main wing.

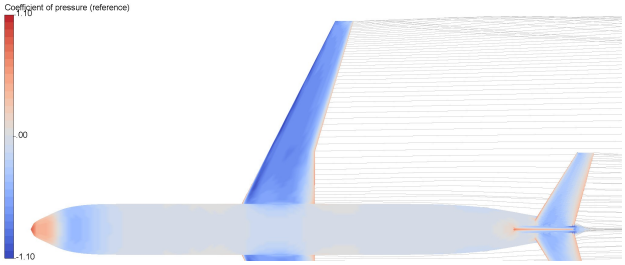

(a) Initial Design.

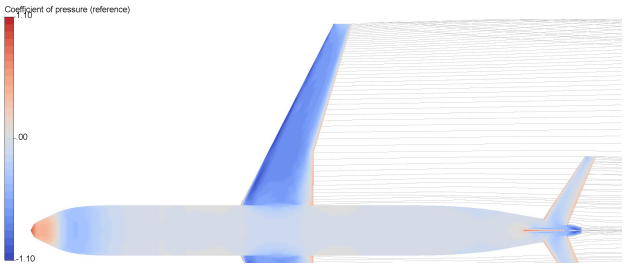

(b) Optimized A321neo.

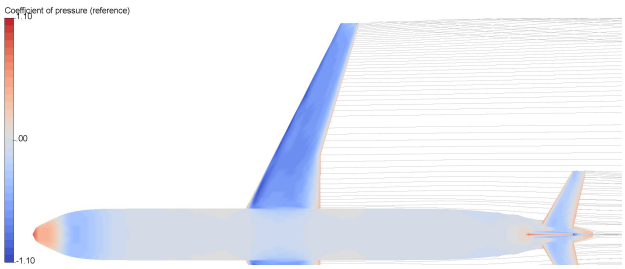

(c) APPU Propulsion.

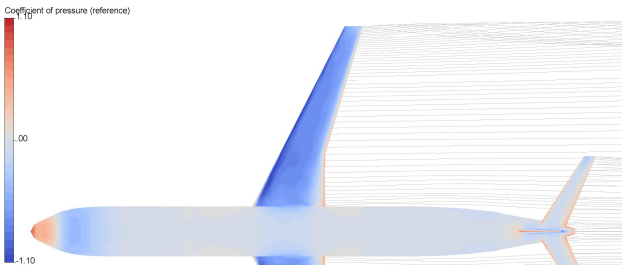

(d) APPU Wing & Propulsion.

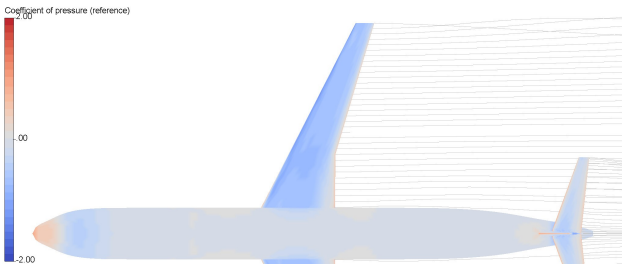

(e) APPU.

Figure E.3: Top view of the pressure distribution from FlightStream simulations at cruise for each configuration.

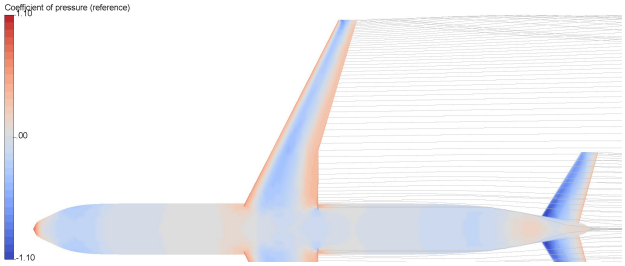

(a) Initial Design.

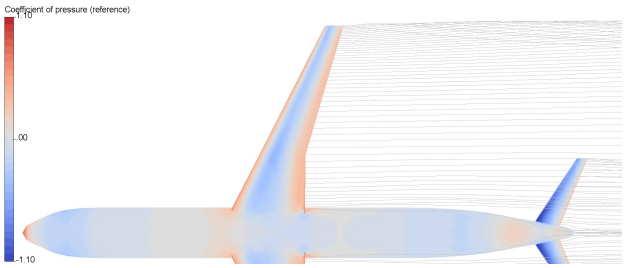

(b) Optimized A321neo.

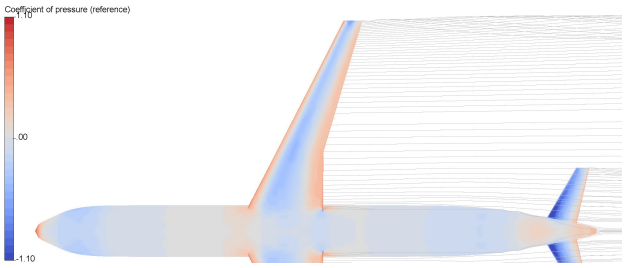

(c) APPU Propulsion.

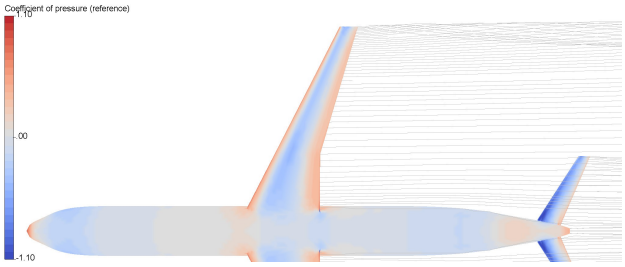

(d) APPU Wing & Propulsion.

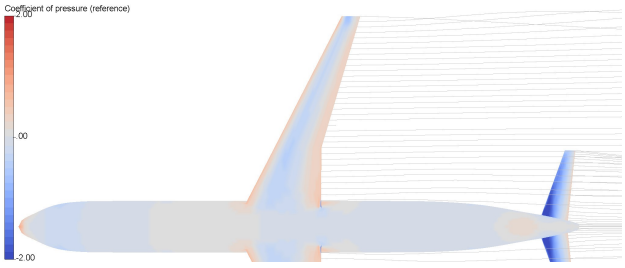

(e) APPU.

Figure E.4: Bottom view of the pressure distribution from FlightStream simulations at cruise for each configuration.